Spintronic sensor based microwave imaging

by

Lei Fu

A Thesis submitted to the Faculty of Graduate Studies of
The University of Manitoba
in partial fulfillment of the requirements of the degree of

Doctor of Philosophy

Department of Physics and Astronomy
University of Manitoba
Winnipeg

Thesis advisor

Can-Ming Hu

Author

Lei Fu

Spintronic sensor based microwave imaging

Abstract

Novel characteristics of spin-based phenomena are intensively researched in the hope of discovering effects that could be used to develop new types of high-performance spintronic devices. Recent dynamics studies have revealed new principles for spintronic devices to sense microwaves. The capabilities for detecting both microwave electric field and magnetic field could make the spintronic microwave sensor as ubiquitous as semiconductor devices in microwave applications in the future. In this thesis, the feasibility of spintronic sensors in microwave applications has been researched and developed. Thanks to the high conversion efficiency of microwave rectification in the magnetic tunnel junction (MTJ) based spintronic sensor, it can directly measure the coherent spatially scattered microwave field distribution and detect a hidden object by analyzing the reflected microwave amplitude pattern. To enable the real-time vector measurement of the microwave field, a sensor based rapid phase detection technique is also developed. Combining the rapid phase detection technique and the microwave holography principle, a two-dimensional microwave holographic imaging system using a spintronic sensor was built. The high sensitivity of the microwave phase measurement allows the coherent imaging of the target to be reconstructed in noisy environments. By adapting the broadband measurement, not only the shape but also

the distance of the target can be determined, which implies that three-dimensional imaging is achievable using a spintronic device. Combining the broadband microwave measurement and a wavefront reconstruction algorithm with a spintronic microwave sensor in circular trajectory, the reconstructed images of targets are obtained. The reconstructed images clearly indicate the targets' positions even when the targets were immersed in a liquid to simulate an inhomogeneous tissue environment. Our spintronic techniques provide a promising approach for microwave imaging, with the potential to be used in various areas, such as biomedical applications, security services, and material characterization.

Contents

List of Figures

List of Tables

Acknowledgments

Firstly, I would like to give my sincere thanks to my advisor Dr. Can-Ming Hu, who supported me during the past five years. I appreciate all his contributions of time, ideas, and funding to make my Ph.D. productive. I am also thankful for the great example he has been as a successful researcher and professor.

I would like to thank Dr. Stephen Pistorius, Dr. Daniel Rickey, and Dr. Gregory Bridges for serving as my internal committee members. I greatly appreciate your comments and suggestions which helped me a lot in improving my research.

I would like to thank my external committee member, Dr. Arthur Yelon from École Polytechnique de Montréal, for the time he spent reviewing my Ph.D thesis and his contribution in the improvement of my thesis. I also appreciate his presence at my Ph.D. defence, which requires a long trip from Montréal to Winnipeg at an age of over 80.

I would like to thank Dr. Yongsheng Gui, who gave me great support during my Ph.D. research. Without him, my Ph.D. research could not have been completed within five years.

I would like to thank Dr. Wei Lu and Dr. Bo Zhang from China Academy of Sciences, who introduced me to the opportunity of being a Ph.D. student at the University of Manitoba.

I would like to thank all the lab members, Dr. Lihui Bai, Dr. Bimu Yao, Zhaohui Zhang, Dr. Zhongxing Cao, Micheal Harder, Paul Hyde, Jinwei Rao, Sandeep Kaul, Alex Reimer, Yan Huo, Fuchun Xi and Yutong Zhao. I greatly appreciate your helpful discussions and assistances in my research.

I would like to thank my friends in Canada, Dr. Jiandongwu, Xun Wu, Dr.

Jilagamazhi Fu, Jing Li, Weitian Ji and Dr. Ping Zhou. Thanks for your support and friendship.

I would like to thank the University of Manitoba, the Natural Sciences and Engineering Research Council of Canada (NSERC), the Canadian Breast Cancer Foundation (CBCF), the CMC Microsystems, the National Key Basic Research Program of China and the Canada Foundation for Innovation (CFI) for their financial support.

Finally, I would like to thank my family for their unwavering support.

This thesis is dedicated to my parents.

For their endless love, support and encouragement

Chapter 1

Introduction

Microwave refers to electromagnetic waves with wavelengths in the range of 10 cm to 1 mm, which corresponds to a frequency range of 3 GHz to 300 GHz [1]. Compared with visible light and infrared, microwaves have a larger penetration depth in dielectric materials and less attenuation while penetrating in air. In contrast, when compared with radiowaves, microwaves have a smaller wavelength which makes microwave devices smaller and more portable. These advantages make microwave a powerful tool in many areas such as non-destructive testing [2; 3; 4; 5], geophysical investigation [6; 7; 8; 9], medical imaging [10; 11; 12; 13], communication [14; 15; 16], navigation etc. [1; 17]. In order to achieve these functionalities, the microwave signal should be precisely measured via a frequency down-convert technique using non-linear devices [17], for which three generations of microwave sensors have been developed [18], as shown in the schematic diagram in Fig. 1.1.

First generation microwave detector: In 1887 Heinrich R. Hertz invented the spark gap resonator which was used to detect radiowaves [19]. However, Hertz's

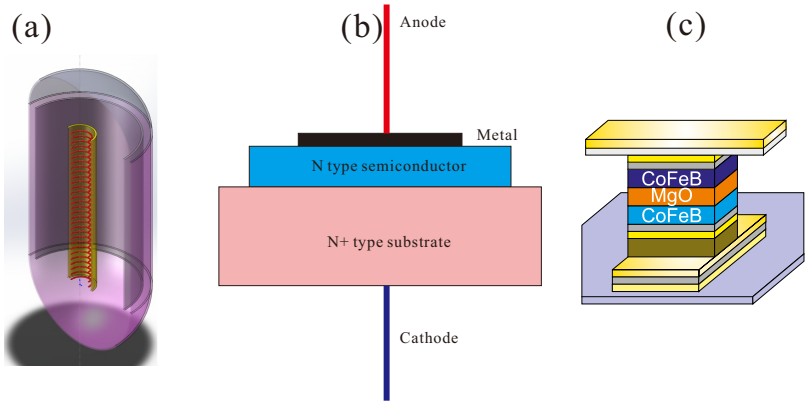

Figure 1.1: Three generations of microwave sensors. (left) Electron tube , (middle) Schottky diode and (right) magnetic tunnel junction

setup could only detect radiowaves that could ionize the air between electrodes which limits its application. Three years later, Edouard Branly built a "coherer" to record radiowave signals [20]. This device was based on the phenomenon that the conductivity of metal filings change due to any incident electromagnetic waves. However, the metal filings cannot return to their initial states after a radiowave signal is recorded and the resistance drop is independent of the strength of the radiowave, meaning this device is not suitable as a rectifier (RF detector) [18]. In 1903, John Ambrose Fleming used his "oscillation valve" to make the first widely used RF detector which employed electron thermionic emission [18]. The oscillation valve is a vacuum bulb with a heated filament and a cold metal cylinder. When the filament is heated up, due to thermionic emission, the electrons can only fly in one direction from the filament to the cylinder in the vacuum bulb. The amount of transmitted electrons is related to the detected radiowave strength. This oscillation valve was accepted and used as an RF detector. In 1907, a third electrode was added into the vacuum bulb by Lee De Forest to amplify the electrical signal [21]. This device was called the "electron tube"

and had a great impact since it was the first device that could amplify an electric signal. Electron tubes were widely used for more than 50 years after which they were replaced by solid-state devices. Compared with solid-state devices, electron tubes have several weaknesses in microwave detection. Two examples are that a battery is required to boost the electron tubes and that microwave frequencies are a little bit too high for the electron transition in electron tubes.

Second generation microwave detector: Today, the most widely used rectification devices are metal-semiconductor contact devices. Although the rectification effect of metal-semiconductor contact devices was first reported as early as in 1874 by F. Braun, the early metal-semiconductor contact devices were "point-contact devices" whose performance was uncontrollable. Thus, the market was still occupied by electron tubes [22]. This situation was only changed in 1939 because of the innovations in physics and material technology.

In 1939, silicon crystal ingots with a purity of 99.8% were obtained, making uniform doping possible in semiconductor materials. The uniform doping materials were so reliable that any part of silicon wafer could be fabricated almost identical devices [23]. Almost at the same time, W. Schottky first explained the mechanism of the contact barrier and developed a model for calculating the barrier height [23]. This was a fundamentally important work which made the performance of the metal-semiconductor contact devices predictable and reliable. From then on, the metal-semiconductor contact device was named the Schottky diode and was widely used in the Second World War. Now the Schottky diode is one of the most important devices in microwave detection and it may still be important in the coming decades.

However, after more than 70 years of development, the Schottky device has basically reached its maximum performance and little progress is expected in the next decade [18].

Third generation microwave detector: From a quantum point of view, charge dynamics have typical characteristic energies in the eV range which matches the optical frequencies [24]. This has been used to build optical sensors based on charge coupled devices which have revolutionized modern optical sensing and imaging technology. At microwave frequencies, the energy ranges are too low ($\sim \mu$eV) to be reached by charge dynamics. However, microwaves have the exact characteristic energy to excite spin dynamics in magnetic materials. Therefore spintronic (a subject studying the electron spin and its magnetic moment) devices may provide new possibilities and opportunities for developing microwave sensing technology.

As expected, spintronics has a long history which can be traced back to 1856 (before the concept of spin was proposed by S. Goudsmit and G. Uhlenbeck in 1925 [25]) when William Thomson discovered anisotropic magnetoresistance (AMR) [26], where the resistance of iron changes with the direction of the magnetization. For a long time, computer memory and hard discs were considered as one of the main applications of spintronics because the influence of the spin configuration on the electrical conduction in ferromagnetic metals based on AMR, giant magnetoresistance(GMR) and tunnel magnetoresistance (TMR) effects. The GMR effect especially, discovered by Albert Fert and Peter Grunberg [27] who won the Nobel Prize in Physics in 2007 [28], resulted in the rapid development of density of hard drives.

Recent dynamics studies of spintronic devices have revealed new principles for

devices such as nano-oscillators [29] and spin diodes [30] and thus opened up many possibilities to incorporate spintronic devices in microwave applications. The use of the spin diode effect in a magnetic tunnel junction (MTJ) device caused by spin transfer torque [30] aids the development of a new generation of microwave detector based on MTJ devices. In S. Yuasa's first report the microwave sensitivity, which is characterized by the ratio between the produced d.c. voltage and the incident microwave power, was only 1.4 mV/mW. This value is about three orders of magnitude lower than the commercial Schottky diode such as the SMS7630 from Skyworks [31]. Since then, many efforts have been made to improve the spintronic sensor's sensitivity, including optimized in-plane magnetic field [32], tilted magnetic field from the film normal [33], interfacial anisotropy using MgO [33] and d.c. current bias [34]. As a consequence, in 2014 the sensitivity increased to 12000 mV/mW [35] (about four orders of magnitude enhancement in performance), which is comparable with the Schottky diode. Theoretical studies have revealed that in the low microwave power limit, the spintronic sensor may show better signal to noise ratio than semiconductor devices [35; 36]. Based on the rapid development of spintronic microwave sensors in recent decades, the spintronic community optimistically believes that the overall performance of spintronic microwave sensors could eventually surpass that of semiconductor devices [35].

Advances in the performance of spintronic sensors have encouraged the exploration of its applications in non-destructive detection and microwave imaging. The small size of a spintronic sensor allows it to be placed close to the target for near field imaging without significantly distorting the wave pattern. For far field imaging, a

sensor receives less microwave power compared to an antenna; noise is potentially an issue, particularly for biomedical applications with exposure limits [37]. In addition, a precise determination of microwave phase is often required for practical applications as the microwave phase contains information crucial for a proper estimation of electric permittivity and conductivity profiles. These are the challenges faced for spintronic microwave sensors when I joined the Dynamic Spintronics Group at the University of Manitoba as a Ph.D. student in 2011.

The Dynamic Spintronics Group at the University of Manitoba is one of the leading groups in the world in the spintronic community, especially in the spintronic sensor study. In 2005, before moving to Canada, the group first reported the electrical detection of ferromagnetic resonance (FMR) using the photo-resistance effect in ferromagnetic microwave structure [38]. In 2007, the group invented the spin dynamo which is a micro-structured composite device combining a spintronic device and a coplanar waveguide (CPW) [39]. This device can effectively convert a microwave signal into d.c. voltage via the spin rectification effect. Different from semiconductor devices, spintronic devices are also sensitive to the microwave magnetic field (h-field) as well as its direction, which allowed the development of an h-field vector detector in 2008 by the Dynamic Spintronic group [40]. Later in 2010, by adapting the Michelson interferometer from optics, the on-chip spintronic sensor demonstrated the ability to resolve phase [41], which greatly broadened the potential of the spintronic sensor in microwave applications. The Spintronics group research has also explored the non-resonant range [42], where an external magnetic field of several mT instead of several hundred mT, required for the resonance condition, is applied. This technology allows

the determination of a material's dielectric constant using a spintronic sensor[43].

Based on the above existing knowledge and understanding in the Dynamic Spintronic group as well as the challenges faced by the community, my thesis research is aimed to demonstrate the feasibility of spintronic sensors in microwave sensing and imaging technologies and develop a spintronic microwave imaging system. During my Ph.D. research, I was involved in the following research and development:

Seebeck rectification [44]. This is a thermoelectric coupling effect in magnetic tunnel junctions (MTJ). A nonlinear correction to Ohm's law is induced by this effect. Dynamically, it rectifies microwaves in a broad frequency range which is more practically useful than the previous single frequency spin diode[30]. More importantly, the Seebeck rectification enables MTJs to work at zero external magnetic field and reduces the hardware requirement of a static magnetic field, which is essential for the spin rectification effect. The discovery of Seebeck rectification makes a portable spintronic based microwave system for practical applications possible.

Rapid microwave phase detection using spintronic sensors [45]. This technique enables a real-time microwave vector measurement by employing a phase-modulated reference and a lock-in amplifier, thus reducing the microwave phase measurement time using a spintronic sensor from minutes [41] to several ms [45]. As the microwave phase contains information crucial for an objects' permittivity and conductivity profile estimation, rapid microwave phase detection lays the foundations for spintronic sensor applications such as non-destructive detection and microwave imaging.

These techniques allow me to perform real-time microwave vector measurements

using a spintronic sensor based on an MTJ in the absence of any external applied magnetic field. During my Ph.D. study, to explore the microwave sensing and imaging technology using spintronic devices, I have achieved the following goals:

Detection of hidden objects [46]. A far-field microwave imaging technique has been developed using a spintronic sensor. Such a sensor can directly rectify a microwave field into a d.c. voltage signal using the Seebeck rectification effect. The high conversion efficiency of microwave rectification in MTJs, allows the sensor to directly measure the coherent spatial scattered microwave field distribution. The pattern is confirmed by simulations using COMSOL Multiphysics. By analysing the reflected microwave pattern, we can identify the presence of the hidden objects. In addition, the MTJ was used to measure the antenna's radiation pattern which could assist in designing antennas [47].

Development of spintronic microwave holographic imaging system [48]. Adapting the rapid phase detection technique, I developed a 2D microwave holographic imaging system using a spintronic sensor. This work demonstrated the feasibility of microwave holographic imaging applications using a spintronic microwave sensor. The high sensitivity of the microwave phase measurement allows the coherent imaging of the target to be reconstructed in noisy environments. This system can detect objects embedded in microwave penetrable media, even if the objects are smaller than the microwave wavelength. By employing a broadband frequency measurement, a 3D imaging system is achievable.

Development of spintronic microwave radar imaging system [49]. I demonstrated for the first time that spintronic microwave sensors have the capability

to perform microwave radar imaging. The detection of the amplitude and phase of a scattered microwave signal over a wide frequency band allows this technique to determine the time delay of a microwave signal scattered by the target. Combining microwave radar techniques and a wavefront reconstruction algorithm with a spintronic microwave sensor in a circular trajectory, the reconstructed images of targets are obtained. The reconstructed images clearly indicate the target's positions even when the targets were immersed in liquid to simulate an inhomogeneous tissue environment. Such a sensor based radar technique was employed in a clinical trial of the microwave imaging system.

This thesis is organized into 6 Chapters.

Chapter 1 mainly focuses on background, problems to be solved and outlines the main achievement and the structure of this thesis.

Chapter 2 contains a detailed discussion about semiconductor sensors, spintronic sensors, electrical rectification mechanisms and thermal rectification mechanisms.

Chapter 3 mainly focuses on obtaining microwave amplitude mapping and its applications, such as non-destructive detection and assisting antenna design.

Chapter 4 discusses the rapid microwave phase detection technique and the sensor based microwave holography system.

Chapter 5 discusses the spintronic sensor based microwave radar system and the sensor based clinical trial microwave imaging system.

Chapter 6 is the summary and future work.

Chapter 2

Microwave Sensor principles

2.1 Introduction

The microwave frequency ranges from several GHz to several hundred GHz [1]. In order to directly track microwave signals, electronic devices with response times on the sub nanosecond scale are required. This is beyond the capability of most electronic devices. To process microwave signals, a frequency translation is required to convert the high frequency signal to a low frequency signal. A similar case is the optical rectification effect, which converts the light signal into a d.c. voltage via nonlinear media with a large second order susceptibility [50; 51]. In general, a frequency conversion happens when two waves mix together in a nonlinear device or media. The waves are governed by the trigonometric relation of [51]

$$\cos(\omega_{RF}t)\cos(\omega_{LO}t) = [\cos((\omega_{RF} - \omega_{LO})t) + \cos((\omega_{RF} + \omega_{LO})t)]/2, \tag{2.1}$$

where ω_{RF} and ω_{LO} are the circular frequencies of the two waves. If the two waves have the same frequency $\omega_{RF} = \omega_{LO}$, the first term and the second term in the right

hand side of Eq. 2.1 gives the rectification and the second harmonic term, respectively. This wave mixing principle can be applied to a microwave sensor.

2.2 Microwave sensors

In a microwave sensor, a d.c. voltage is generated by the coupling of an oscillating current j_{rf} with an oscillating resistance. In a nonlinear device, the voltage across a device can be generally expressed according to a Taylor expansion as

$$V = IR = [I_0 + j_{rf}\cos(\omega t)][R_0 + \frac{\partial R}{\partial I} j_{rf}\cos(\omega t) + \frac{\partial R}{\partial H} h_{rf}\cos(\omega t) + ...], \tag{2.2}$$

where I is the current which includes a d.c. part I_0 and an a.c. part $j_{rf}\cos(\omega t)$, R is the device's resistance, including a static part R_0 and an oscillating part $\delta R\cos(\omega t) = \frac{\partial R}{\partial I} j_{rf}\cos(\omega t) + \frac{\partial R}{\partial H} h_{rf}\cos(\omega t)$ for the first order correction of the resistance caused by current and magnetic field. By reorganizing Eq. 2.2, we have

$$V = I_0 R_0 + j_{rf}\cos(\omega t)\cdot\delta R\cos(\omega t) + I_0\cdot\delta R\cos(\omega t) + j_{rf}\cos(\omega t)\cdot R_0, \tag{2.3}$$

where $I_0 R_0$ is the result of d.c. bias which does not contribute to the rectification and may be ignored in the following steps. $I_0\cdot\delta R\cos(\omega t)$ and $j_{rf}\cos(\omega t)\cdot R_0$ do not contribute to the rectification either since their time averaged values are zero. Taking the time averaged value of voltage, we get

$$\langle V\rangle = \langle\delta R\cos(\omega t)\cdot j_{rf}\cos(\omega t)\rangle = \delta R\cdot j_{rf}/2 \tag{2.4}$$

where$\langle\rangle$ represents the time averaged value. It is clearly observed that the rectification comes from the coupling of the oscillating current and the oscillating resistance. The schematic diagram of the rectification mechanism is shown in Fig. 2.1. The a.c.

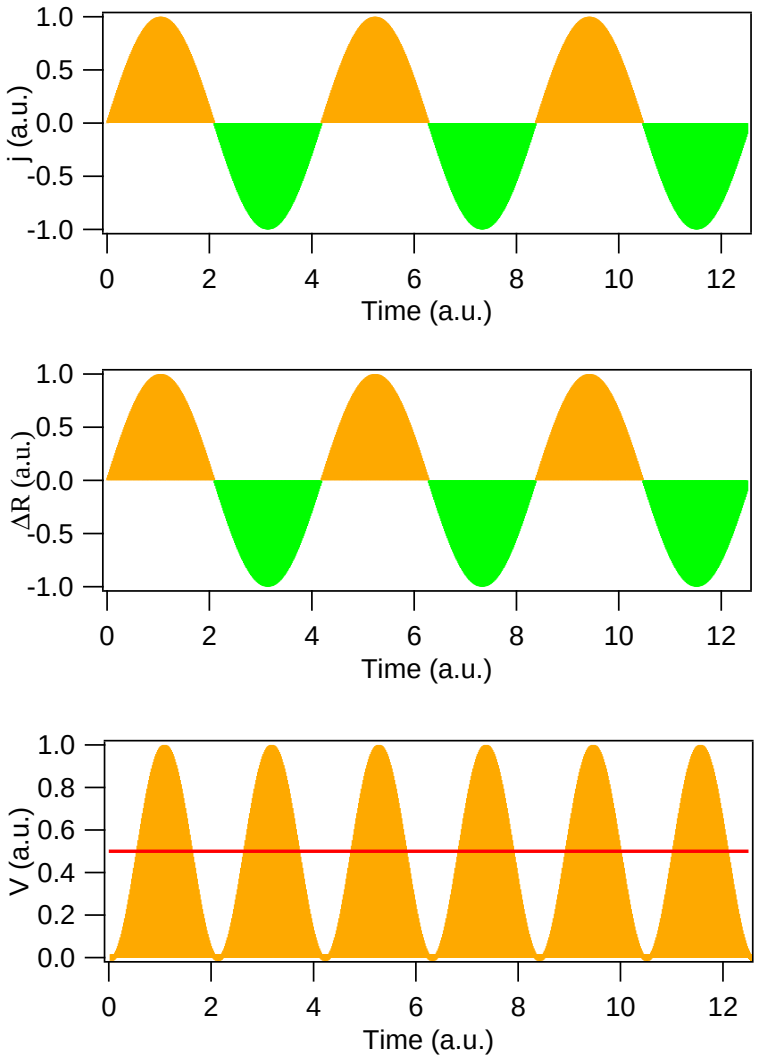

Figure 2.1: (a) The induced microwave current as a function of time in the microwave sensor. (b) The oscillating resistance of a microwave sensor as a function of time. (c) Rectification voltage as a function of time. The d.c. voltage component is indicated by the red line.

microwave current is shown in Fig. 2.1(a), where the yellow and green parts indicate a positive and negative current respectively. The oscillation of the device's resistance is shown in Fig. 2.1(b), which is induced by either the microwave e-field (microwave current) or by the microwave h-field. The coupled voltage is shown in Fig. 2.1(c),

where a d.c. voltage component is indicated by a red line and an a.c. voltage with a frequency of 2ω is indicated by the amplitude oscillation.

2.2.1 Schottky diode

In general, the resistance oscillation δR comes from the perturbation by both the microwave e-field and h-field. In a semiconductor sensor, the perturbation from the microwave h-field is negligible, thus only the $\frac{\partial R}{\partial I}$ term contributes to the rectification effect. The most widely used semiconductor microwave sensor is the Schottky diode named after Walter H. Schottky. The Schottky diode is a metal-semiconductor contact diode whose schematic diagram is shown in Fig. 2.2(a). The Schottky diode is a majority carrier device which has a lower turn on voltage, faster switching speed and smaller capacitance than other types of diodes [52]. Due to its high frequency performance, a Schottky diode is usually used as radio frequency and microwave mixer and detector.

Consider a metal that has a work function of W_m and an n type semiconductor that has an electron affinity of χ and a work function of W_s. The work function is defined as the energy difference between the vacuum level E_0 and the Fermi level E_F, whereas the electron affinity is defined as the energy difference between the vacuum level E_0 to the bottom of conduction band E_c. For a given material, the work function of the metal and the electron affinity of the semiconductor are fixed, while the work function of the semiconductor can be tuned by doping. The energy band diagram of a metal and semiconductor separately can be seen in Fig. 2.2(b). When the metal and the semiconductor are in contact with each other, electrons flows from the high energy

region to the low energy region until the Fermi level of the two materials becomes the same. Consider the case $W_s < W_m$, in the redistribution process, the electrons transfer from the semiconductor to the metal, forming a space charge layer. This space charge layer bends the band structure near the interface, forming an interface barrier, as shown in Fig. 2.2(c). The height of the interface barrier in the metal and in the semiconductor are $W_m - \chi$ and $eV_D = W_m - W_s$, respectively.

On a positive voltage bias (from metal to semiconductor), the barrier height in the metal remains the same, while the barrier height in the semiconductor decreases, which increases the number of electrons transferred to the metal. This results in a positive current across the junction. On a negative bias (from semiconductor to metal), the increase of barrier height in the semiconductor blocks the electrons' transport. This is the reason why the Schottky diode shows unipolar conductivity.

The I-V characteristic of an ideal Schottky diode can be expressed as [52]

$$I = I_s(\exp(eV/k_BT) - 1), \tag{2.5}$$

where I_s is the reverse biased saturation current determined by the diode's area and the barrier height [52], V is the voltage applied on the diode, k_B is the Boltzmann constant and T is the temperature. Rewriting Eq. 2.5 to express V as a function of I, we can get that

$$V = \frac{k_BT}{e}\ln(\frac{I}{I_s} + 1). \tag{2.6}$$

For a small current, Eq. 2.6 can be expanded in terms of series of $\frac{I}{I_s}$ as

$$V = \frac{k_BT}{e}[\frac{I}{I_s} - \frac{1}{2}(\frac{I}{I_s})^2 + ...]. \tag{2.7}$$

The voltage responsivity of a microwave detector is defined as the ratio of the d.c.

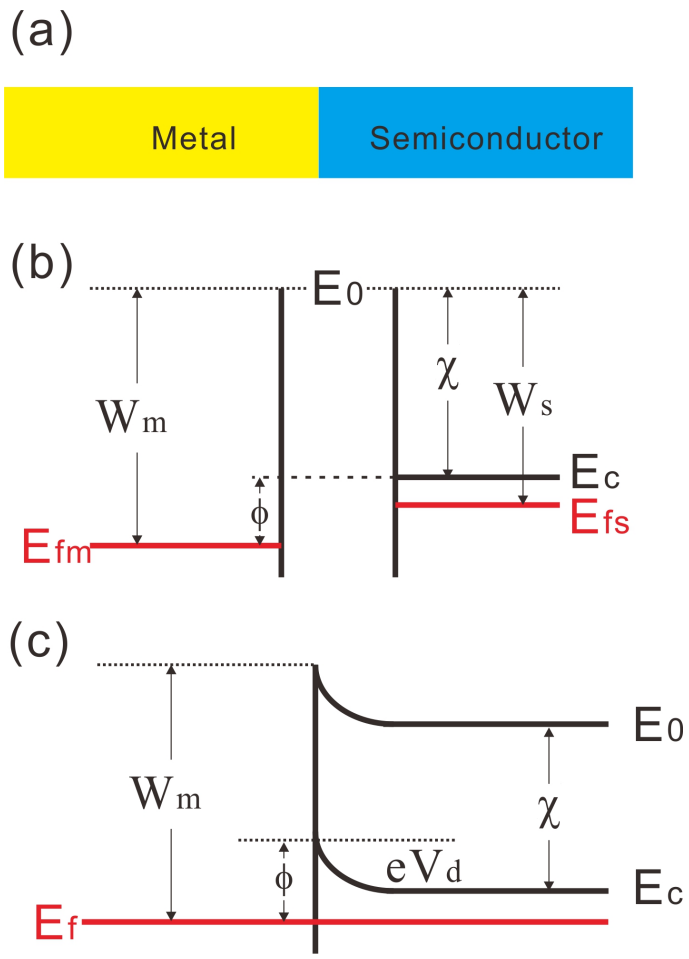

Figure 2.2: (a) Schematic diagram of a Schottky diode. The left and right hand sides are metal and semiconductor parts, respectively. (b) Energy band diagram of a separate metal and semiconductor. (c) Energy band diagram when metal and semiconductor are in contact with each other, where thermal equilibrium has been made.

voltage produced over the input microwave power. Therefore, the voltage responsivity can be determined from the I-V relationship as [53; 54]

$$R_v \equiv -\frac{dV^2/dI^2}{dV/dI}. \tag{2.8}$$

In the ideal Schottky diode case, R_v is deduced as

$$R_v = -\frac{1}{I_s - I} \tag{2.9}$$

For $I = 0$, $R_v = -\frac{1}{I_s}$.

2.2.2 Spintronic sensor

While semiconductor devices have been widely used for microwave detection for more than half a century, a new generation microwave sensor based on spintronic devices emerged in 2005 [30]. Spintronics, or spin electronics, involves the study of active control and manipulation of spin degrees of freedom in solid-state systems [55]. Spintronics studies are focused on the spin dynamics, spin transport, and spin relaxation properties during electrical, magnetic and thermal processes in semiconductor and metals [55]. Traditionally, microwaves are widely used to study the excitation of electron spins in spintronic devices since the energy of the electron spin is in the microwave range. During these studies, people have found that a d.c. voltage can be generated from a microwave field via various mechanisms, such as the spin rectification effect in a single FM layer [39], the spin rectification effect in multilayer MTJ devices [30] and spin Seebeck rectification effect in multilayer MTJ devices[44]. It was soon realized that the high conversion efficiency from microwave to d.c. voltage could make spintronic devices the next generation of microwave sensors. Exploring the feasibility of microwave applications for spintronic devices quickly became a hot research topic in spintronic communities due to using a different principle from semiconductor devices as well as a unique capability in microwave magnetic field detection [40].

In conventional semiconductor sensors, $\frac{\partial R}{\partial I}$ in Eq. 2.2 is the only contributing term, and hence semiconductor sensors are only sensitive to microwave e-fields. In

spintronic sensors, $\frac{\partial R}{\partial H}$ in Eq. 2.2 is no longer negligible, making spintronic sensors not only sensitive to microwave e-fields, but also to microwave h-fields. In the following sections of this chapter, I will provide a detailed discussion of the physical principles of spintronic microwave sensors which are based on the magnetoresistance effect.

2.3 Magnetoresistance effect and rectification mechanism

Magnetoresistance (MR) refers to the phenomenon of change in a material's resistivity with the application of an external magnetic field [27]. It is very dependent upon the magnetic field strength and the relative direction of the magnetic field with respect to current. Though the MR effect can occur in some non-magnetic metal and semiconductors, it mainly appears in magnetic materials [27]. Based on the material structure, the MR effect is commonly observed as anisotropic magnetoresistance (AMR) in a single ferromagnetic metal (FM), as giant magnetoresistance (GMR) in FM/NM (normal metal)/FM, and as tunnelling magnetoresistance (TMR) in FM/IN (insulator)/FM. A typical parameter used to describe the MR effect is the MR ratio, which is defined as

$$MR_{ratio} = \frac{R_{max} - R_{min}}{R_{min}} \times 100\%, \tag{2.10}$$

where R_{max} and R_{min} are the maximum and minimum values of the device's resistance as the magnetization changes. The typical values of AMR, GMR and TMR are about $1 \sim 2\%$[42], $10 \sim 20\%$ [28] and $100 \sim 200\%$ [28], respectively. When applied, the microwave field results in a perturbation of the external magnetic field, which results

in an oscillation of the material's resistance due to the MR effect. Following the mechanism described in section 2.2, the production of the resistance oscillation and the microwave current will produce a d.c. voltage. For a given microwave field, larger resistance oscillation gives a larger d.c. voltage, which makes MTJ the best candidate for a spintronic microwave sensor. In this section, I provide a detailed discussion about the AMR and TMR effects that were commonly used for spintronic microwave sensors.

2.3.1 Spin rectification effect in a single FM layer

The AMR effect is the earliest discovered MR effect, whose history can be traced back to 1856 [26]. In ferromagnetic metals, the resistance is dependent on the relative angle between the current and the magnetization direction. The key characteristic angular dependence of AMR is

$$R = R_{\perp} + (R_{\parallel} - R_{\perp}) \cos^2 \theta_M, \tag{2.11}$$

where θ_M is the relative angle between the current and the magnetization direction, $R_{\perp}$ and $R_{\parallel}$ are the material's resistances when $\theta_M = 90°$ and $0°$, respectively, and $\Delta R = R_{\parallel} - R_{\perp}$ is the resistance change. A typical result of such angular dependence is shown in Fig. 2.3. The origin of the AMR is from the spin orbit coupling. As the magnetization rotates, the electron cloud about each nucleus deforms, which changes the electron scattering cross section when it travels across the lattice. A heuristic explanation can be used to understand the origin of the AMR effect [27]. In ferromagnetic metals, the magnetization direction can rotate the bound electron

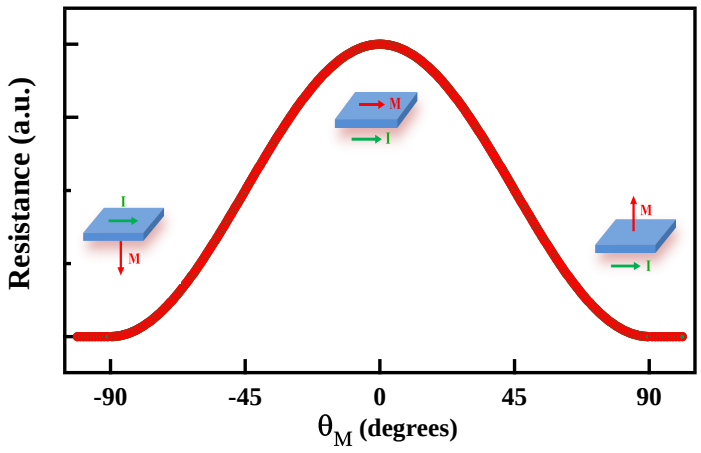

Figure 2.3: Typical Result of the ferromagnetic material's resistance with respect to θ_M. The insets are the schematic diagrams showing the angle of current and magnetization direction.

orbit orientation about the nucleus. The bound electron orbit direction is in the plane of current when the magnetization direction is transverse to the current, as shown in the schematic diagram in Fig. 2.4(a). In this case, a small scattering cross section is expected, which gives a low resistance state. When the magnetization direction is parallel to the current, the electron orbit is perpendicular to the current. This induces a larger scattering cross section which gives a high resistance state, as shown in Fig. 2.4(b).

The AMR effect is usually studied using $Ni_{0.8}Fe_{0.2}$ (permalloy, Py) which is a ferromagnetic material with a relatively large AMR effect ($\sim 2\%$) at room temperature and low saturation fields (5-10 kOe) [27]. In 2007, our group fabricated a device in which Py is integrated into a coplanar waveguide (CPW)[39]. As shown in the schematic diagram in Fig. 2.5(a), the Py stripes are located in the gap between the signal (S) line and the ground (G) line, where the microwave energy is concentrated

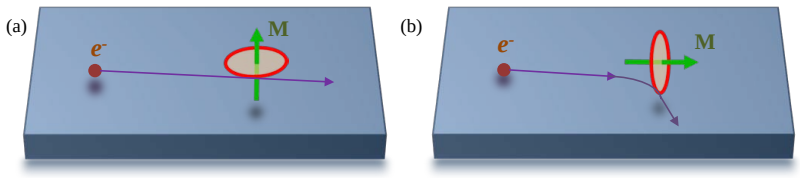

Figure 2.4: Schematic diagram of the origin of AMR effect. The shaded area inside the red ring indicates the bound electron orbit. (a)In case of magnetization direction perpendicular to the current direction, the bound electron orbit is in plane with the current. And a smaller scattering cross section is expected. (b) In the case of magnetization direction parallel to the current direction, the bound electron orbit is out of plane with the current. And a larger scattering cross section is expected.

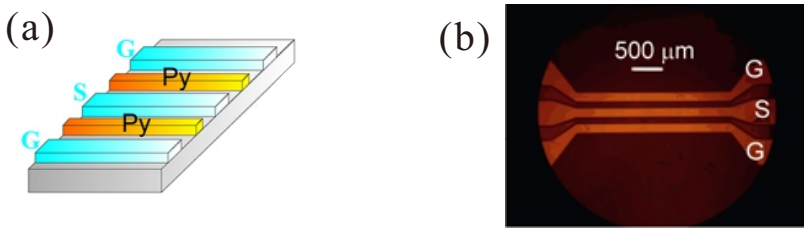

Figure 2.5: (a) Schematic diagram and (b) optical picture of the permolloy (Py) integrated into a CPW. G and S indicate the ground and signal lines of the CPW. Py stripes are located at the gap between the ground and the lines. After Gui et al. [39], used with permission.

by the CPW. The optical picture of the sample under a microscope is shown in Fig. 2.5(b).

Microwaves drive the precession motion of the Py's magnetization around the external magnetic field, as indicated by the orange cone in Fig. 2.6. This makes the angle in Eq. 2.11 $\theta_M = \theta_H + \theta\cos(\omega t)$, where θ is the precession angle, and θ_H is the Py's equivalent magnetization direction parallel with the external magnetic field. The precession of magnetization induces a resistance oscillation due to the AMR effect. Usually, $\theta \ll \theta_H$, which makes the oscillating resistance approximation to be $\Delta R\theta\sin(2\theta_H)\cos(\omega t)$. Coupled with an a.c. microwave current $j = e\sigma\cos(\omega t)$, a d.c.

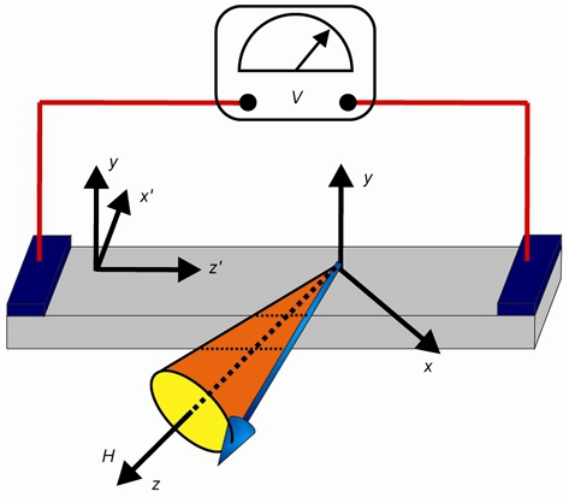

Figure 2.6: The schematic diagram of the experiment setup measuring the rectification voltage of Py while applying an in-plane static magnetic field H. The current is along the strip's length and is parallel with the z' direction. The z-axis rotates to follow the direction of H, and M precesses around H elliptically. After Gui et al. [56], used with permission.

voltage of $V \propto \Delta R\sigma e\theta \sin(2\theta_H)/2$ is produced, where σ is the material's electrical conductivity. For the experimental configuration shown in Fig. 2.6, the microwave current is in the z' direction and the external magnetic field is in the z direction. In the small precession angle approximation, θ can be expressed as $\theta = m_x/M_0$, where m_x is the dynamic magnetization in the x direction and M_0 is the static magnetization which is in the z direction. Thus, the rectification voltage across the Py sample can be expressed as

$$V_{z'} = -\frac{\Delta R}{M_0}\langle Re(m_x \exp^{-i\omega t}) Re(j_{z'} \exp^{-i\omega t})\rangle \sin(2\theta_H). \tag{2.12}$$

$\overrightarrow{\mathbf{m}}$ and $\overrightarrow{\mathbf{h}}$ are connected by magnetic susceptibility $\hat{\chi}$, expressed as $\overrightarrow{\mathbf{m}} = \hat{\chi}\overrightarrow{\mathbf{h}}$, where $\hat{\chi}$ is a tensor. The relation can be written as

$$\begin{pmatrix} m_x \\ m_y \\ m_z \end{pmatrix} = \begin{pmatrix} \chi_{xx} & i\chi_{xy} & 0 \\ -i\chi_{xy} & \chi_{yy} & 0 \\ 0 & 0 & 0 \end{pmatrix} \begin{pmatrix} h_{x'}\mathrm{e}^{i\Phi_{x'}}\cos\theta_H - h_{z'}\mathrm{e}^{i\Phi_{z'}}\sin\theta_H \\ h_y\mathrm{e}^{i\Phi_y} \\ h_{x'}\mathrm{e}^{i\Phi_{x'}}\sin\theta_H + h_{z'}\mathrm{e}^{i\Phi_{z'}}\cos\theta_H, \end{pmatrix}$$

where Φ_k is the relative phase of the microwave h-field with the microwave current in the z' direction, and χ_{xx}, χ_{xy} and χ_{yy} are the matrix elements of $\widehat{\chi}$. χ_{xx}, χ_{xy} and χ_{yy} can be expressed as a combination of Lorentzian L and a dispersive D line shape curve, written as $(\chi_{xx}, \chi_{xy}, \chi_{yy}) = (D+iL)(A_{xx}, A_{xy}, A_{yy})$, where A_{xx}, A_{xy} and A_{yy} are the coefficients determined by the permalloy sample [56]. L and D can be expressed as

$$L = \frac{\Delta H^2}{(H-H_r)^2 + \Delta H^2} \tag{2.13}$$

$$D = \frac{\Delta H(H-H_r)}{(H-H_r)^2 + \Delta H^2}, \tag{2.14}$$

where H, H_r and ΔH are the applied magnetic field, resonance field and line width, respectively [56]. Based on these facts, the rectification voltage can be simplified as a combination of Lorentzian L and a dispersive D line shape curve as

$$V_{z'} = -\frac{\Delta R}{M_0} j_{z'}(A_L L + A_D D), \tag{2.15}$$

whose amplitude A_L and A_D can be expressed as

$$A_L = sin(2\theta_H)[-A_{xx}h_{x'}\sin\Phi_{x'}\cos(\theta_H) + A_{xx}h_z\sin\Phi_{z'}\sin(\theta_H) - A_{xy}h_y\cos\Phi_y]/2, \tag{2.16}$$

$$A_D = sin(2\theta_H)[A_{xx}h_x\sin\Phi_{x'}\cos(\theta_H) - A_{xx}h_z\cos\Phi_{z'}\sin(\theta_H) - A_{xy}h_y\sin\Phi_y]/2. \tag{2.17}$$

From Eq. 2.12, it is clear that the rectification voltage is proportional to the product of m_x and j'_z and hence the microwave power, which is confirmed experimen-

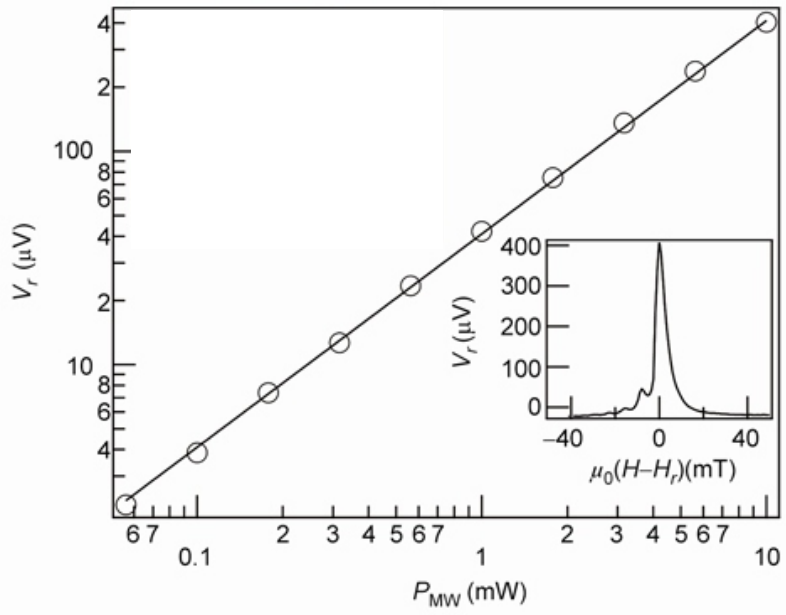

Figure 2.7: The measured voltage as a function of microwave power for FMR. This shows that V_r is linearly dependent on microwave power and the line is a linear fitting. The inset is a typical voltage spectrum at 6.0 GHz with an input microwave power of 10 mW. After Gui et al. [56], used with permission.

tally. As shown in Fig. 2.6, microwaves at 6.0 GHz with an output power of 10 mW were injected into the Py strip. The d.c. voltage across the Py strip was measured. The typical voltage spectrum when sweeping the external magnetic field is shown in the inset of Fig. 2.7, where the resonant nature is clearly observed. Swept at the resonant field, the voltage was linearly proportional to the injected microwave power, as shown in Fig. 2.7. To distinguish it from semiconductor devices, this rectification mechanism was named the "spin rectification effect" [39].

Microwave h-field detection

For a long time, loop antennas were important tools for microwave h-field detection [57]. These were based on Faraday's law of induction where the signal was

proportional to the loop area [58]. In recent years, the demand for microwave h-field detection has increased rapidly because of the development of metamaterials in the microwave range [59]. However, it is difficult to accurately measure the microwave h-field as well as its direction in the subwavelength scale by using loop antennas. As discussed before, the spintronic sensor is sensitive to both the microwave e-fields and h-fields. This makes a spintronic sensor a good candidate for a microwave h-field detector in the subwavelength scale. Our group first found that in addition to the amplitude, the spintronic sensor is also sensitive to the phase and the microwave h-field polarization direction at the subwavelength scale [40].

The spintronic sensor our group used is a permalloy strip with dimensions of 3 mm $\times$ 50 μm $\times$ 45 mm. The sensor is connected to the electrode on the sample holder via gold bonding wires. The dimensions of the sensor are much smaller than the microwave wavelength (2.5 cm), which is referred to as subwavelength detection. To demonstrate the feasibility of microwave h-field detection, an X band standard microwave rectangular waveguide was employed, whose microwave field distribution was well known. As shown in Fig. 2.8, the waveguide was working in TE_{10} mode. When working in the TE_{10} mode, microwaves propagated along the y direction with their e-field polarized in the z direction and the h-field polarized in the x-y plane. The spintronic sensor was fixed in the center of the open end of the waveguide, where h_x is much larger than h_y and h_z.

In this experiment, the external magnetic field is rotated in the x-z plane while the rectangular waveguide (microwave field) and the spintronic sensor keep their positions. The angle between the external magnetic field and the spintronic sensor

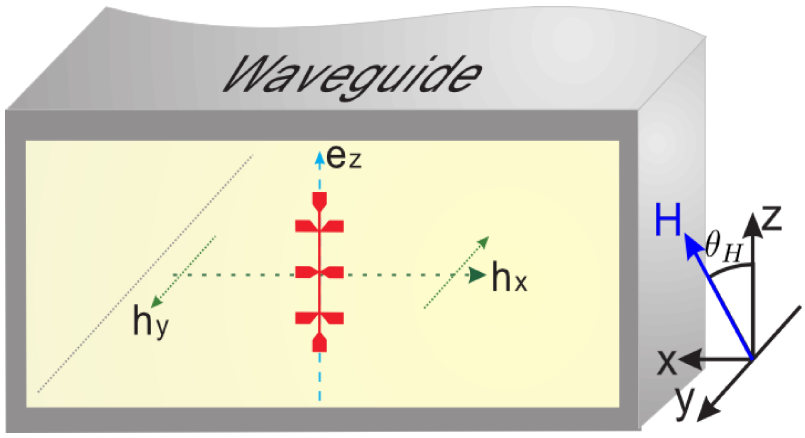

Figure 2.8: Microwave h-field detection in a rectangular waveguide via a spintronic sensor. The sensor is mounted at the end of a rectangular waveguide, where the electromagnetic field is well defined. At the sensor's position, h_x is much larger than h_y and h_z. After Bai et al. [40], used with permission.

is defined as θ_H. At each angle θ_H, the rectification voltage across the spintronic sensor was recorded as a function of external magnetic field, as shown in Fig. 2.9(a). As discussed previously, the rectification voltage can be regarded as a combination of a Lorentz and a dispersive line shape curve, whose amplitudes A_L and A_D are functions of h_x, h_y and h_z. A_L and A_D can be fit to Eq. 2.16 and 2.17, as shown in Fig. 2.9(b). From the fitted, we get results of h_y/h_x=0.04 and h_z/h_z=0.22, meaning that the microwave h-field dominates in the x direction. This result is in agreement with the microwave h-field distribution calculated from the Maxwell equations and is the first experiment to detect a microwave h-field using a spintronic sensor [56].

2.3.2 Spin rectification effect in multilayer MTJ devices

MTJ is one of the most important structures in spintronic studies. MTJs have been widely used as memories (magnetoresistive random-access memory, MRAM) due

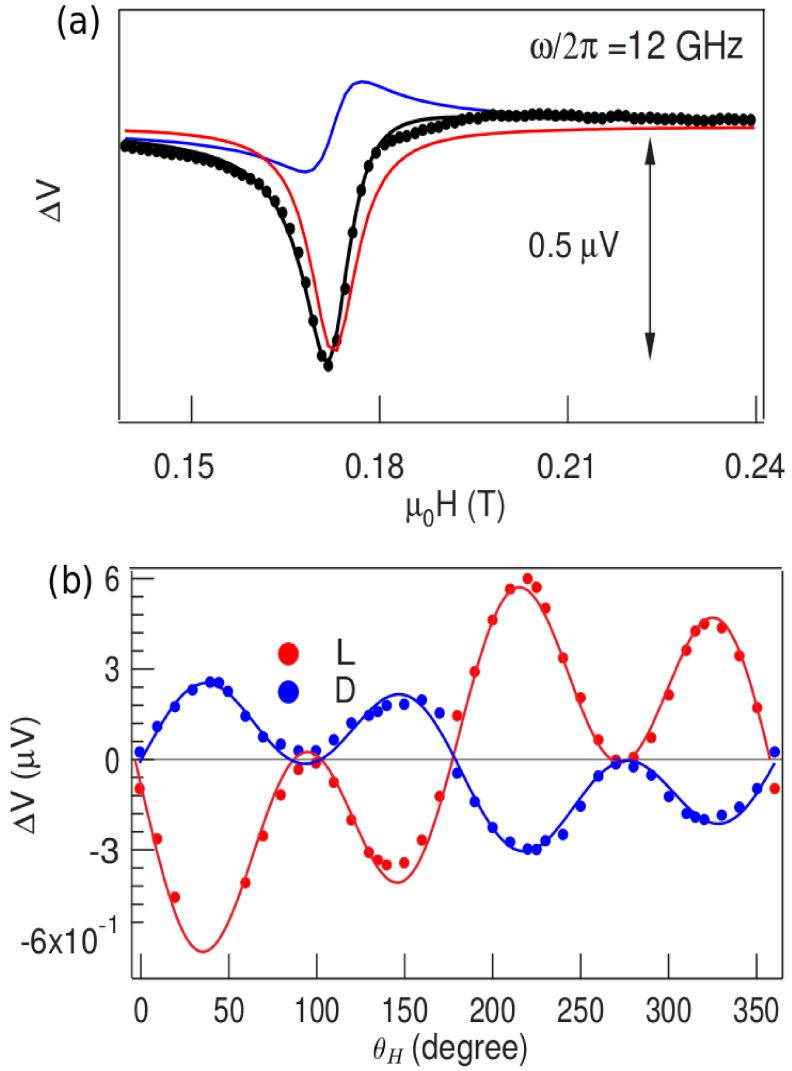

Figure 2.9: (a)Rectification voltage as a function of external magnetic field when $\omega/2\pi$=12 GHz and θ_H=45°. (b) Amplitude of Lorentz line shape L and dispersive line shape D as functions of angle θ_H. After Bai et al. [40], used with permission.

to their static properties [54]. Recent dynamic studies have revealed new principles that opened up new microwave application areas. MTJ is a device with a sandwich structure. A series of ultra thin films made of different materials are stacked on a substrate to form an MTJ device, as shown in Fig. 2.10(a). The core parts of MTJ include two FM layer separated by a tunnel layer. One of the FM layers is called the

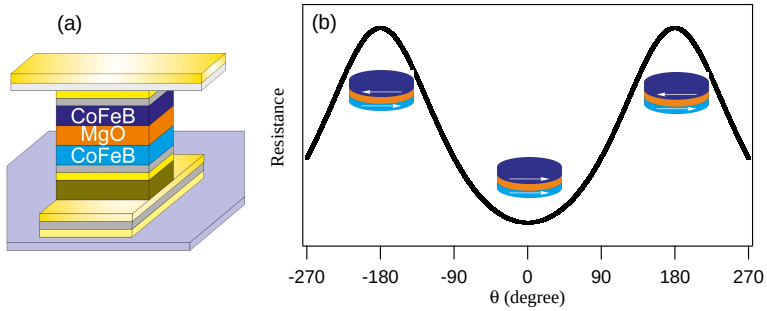

Figure 2.10: (a)Schematic diagram of a MTJ structure. (b)Typical angular dependence of the MTJ's resistance with respect to θ. The insets are the schematic diagrams showing the P state and AP state.

pinning layer whose magnetization direction is fixed by an anti-ferromagnetic layer. The other FM layer is called the free layer whose magnetization direction can be easily changed by an external magnetic field. By tuning the external magnetic field, one can change the magnetization configuration of the MTJ device. There are two types of preferred magnetization configurations when zero magnetic field is applied: the anti-parallel (AP) state and parallel state (P). The schematic diagram of the AP state and P state are shown as the insets in Fig. 2.10(b) when their relative angle θ=0° and 180°, respectively.

The thickness of the insulating layer is usually on the order of nanometres so that the electrons can tunnel through it. As a result of spin polarized tunnelling, the tunnel resistance of an MTJ is dependent upon the magnetization configuration. This is called the TMR effect. The TMR effect was first observed by M. Jullière in 1975 in a Fe/GeO/Fe junction [60], whose TMR ratio is 14% at 4.2 K. In 1991, the TMR effect was observed at room temperature by Terunobu Miyazaki [61]. At that time, the TMR ratio was only 2.5 %, which is similar to the ratio for the AMR effect.

In the following decades, the TMR ratio increased tremendously, reaching a value of 604 % in 2008 at room temperature [62].

The phenomenon of TMR can be described by the two current model proposed by M. Jullière [60]. In the two current model, the electron spin is considered to be conserved during the tunnelling process and electrons with different spins tunnel through their own channels. This means that the spin-dependent tunnelling rate is only related to the spin-dependent density of state (DOS) in each ferromagnetic layer. Also, the total conductances is the sum of conductance for both spin up and spin down electrons.

At the anti-parallel and parallel states, the conductance G_{ap} and G_p of an MTJ is

$$G_{ap} \propto N_T^{\uparrow} N_B^{\downarrow} + N_T^{\downarrow} N_B^{\uparrow} \tag{2.18}$$

$$G_p \propto N_T^{\uparrow} N_B^{\uparrow} + N_T^{\downarrow} N_B^{\downarrow} \tag{2.19}$$

where N_T and N_B represent the DOS at the Fermi level for the top ferromagnetic layer and the bottom ferromagnetic layer, respectively. The $\uparrow$ and $\downarrow$ indicate the majority and minority electrons in the ferromagnetic layers. In the normal case, $N_T^{\uparrow} > N_T^{\downarrow}$ and $N_B^{\uparrow} > N_B^{\downarrow}$ so that $G_p > G_{ap}$, which means that the AP state has larger resistance compared with the P state. Following the MR ratio definition described in the previous section, the TMR ratio can also be expressed as

$$TMR_{ratio} = \frac{R_{\max} - R_{\min}}{R_{\min}} = \frac{R_{ap} - R_p}{R_p} = \frac{G_p - G_{ap}}{G_{ap}} = \frac{2P_T P_B}{1 - P_T P_B} \tag{2.20}$$

Where the R_{ap} and R_p stand for the resistances of AP and P states, respectively. P_T and P_B are the electron spin polarizations in the top FM layer and the bottom

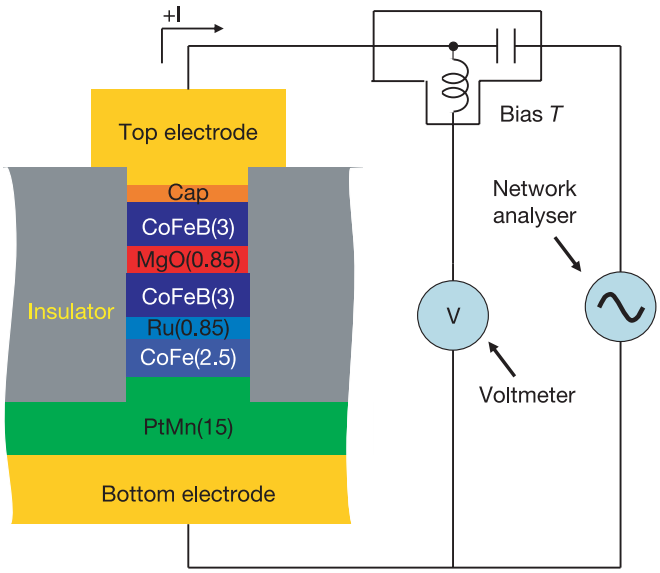

Figure 2.11: Schematic diagram of the experiment setup measuring the rectification voltage in an MTJ. The network analyser was used to apply microwave, and voltmeter was used to measure the rectification voltage. After Tulapurkar et al. [30], used with permission.

layer, respectively, which can be expressed as

$$P_T = \frac{N_T^{\uparrow} - N_T^{\downarrow}}{N_T^{\uparrow} + N_T^{\downarrow}} \tag{2.21}$$

$$P_B = \frac{N_B^{\uparrow} - N_B^{\downarrow}}{N_B^{\uparrow} + N_B^{\downarrow}} \tag{2.22}$$

For materials with spin polarization of 0.6, the TMR ratio can reach the value of $\sim 100\%$, which is already two orders of magnitude higher than that for AMR. In an extreme case, for example, in half metals whose spin polarization is 100%, the TMR ratio can be infinitely large. The angular dependence of the TMR can be expressed as

$$G(\theta) = R(\theta)^{-1} = \frac{G_p + G_{ap}}{2} + \frac{G_p - G_{ap}}{2}\cos(\theta) \tag{2.23}$$

Due to their MR effects being two orders of magnitude greater. MTJ's are expected to have higher microwave rectification sensitivity than the single layer struc-

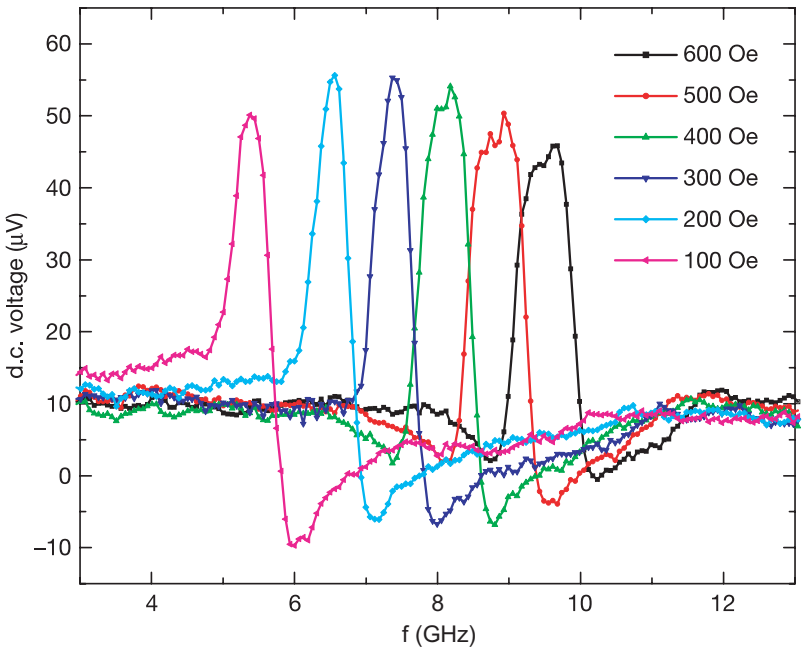

Figure 2.12: Measured rectified voltage as a function of microwave frequency at different external bias. The external magnetic fields range from 100 Oe to 600 Oe. After Tulapurkar et al. [30], used with permission.

tures based on the AMR effect. This expectation is based on the fact that for the same magnetization perturbation, the TMR can induce a larger oscillating resistance and hence a stronger rectification voltage. In 2005, A.A. Tulapurkar et al. first observed a rectification voltage in an MTJ. A schematic diagram of their experiment setup is shown in Fig. 2.11 [30]. The network analyser was used to apply microwave, and voltmeter was used to measure the rectification voltage. An external magnetic field was applied at 30° from the pinning layer magnetization. When microwaves were applied, it drove the precession motion of the free layer, resulting in an oscillating resistance. Following the discussion in section 2.2, a d.c. voltage is expected. In Tulapurkar's experiment, the d.c. voltage as a function of frequency in MTJ was measured at different external magnetic field biases. The result is plotted in Fig.

2.12 for external magnetic fields ranging from 100 Oe to 600 Oe. From the data, a resonance feature of the d.c. voltage is observed. The resonance frequency increases with the external magnetic field strength, in agreement with the FMR feature of the FM layers in an MTJ.

2.4 Seebeck effect and Seebeck rectification effect

Studies have found that the thermal effects such as the Seebeck effect within MTJs can be significant due to their spin polarization [63], which could influence its electrical properties greatly [63; 64; 65]. The Seebeck effect was discovered by T. J. Seebeck in 1821 , when he found that a compass could be deflected by a circuit made from two different metals with junctions at different temperatures [65]. Initially, Seebeck thought it was temperature difference induced magnetism. However, it was quickly realized that this effect was a direct conversion process from temperature gradient to electrical voltage and the compass' deflection was governed by Ampere's law [65].

The Seebeck effect is a direct conversion process from temperature gradient to electrical voltage. Consider a material as shown in Fig. 2.13. The left side of the material is connected to a heat source with temperature T_0, and the right side is connected to another heat source with temperature T_1. In this case, a temperature gradient $\Delta T = T_1 - T_0$ is generated across the material. When a voltage meter is connected to both sides of the material as shown in Fig. 2.13, a d.c. voltage V can be detected. The detected voltage is proportional to the temperature gradient ΔT, and can be written as

$$V = S \cdot \Delta T, \tag{2.24}$$

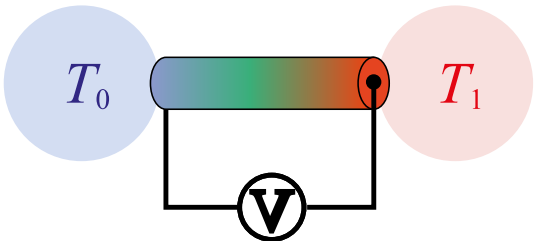

Figure 2.13: Schematic diagram of the Seebeck effect. When there is a temperature difference $\Delta T = T_1 - T_0$ between the two sides of a material, a voltage is generated across the material.

where S is called the Seebeck coefficient. The Seebeck coefficient usually depends upon the material and the temperature. The value of the Seebeck coefficient can range from -100 $\mu V/K$ to 1000 $\mu V/K$ [63].

This effect can be also used to rectify microwaves. When microwaves are injected into the MTJ, the induced microwave current generates Joule heat across the MTJ, which raises the temperature of the MTJ. The schematic diagram of the microwave induced heating is shown in Fig. 2.14. The microwaves act as an a.c. current source (two circles on the top) applied to the MTJ device. The current induced heat transfers to both the cap layer and the substrate of the MTJ, where a heat source (air) at room temperature T_0 is connected.

Since the MTJ's lateral dimension (100-1000 nm) is much larger than its thickness (a few tens of nm), a one dimensional model can be employed to simplify this problem. Along the current flow direction, thermal diffusion equation can be written as [44]

$$C_v \frac{\partial T}{\partial t} = \kappa \frac{\partial^2 T}{\partial x^2} + J^2/\sigma, \tag{2.25}$$

where C_v is the specific heat per unit volume, J is the current density, and σ and κ are the electrical and thermal conductivity, respectively. At the steady state, $\partial T/\partial t = 0$,

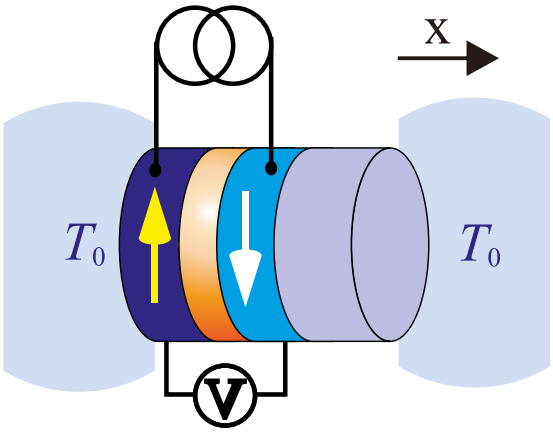

Figure 2.14: A schematic diagram of the microwave induced heating. The microwave acts as an a.c. current source applied to the MTJ. The cap layer and the substrate are connected to the heat source at a temperature T_0.

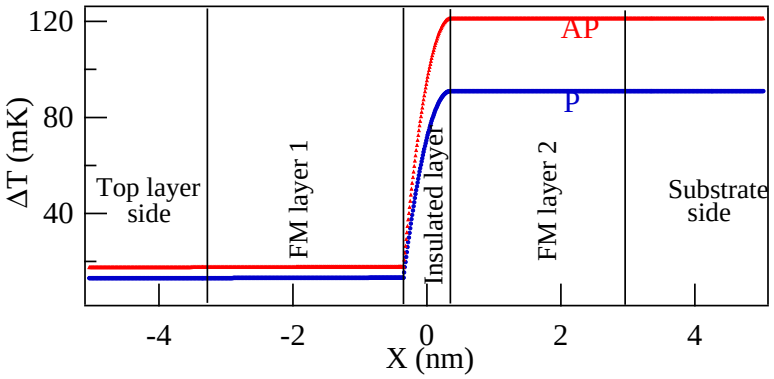

Figure 2.15: The calculated temperature distribution in the MTJ for AP (red) and P (blue) state. The left and right hand side are the top layer and substrate side, respectively. After Zhang et al. [44], used with permission.

Eq. 2.25 can be written as

$$0 = \kappa \frac{\partial^2 T}{\partial x^2} + J^2/\sigma. \tag{2.26}$$

From Eq. 2.26, the temperature profile can be solved as $T = Ax^2 + Bx + C$, where $A = -J^2/(2\sigma\kappa)$ is determined by the material's electrical and thermal conductivity, B and C are determined by the boundary conditions. Air is considered as the heat

(cooling) source with a room temperature of T_0. The temperature at the top of the capping layer and at the bottom of the substrate is T_0 since they are directly in contact with air and the system is in a steady state. Based on this boundary condition, the temperature distribution in each layer can be calculated, as shown in Fig. 2.15. From Fig. 2.15, we can see that there is a huge asymmetry in the temperature distribution. This is due to the fact that usually the thickness of the substrate is on the order of 0.5 mm while the thickness of the MTJ is only a few tens of nm. Also, a temperature gradient ΔT is developed across the MTJ and mainly occurs in the tunnel insulated layer since the tunnel insulated layer contributes the most to the resistance of the MTJ device and most of the Joule heat is generated in the tunnel insulated layer. Note that in this discussion, the tunnel insulated layer is treated as a conductor with a conductivity much smaller than the other layers.

For a certain MTJ device (fixed geometry), the temperature gradient ΔT is proportional to the generated Joule heat I^2R, and thus is proportional to the injected microwave power P_{MW}. The rectified d.c. voltage V can therefore be expressed as

$$V = S \cdot \Delta T \approx S \cdot I^2 \approx P_{MW}, \tag{2.27}$$

where S is the Seebeck coefficient of the MTJ device. Note that V is induced by the Seebeck effect. For this reason, the thermoelectric rectification effect is called the Seebeck rectification effect. The Seebeck rectification effect in an MTJ was first reported by our group in 2012 [44]. In this experiment, it was found that the rectification voltage was linearly dependent on the microwave power, as expected. The experimental data are shown in Fig. 2.16, where the rectification voltage in both the P state and the AP state is measured. The difference in the slopes indicates that

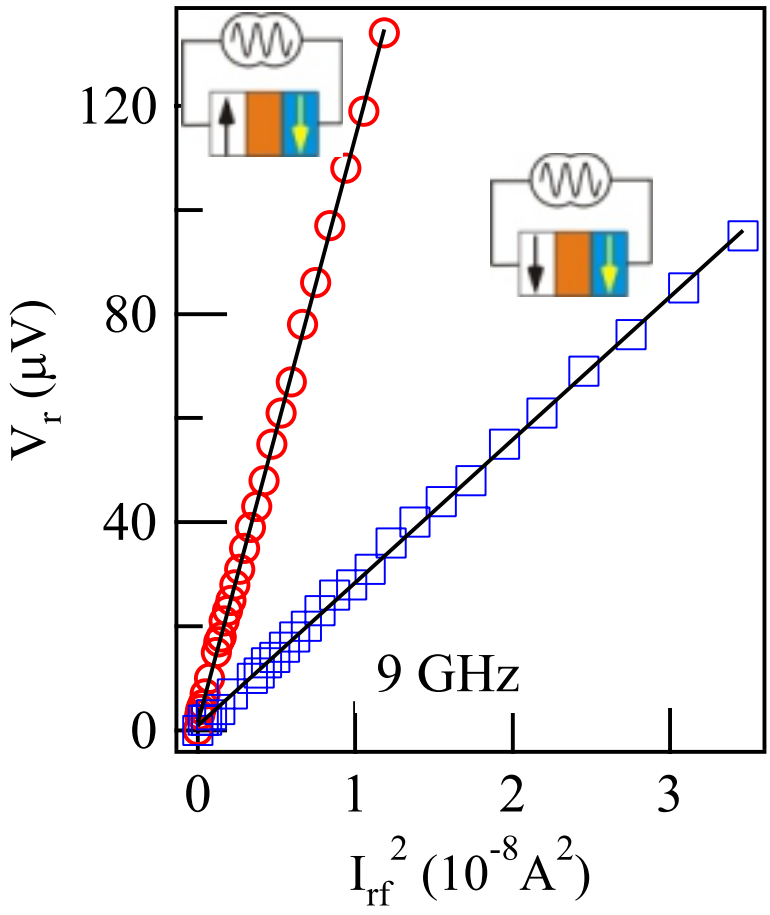

Figure 2.16: The Seebeck rectification voltage measured as a function of microwave power at a microwave frequency of 9 GHz. The red circles and the blue rectangles are the results obtained when the MTJ is in AP and P state, respectively. The lines are the linear fits for each state. After Zhang et al. [44], used with permission.

for different states, even for the same sample, the Seebeck coefficient can be different [44].

The Seebeck rectification effect is sensitive to thermal boundary conditions. When a laser beam is applied to the top of the capping layer of the MTJ, the temperature of the capping layer is locally raised by the laser. Therefore, the Seebeck rectification voltage will be suppressed by such an external heating effect. A schematic diagram is shown in Fig. 2.17 to illustrate such a suppression effect.

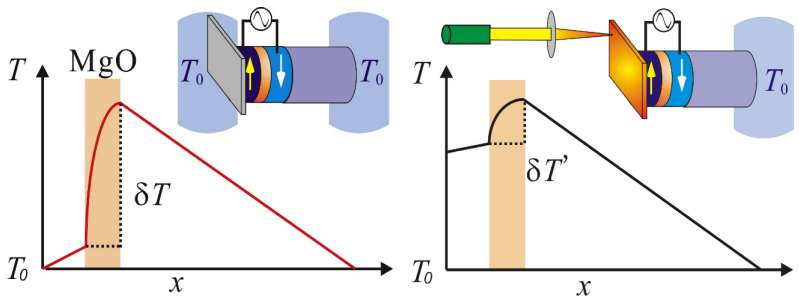

Figure 2.17: Schematic diagram of temperature gradient without laser heating and with laser heating. (Left) Without the laser, the microwave induced temperature difference across the MgO layer is δT (indicated by the dark area). (right) With the laser applied, the microwave induced temperature difference across the MgO layer is reduced to $\delta T'$ (indicated by the dark area). After Zhang et al. [44], used with permission.

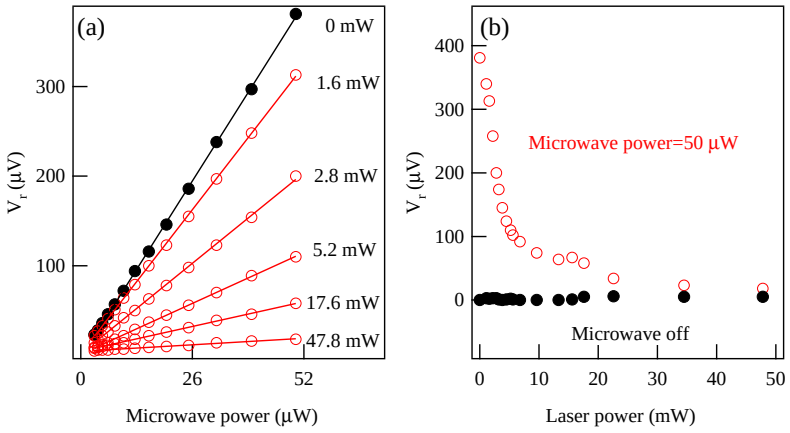

Figure 2.18: (a) Microwave power dependence of the Seebeck rectification voltage V_r measured at different laser power ranging from 0 to 47.8 mW. (b) Laser power dependence of V_r measured at fixed microwave powers of 50 μW and 0. After Zhang et al. [44], used with permission.

This suppression effect was observed experimentally by Zhang [44]. As shown in Fig. 2.18(a), at a fixed laser power, the rectification voltage V is proportional to the input microwave power, which is as expected. When there is no laser applied, V can be as high as 300 μV at a 50 μW microwave input power. When a laser is applied

to the MTJ, V decreases with respect to the laser power. When the laser power reaches 47.8 mW, the rectification voltage V is totally suppressed to 0, which can be clearly observed in Fig. 2.18(b). By this laser suppression experiment, the Seebeck rectification effect is further confirmed.

In summary, the rectification voltages V_r produced from both the spin rectification effect and the Seebeck rectification effect are linearly dependent with incident microwave power, which makes the spintronic devices good candidates for microwave sensors. The differences between the two mechanisms are also obvious: The voltage produced from the spin rectification effect is related to both the microwave e-field and h-field as well as their relative phase while the voltage produced from the Seebeck effect only depends on the microwave e-field.

Chapter 3

Microwave amplitude detection using spintronic sensors

3.1 Introduction

Since microwaves can penetrate optically opaque materials and non-conducting materials, microwaves can interact with subsurface structures in addition to the surface structures [66; 67; 68]. Therefore, microwaves have the ability of subsurface detection to reveal hidden objects or defects by making an image of the contrast of dielectric properties of the hidden objects and surrounding materials. Since microwaves are a kind of non-ionizing radiation, it is reasonably safe when used under the power limitation given by government regulations (1.6 W/kg for local absorption and 0.08 W/kg for whole body absorption) [37]. This gives microwave imaging systems significant potential for industrial design, security services, and biomedical imaging [69; 70; 71].

Developments in spintronic techniques have made the spintronic sensor a promising alternative to traditional sensors for microwave imaging. One of the major discoveries in this area is the spin rectification effect discussed in Section 2.3, which is the generation of a d.c. voltage due to the coupling between the microwave field and the material's dynamic magnetization [30; 39]. The requirement for a static external magnetic field in the spin rectification effect cannot always be satisfied in microwave imaging systems. Because the spatial distribution of scattered microwave fields measured by a microwave imaging system may be distorted by the hardware required for the external magnetic field, a microwave imaging system based on a spintronic sensor working at zero external magnetic field is desired.

In this chapter, a far field microwave imaging system working at zero external magnetic field is developed using a spintronic sensor. This sensor employs the Seebeck rectification effect, which makes zero field microwave rectification possible. Thanks to its high conversion efficiency, the far field imaging system can directly measure the coherent spatially-scattered microwave field distribution in free space. The pattern obtained is confirmed by numerical simulation using finite element software COMSOL Multiphysics. By analysing the scattered microwave pattern, the presence of hidden objects may be revealed. In addition, the spintronic sensor was used to measure the radiation pattern of an antenna. This could assist in antenna design.

3.2 Spintronic sensor based microwave amplitude measurement

The key element of the spintronic microwave sensor described in this chapter is an MTJ structure. The MTJ devices were provided by Everspin Technologies. MTJs were grown on a Si substrate covered with 200 nm SiO_2 and contained the following layers: PtMn(20 nm)/CoFe(2.27 nm)/Ru(0.8 nm)/CoFeB(2.2 nm)/CoFe(0.525 nm)/MgO(1.2 nm)/CoFeB(2.5 nm). The buffer and capping layers are TaN and Ta, respectively. The MTJ stack is patterned into an elliptical shape with short axes from 63 nm to 120 nm and an aspect ratio between 1.8 and 3.5, using photo-lithography and reactive ion etching [44], a photograph of the MTJ sensor is shown in Fig. 3.1.

The thickness of the MgO barrier is only 1.2 nm, so that the electrons can tunnel through, providing a tunnelling resistance. Due to different electron tunnel efficiency at parallel (P) and anti-parallel (AP) states (depending upon the configuration of the magnetization of the two ferromagnetic layers), the MTJ device shows different resistances for different magnetization configurations.

The schematic setup for the MTJ's characterization is shown in Fig. 3.2, including a sourcemeter (Keithley 2400), a broadband microwave generator (Agilent E8257D), a lock-in amplifier (Stanford Research Systems SR830), an electromagnet (LakeShore EM4-HVA) and an MTJ device. In the d.c. property measurement, the MTJ device was connected with the sourcemeter and placed in the gap of the electromagnet, as shown in Fig. 3.2(a). A d.c. current bias of 10 μA was applied to the MTJ device using the sourcemeter. Meanwhile, the resistance of the MTJ was measured by the

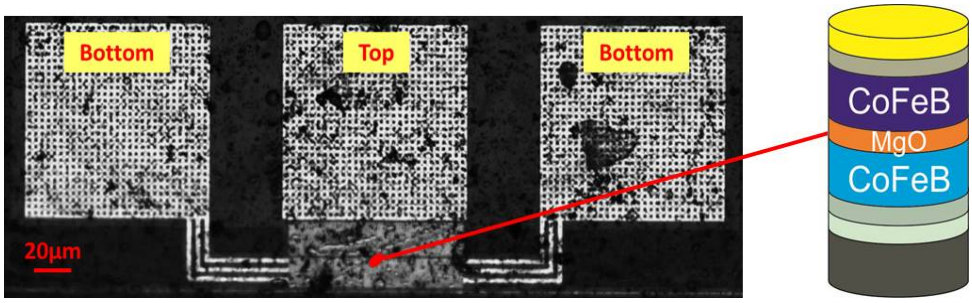

Figure 3.1: Photograph of the MTJ device. The MTJ is red ellipse in the center, whose schematic diagram is shown in the right side of the figure. The three squares are the electrodes of the device.

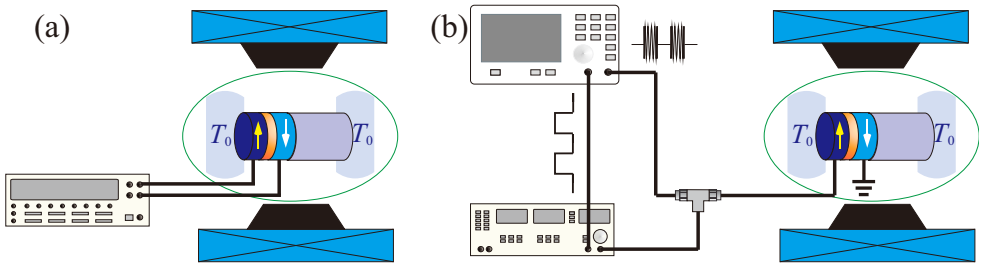

Figure 3.2: (a) Schematic setup for the measurement of the MTJ's d.c. properties, including a digital sourcemeter, an electromagnet and an MTJ device (not to scale). (b) Schematic setup for the measurement of the MTJ's a.c. property, including a broadband microwave generator, a lock-in amplifier, an electromagnet and an MTJ device (not to scale). After Gui et al. [47], used with permission.

sourcemeter. Applying a static magnetic field in-plane with the free layer, the MTJs show single domain magnetization reversal, as seen in Fig. 3.3 for a sample with long and short axes of 190 and 100 nm, respectively. When the external magnetic field is positive and larger than the coercive field, the MTJ is in the P state and shows a resistance of 618 Ω. When the magnetic field is negative, the MTJ shows a resistance of 1068 Ω.

When microwaves are injected into the MTJ, Joule heat is generated by the microwave induced current (i). Due to the asymmetric geometry of the MTJ, a tem-

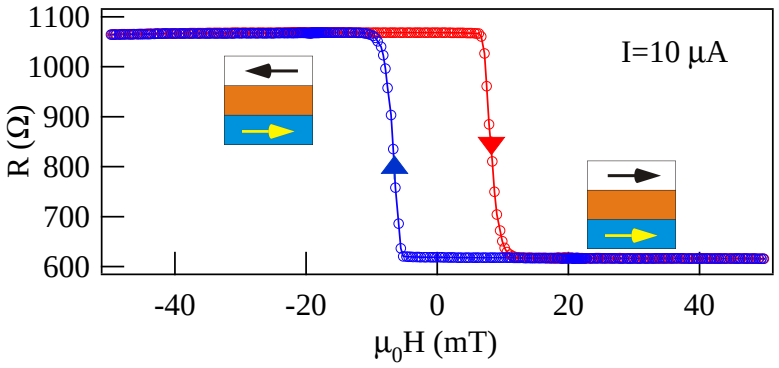

Figure 3.3: The resistance of an MTJ as a function of the magnetic field and its sweeping direction. The d.c. current bias is 10 μA. The MTJ is patterned in an elliptical shape with long and short axes of 190 and 100 nm, respectively. After Fu et al. [46], used with permission.

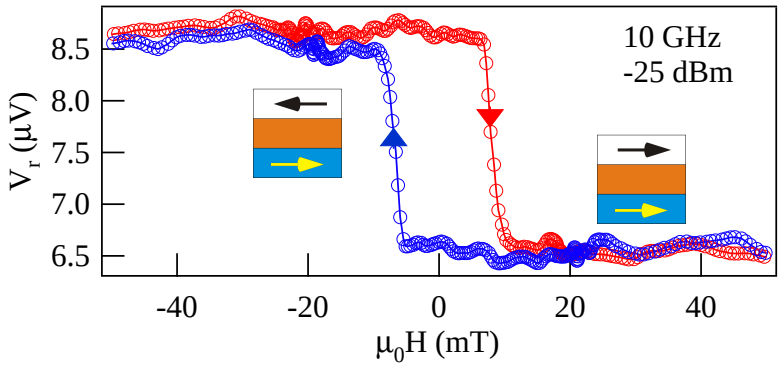

Figure 3.4: The Seebeck rectification measured at $\omega/2\pi = 10$ GHz as a function of the magnetic field. The incident microwave power injected into the MTJ is -25 dBm (~ 3.2 μW) after power calibration. After Fu et al. [46], used with permission.

perature gradient ΔT across the junction is formed, which is converted into a d.c. voltage V_r by the Seebeck effect, following the relationship of $V_r = S \cdot \Delta T \propto i^2$. This thermal mechanism is discussed in detail in Chapter 2.

As shown in Fig. 3.2(b), a microwave at a frequency of 10 GHz is applied to the MTJ, with a power of -25 dBm (~ 3.2 μW). The microwave was amplitude modulated (AM) at 8.33 kHz, so that the rectification voltage could be tracked by

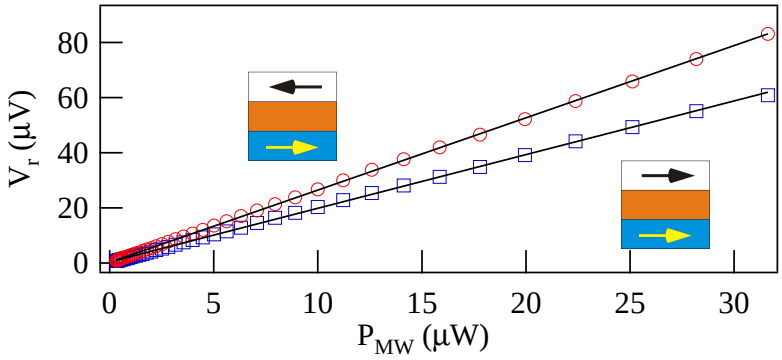

Figure 3.5: The Seebeck rectification V_r (symbols) as a function of the microwave power P_{MW}, which appears as a linear relation indicated by the solid lines. After Fu et al. [46], used with permission.

a lock-in amplifier at the same modulation frequency. Like the resistance loop, the rectification voltage also shows a loop with respect to the external magnetic field, as shown in Fig. 3.4. Here, the transition takes place at the coercive field of 5.5 mT. From Fig. 3.4, it is clear that the MTJ in both the P and AP states can rectify microwaves and that the MTJ in the AP state produces a larger voltage for a given microwave power. Tuning the incident microwave power, it is found that the rectification voltage V_r is linearly dependent upon the incident microwave power, as shown in Fig. 3.5. From Fig. 3.5, we can see that the MTJ in both the P and AP states has a linear relation and the MTJ in the AP state has a larger sensitivity, as expected. In this experiment, the measured sensitivity of the MTJ is 2.6 and 2.0 mV/mW for the AP and P states, respectively. In the following experiments, unless specified, the MTJ is always employed in the AP state.

3.3 Scattered microwave detection in free space using a spintronic sensor

In previous experiments [30; 32; 63; 34; 44], microwaves were directly injected into the MTJ via coaxial cables. Although the MTJ has a response to the microwaves, it is not enough to claim that it directly senses the scattering microwaves whose intensities have specific spatial distributions, depending upon the properties of the target. In order to demonstrate that spintronic sensors have the capability to detect scattering microwaves, we have investigated the microwave distribution scattered by an aluminum (Al) strip.

The experimental setup for microwave intensity distribution detection is shown in Fig. 3.6. Microwaves generated by the microwave generator (Agilent E8257D) were fed to a standard C-band (4-8 GHz) horn antenna (ATM 187-440-6) with an output power of 20 dBm via a coaxial cable. The microwaves were reflected by a flat Al strip (width=5.08 cm, thickness=0.64 cm) positioned at a distance of 24 cm, at a 45 degree incidence angle.

To precisely measure the microwave intensities, a standard lock-in technique was employed. The microwave signal was amplitude modulated (AM) with an 8.33 kHz square wave and was triggered by the lock-in amplifier (SR830), enhancing the signal/noise ratio, permitting Seebeck rectified voltages as weak as about 20 nV to be detected (this corresponds to a microwave with a power of about 8 nW being injected to the MTJ). It is notable that the wavelength of the microwaves used is about λ=5$\sim$7.5 cm, which is comparable to or larger than the width of the aluminum strip.

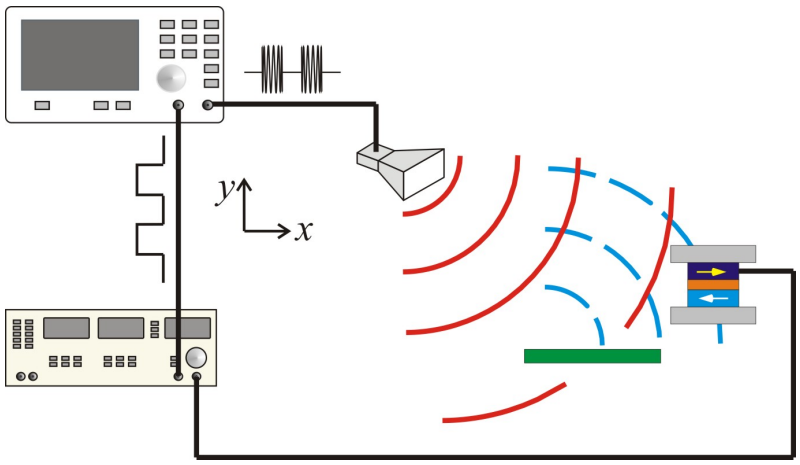

Figure 3.6: A schematic diagram of the experimental setup for scattered microwave detection. Microwaves emitted from the horn antenna were reflected by the target and collected by the sensor. The voltage across the sensor was recorded by the lock-in amplifier. After Gui et al. [47], used with permission.

Like optical waves, microwaves obey the standard laws of geometrical optics. When the target size is comparable to the microwave wavelength, the processes of reflection, refraction and diffraction are complicated. Even though our apparatus only contains a horn antenna and an aluminum strip, the microwave propagation pattern was very complex, since the reflected microwaves interfered with the waves in free space. In order to have a sense of the microwave intensity pattern, COMSOL Multiphysics 4.2 was employed to simulate the microwave field distribution.

A two dimensional simulation was performed, using the RF module of COMSOL Multiphysics. A line source located from (-17, -10.5) cm to (-12.2, -5.6) cm was employed as the microwave source, emitting microwave with electric field polarized in the z direction. A 5 cm wide reflector with its left edge placed at (-1.5, -25) cm was employed to simulate the aluminum strip. All the simulation boundaries were transparent so that no microwaves were reflected from the boundaries. The mesh size

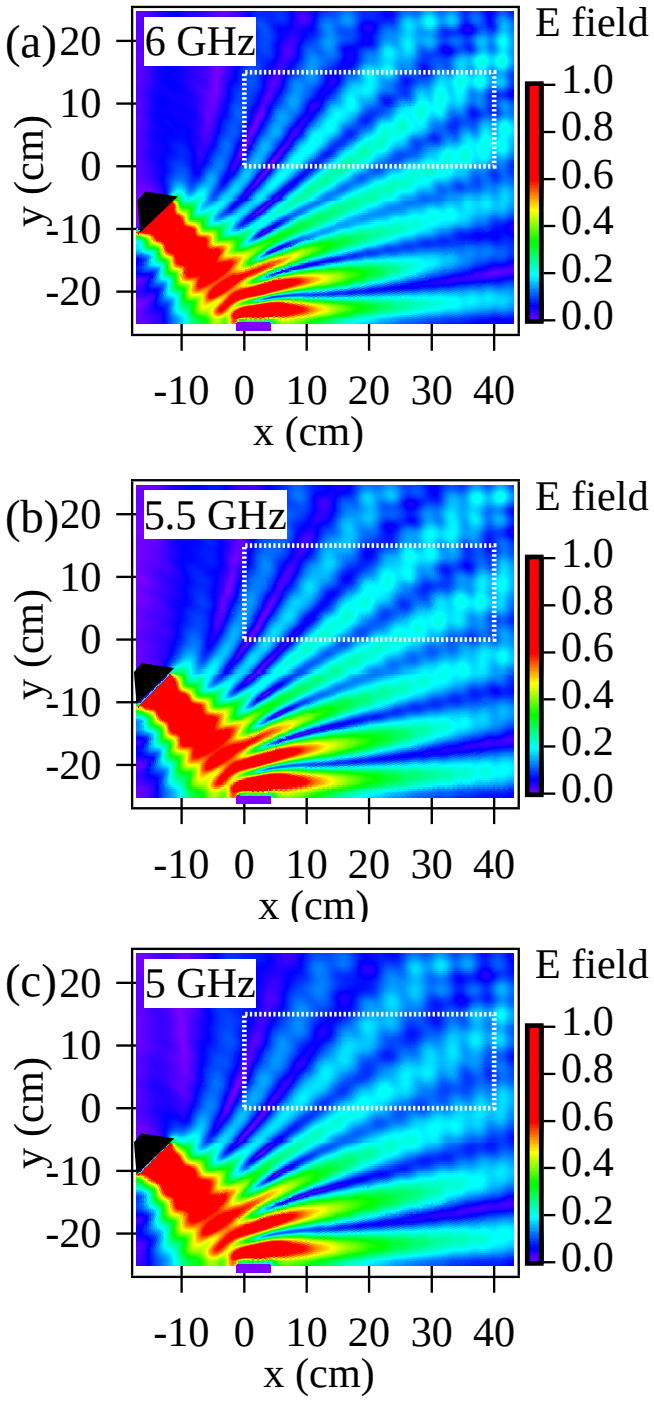

Figure 3.7: Simulated results of the microwave field amplitude at $\omega/2\pi$=(a) 6 GHz, (b) 5.5 GHz, (c) 5 GHz. Microwaves generated from the black quadrilateral are reflected by the target whose left edge locates at (-1.5, -25) cm. The dashed rectangle indicates the area of interest which was investigated in the experiment. After Gui et al. [47], used with permission.

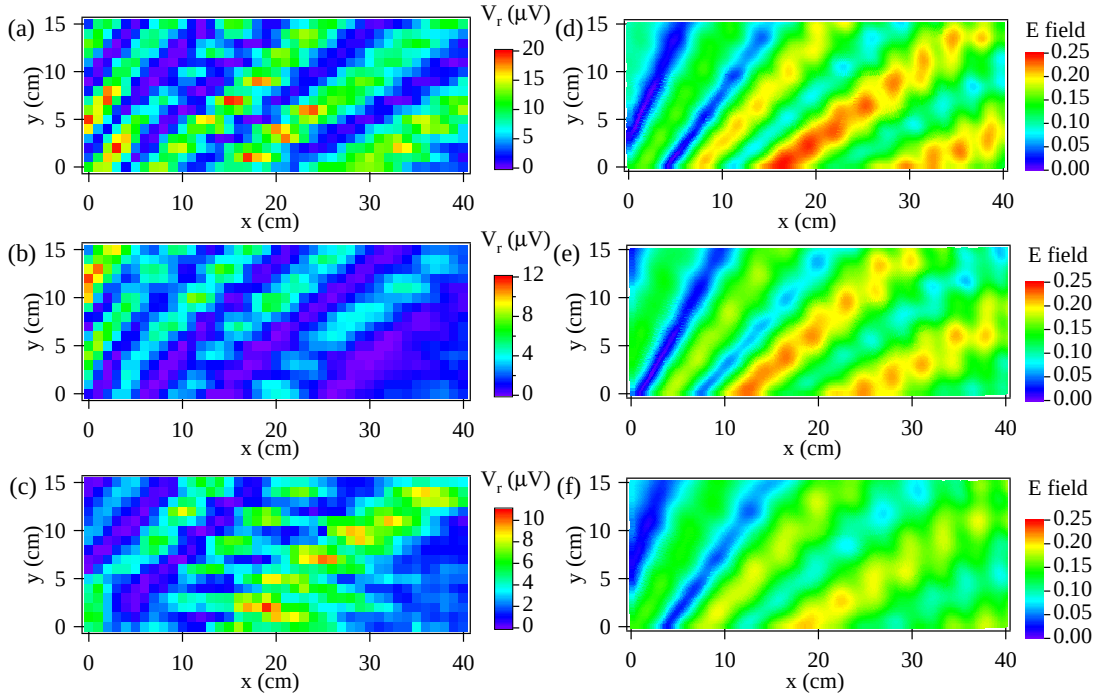

Figure 3.8: Experimental results of the microwave field amplitude at $\omega/2\pi$=(a)6 GHz, (b)5.5 GHz, (c)5 GHz, respectively. Zoom in simulated results of the microwave field amplitude at $\omega/2\pi$=(d)6 GHz, (e)5.5 GHz, (f)5 GHz, respectively.(Colour was rescaled for clarity.)

in the simulation was limited by the memory of the computer (2 GB). The simulation results for microwaves at 6 GHz, 5.5 GHz, and 5 GHz are shown in Fig. 3.7(a), (b) and (c), respectively. In the simulation result, the black quadrilateral is the horn antenna and the rectangle at the bottom is the aluminum strip. The plots in Fig. 3.7 are the microwave intensity distribution, where the color plot is tuned to enhance the contrast in the area of interest, as indicated by the dotted lines. In the simulation pattern, we can see that the incident wave from the microwave source has the strongest intensity (as expected). In addition, a series of side lobes are seen connected to the incident beam. These side lobes are considered to be the result of interaction between the incident and the reflected beams.

In the experiment, a spintronic microwave sensor connected to a lock-in amplifier was used to detect the microwave field. The scan area ranged from (0, 0) cm to (40, 15) cm, and is indicated by the dotted lines in Fig. 3.7. This area was selected to minimize the effects of microwaves scattering off the sensor and its holder. The spintronic sensor was manually scanned in the x and y directions in the 40×15 cm area with steps of 1 cm. The manual scan was performed on the base of a grid paper. At each scan position, the rectification voltage measured by the lock-in amplifier was recorded using LabVIEW 2011. In this way, a two-dimensional image of the microwave intensity distribution was generated. It took hours to finish one image due to the manual scan process. The observed V_r are plotted in Fig. 3.8(a), (b) and (c) when microwaves are at a frequency of 6 GHz, 5.5 GHz, and 5 GHz, respectively. The simulation results are plotted in Fig. 3.8(d), (e) and (f) for a direct comparison. All the figures were plotted using Igor Pro. From the experimental images, a series of lobes are also obtained. The positions of maximum and minimum V_r shift along the x and y directions and are in agreement with the position shift of the maximum and minimum microwave intensities in the simulation. In each image, 6, 5.5 and 4 sets of lobes are observed for 6 GHz, 5.5 GHz and 5 GHz, respectively. In Fig. 3.8(b), the bright lobe in the right bottom corner is considered as a half set of lobes since it is not completely observed (the dark lobe to the right of the lobe does not appear). Similarly, in the simulation, 5.5, 4 and 3.5 sets of lobes are observed in the area of interest for 6 GHz, 5.5 GHz, and 5 GHz, respectively. Both experiment and simulation show that the number of bright lobes decreases as the frequency decreases. This is considered as a result of the increasing microwave wavelength.

It is worth noting that the microwave source in the simulation was a plane wave source, which is not exactly the case in the experiment. Other complexities in the experiment such as the surrounding objects are not considered in the simulation. Therefore, the comparison between the simulation and the experiment should be regarded as qualitative. From a qualitative point of view, using the trace of maximum signal's position shift and the decrease in the number of bright lobes, we can conclude that the simulation and the experimental results are in agreement. Such agreement shows that the spintronic sensors have the ability to detect microwave spatial distribution in free space.

3.4 Hidden object detection using a spintronic sensor

In contrast to visible light and infrared, microwaves can pass through non-metallic physical barriers such sand,rocks, wood and clothes, and interact with dielectric targets beneath the surface. Embedded targets made up of different materials may reflect different intensities of microwaves since different materials have different reflectivity coefficients governed by dielectric constants. Their penetration ability makes microwaves a powerful tool in non-destructive testing, which is widely used in industry, biomedicine, security services, and civil engineering. In this section, using a horn antenna as a transmitter and an MTJ based sensor as a receiver, we also demonstrate that non-destructive imaging can be achieved using microwave reflection imaging.

As shown in Fig. 3.9, a standard X-band horn antenna (8-12 GHz) and an MTJ

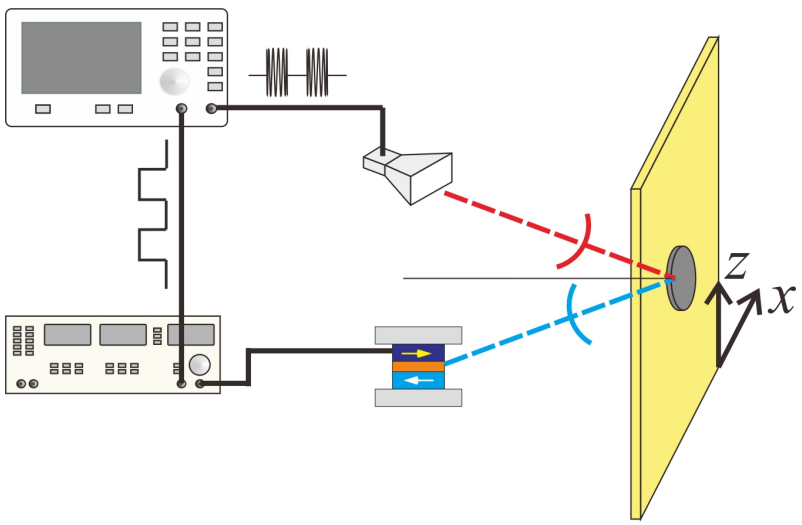

Figure 3.9: Schematic view of the hidden objects detection system. The target is hidden behind a 3.0 cm thick plywood wall and is scanned along the x and z direction.

based sensor were used as the microwave transmitter and receiver, respectively. A lock-in technique was employed to increase the signal/noise ratio. A 50 cm×50 cm sheet of plywood with a thickness of 3.0 cm was placed 15 cm away from the antenna at an angle of 45 degrees. The MTJ sensor was placed across from the horn at a distance of 15 cm from the surface and positioned so that the waves from the horn, which reflect off the surface at an angle of 45 degrees, would travel directly to the sensor. The target of interest was fastened to the side opposite to that of the horn and detector. Therefore, the target was hidden by the surface from the sensor side. Scanning the surface in the x-z plane, we recorded the microwave field distribution scattered by the surface using the MTJ sensor.

In the experiment, a 7.12 cm diameter Al disc, a 5.08 cm diameter Al disc and a 7.12 cm diameter acetal disc ($\varepsilon = 3.8$, thickness=0.64 cm) were investigated at a frequency of 10.5 GHz. The scan area was 18×30 cm in the $x - z$ directions with the

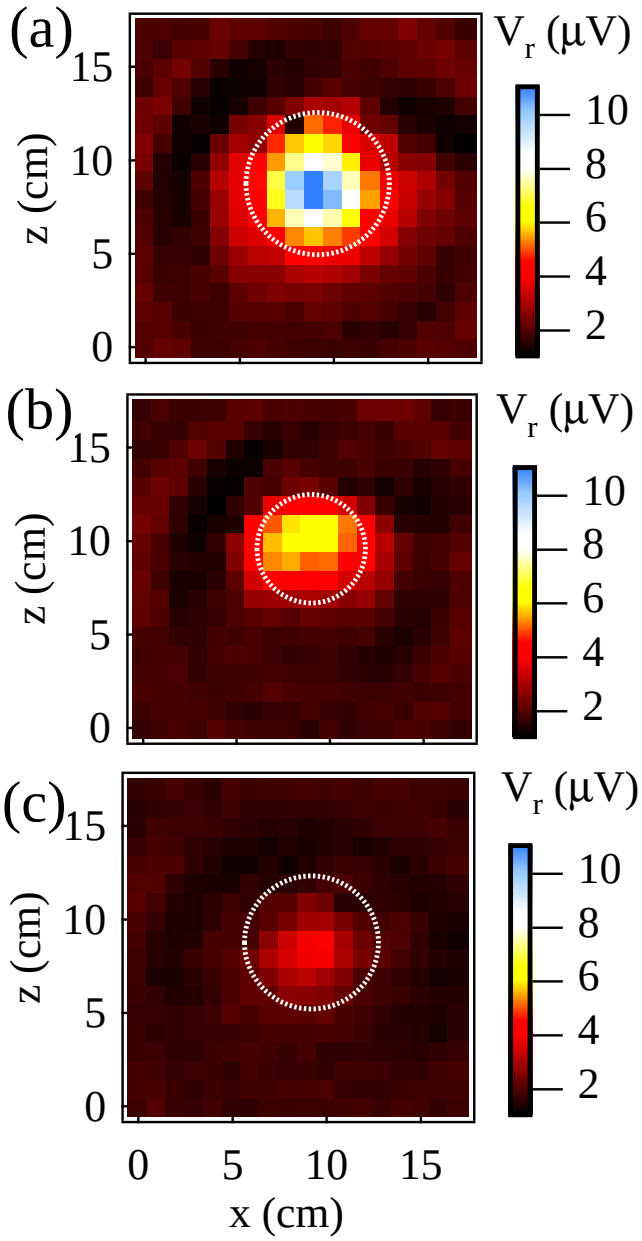

Figure 3.10: (a)Microwave reflection pattern of a hidden Al disc with a diameter of 7.12 cm. (b)Microwave reflection pattern of a hidden Al disc with a diameter of 5.08 cm. (c)Microwave reflection pattern of a hidden acetal disc with a diameter of 7.12 cm. The dotted line in these figures indicates the position of the target. After Fu et al. [46], used with permission.

center coinciding with the target's center. The measured voltage pattern across the sensor is plotted in Fig. 3.10(a), (b) and (c), respectively. The color intensity scale in the figures are the same so that they can be directly compared. As shown in Fig. 3.10(a), (b) and (c), the voltage across the sensor is significantly influenced by the embedded target. At the center of each pattern, there is a bright area corresponding to the target. The dotted circle in Fig. 3.10(a), (b) and (c) indicates the size and position of the target. The difference in the maximum voltage indicates that the targets have different microwave reflection abilities. From Fig. 3.10, we can see that the 7.12 cm diameter Al disc reflects the most microwave power while the 7.12 cm diameter acetal disc reflects the least microwave power. Since more than one factor, such as the target size, material, and shape, can influence the microwave intensity pattern, it is difficult to retrieve quantitative information about the target in this experiment. However, based on the fact that different responses are obtained from different targets, this experiment shows the potential to distinguish different embedded targets using a microwave system based on spintronic sensors.

For the same experimental setup, microwave frequencies ranging from 8-12.5 GHz with an interval of 0.5 GHz were employed to detect the 7.12 Al disc. The recorded amplitude distributions for different frequencies are plotted in Fig. 3.11. As shown in Fig. 3.11, there is some correlation between the disc position and the microwave intensity distribution. For example, at a frequency of 10.5 GHz, there is a bright area at the center of the microwave intensity pattern, which corresponds to the appearance of the Al disc, as indicated by the dotted circle. Similar features are observed when the microwave frequency is 11.5 GHz and 12.0 GHz. However, at other frequencies, the

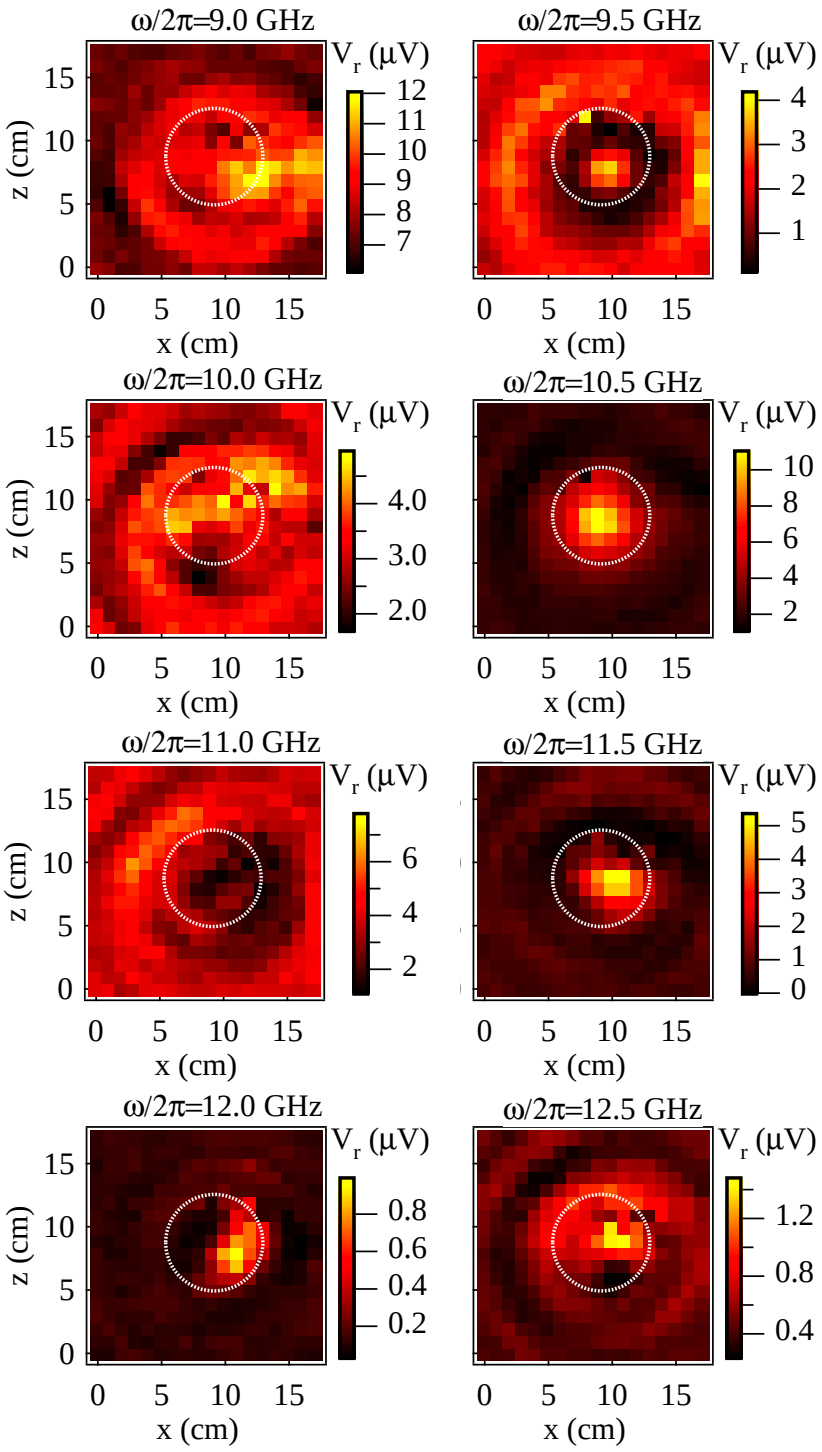

Figure 3.11: The microwave reflection pattern for a hidden object (a 7.12 cm Al disc) for frequency ranging from 9.0 GHz to 12.5 GHz. The dotted line in these figures indicates the position of the target. After Cao et al. [72], used with permission.

intensity pattern is so complex that there is no such bright center indicating the Al disc's position. At frequencies of 9.5 GHz and 11.0 GHz, there is even a dark center in the intensity pattern. At all frequencies, a diffraction effect is more or less observed, as shown by the diffraction circles around the center. These complex patterns are due to the correlations between scattered microwaves, objects, and the environment. Even for the same configuration, microwave intensity patterns are still so different. This effect is expected since the scattered microwave spatial distribution is strongly dependent on the microwave wavelength. It seems that more effort is needed to reveal what's beneath the surface. In principal, microwave reconstruction techniques combined with amplitude and phase information have the ability to determine the shape of a hidden target, which will significantly enhance the capabilities of the spintronic microwave imaging technique. One of the microwave reconstruction techniques will be discussed in detail in Chapter 4.

3.5 Adapting spintronic sensors for microwave antenna design

A spintronic sensor's capability to detect microwave intensity field distributions can be adapted for antenna design procedures. An antenna's radiation pattern is one of the most important features which needs to be carefully measured in the antenna design procedure [73; 74; 75]. In general, measurement of such radiation patterns requires scanning a small probe antenna over the planar surface of the antenna, both in the near field and far field. This is not an easy task since the microwave radiation

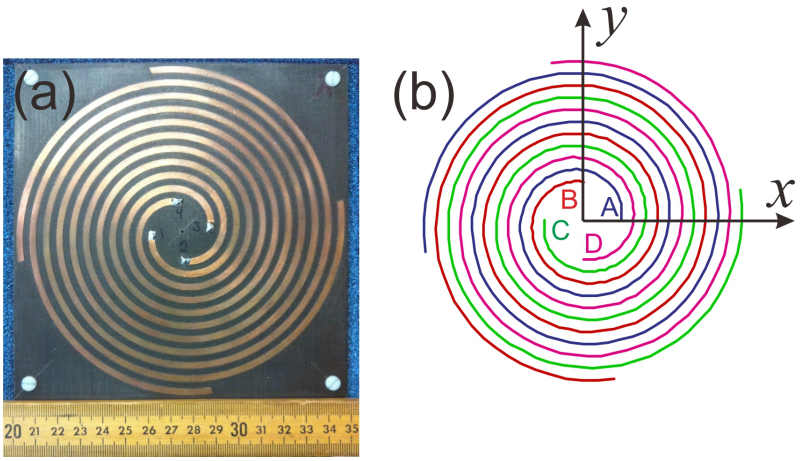

Figure 3.12: (a)Photograph of the measured four-arm spiral antenna. (b) Schematic diagram of the four-arm spiral antenna (top view). The four arms are identical spiral wires placed with the same origin but with initial point at angle 0°, 90°, 180°, and 270° with respect to the x axis, respectively. After Gui et al. [47], used with permission.

pattern may be distorted by the probe antenna. As discussed in previous sections, the MTJ has the advantages of broad bandwidth, small size, and ease of detection of d.c. signal, which make it a good tool for assisting in antenna design and miniaturization.

In this section, a four-arm spiral antenna's radiation pattern was measured to demonstrate such an application using an MTJ microwave sensor. Spiral antennas can emit circularly polarized microwaves and have been widely used for direction finding, radar, navigation and satellite communications[76]. The four-arm spiral antenna contains four identical spiral wires placed in the same plane. The only difference is that the initial point is at an angle of 0°, 90°, 180°, and 270° with respect to the x axis as shown in Fig. 3.12 [47]. The antenna's radiation pattern can be changed by tuning the phase between the four arms. This is the novelty of this design (Table 3.1). A ring conductor model can be employed to understand this effect in the simplest picture. As shown in Fig. 3.13(a), when the circumference $2\pi r$ of the ring is matched

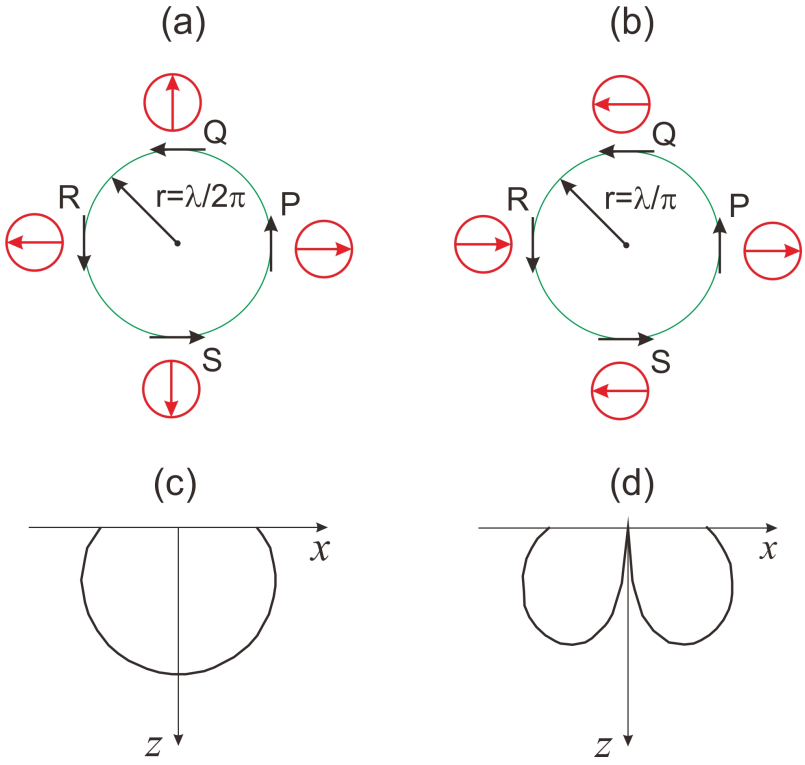

Figure 3.13: A simple way to understand the phase properties of (a) Mode 1 and (b) Mode 2 by representing the spiral antenna as a circular conductor. The black arrows indicate the direction of the uniform progressive microwave current while the red arrows inside a small circle indicate the travelling phase of the current. Principle radiation patterns of the four-arm spiral antenna are (c) Mode 1 and (d) Mode 2. After Gui et al. [47], used with permission.

with the wavelength λ of the microwave current, microwaves at point Q, R, S in the ring will have a 90°, 180°, and 270° travelling phase delay compared with point P, as shown by the red arrows inside the small circle. Microwaves at point R that have an opposite current flow direction with respect to point P, as indicated by the black arrows, will compensate the 180° phase delay. Thus, microwaves at point R and point P will be exactly in phase. Meanwhile, the microwaves at point Q are perpendicular to that at point P. In this case, the ring will generate a circular polarized microwave beam, whose radiation pattern is shown in Fig. 3.13(c). In the four-arm antenna,

Table 3.1: The feed excitations for the first two modes of four-arm spiral antenna

	A	B	C	D
Mode 1	0°	−90°	−180°	−270°
Mode 2	0°	−180°	0°	−180°

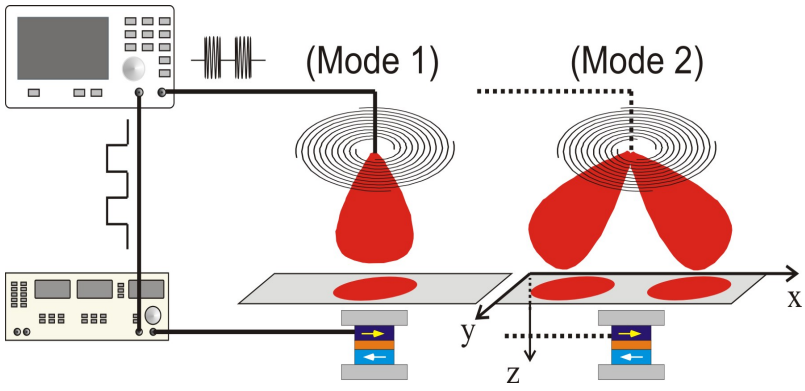

Figure 3.14: A schematic of the experimental setup for the antenna radiation pattern measurement. The sensor is scanned in x-y plane with different z values. After Gui et al. [47], used with permission.

Arms A, B, C, D can be regarded as points P, Q, R, S, respectively. When setting a 90° phase shift in each arm's feeding line, as shown in the Mode 1 in Table 3.1, the four-arm antenna will generate a circular polarized microwave beam in the same way.

The special feature of the four-arm antenna is the phase controlled radiation pattern. For example, when tuning the phase of each arm to $\phi_A = \phi_C = 0°$, $\phi_B = \phi_D = -180°$, a second mode will be generated, i.e., Mode 2 in Table 3.1. This corresponds to the case when $2\pi r = 2\lambda$ in the ring conductor model. As shown in Fig. 3.13(b), the microwaves at point P and R are in anti-phase because of a 360° difference in travelling phase and an opposite current flow direction. Similarly, microwaves at point Q and point S are also in anti-phase. In this mode, microwaves are cancelled at the center of the circle, whose radiation pattern is shown in Fig.

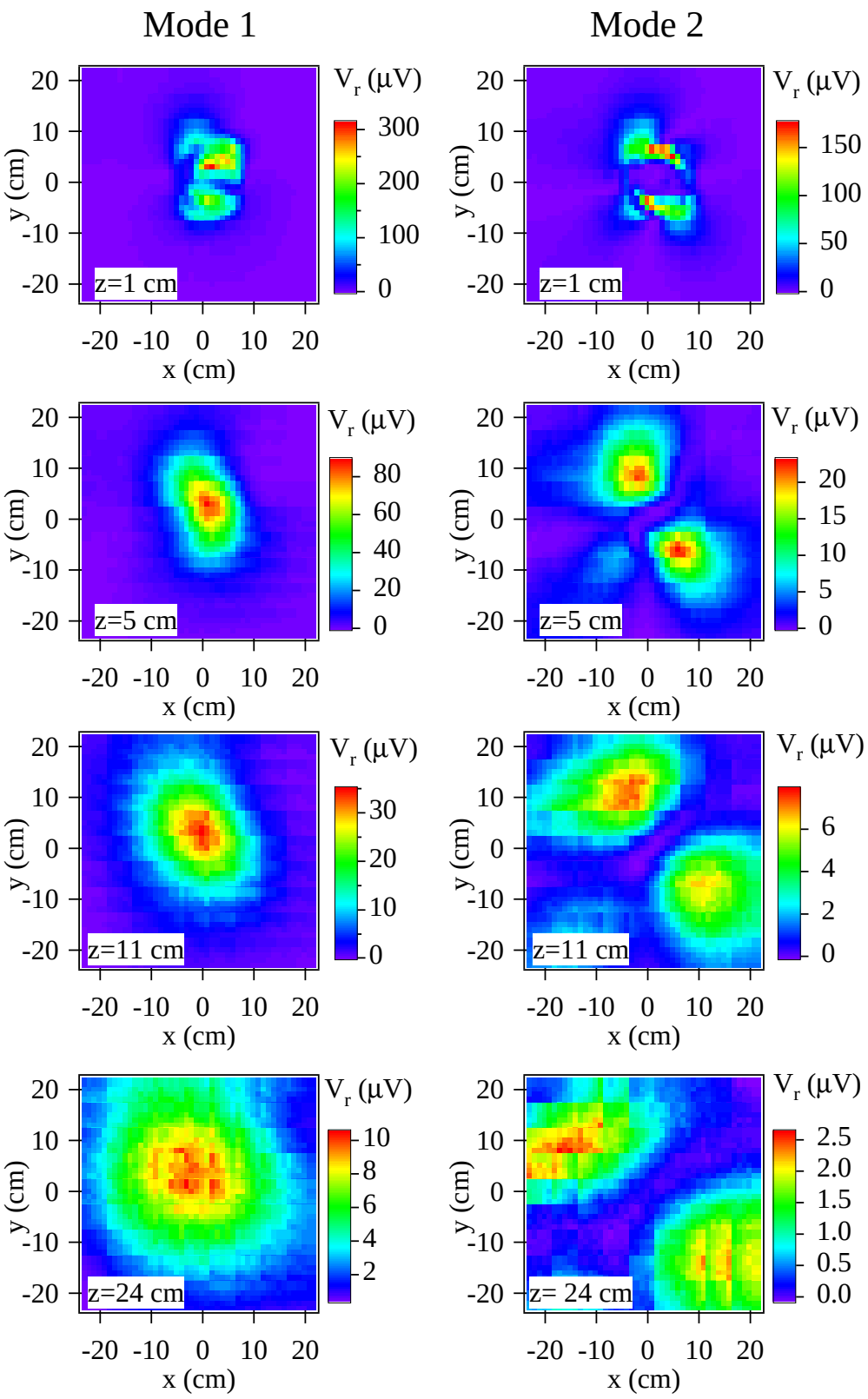

Figure 3.15: Radiation patterns measured by the MTJ based spintronic sensor for Mode 1 and Mode 2 at z distances of z=1, 5, 11 and 24 cm at $\omega/2\pi$=1.1 GHz. After Gui et al. [47], used with permission.

3.13(d).

An MTJ based spintronic sensor was employed to record the four-arm antenna's radiation pattern. The schematic diagram of the experiment is shown in Fig. 3.14. Microwaves at a frequency of 1.1 GHz were directly fed into the antenna in Mode 1 and 2. The MTJ sensor was scanned in the x-y plane, driven by a step motor in the x and y directions with a step of 1 cm. At each position, the rectification voltage was measured by the lock-in amplifier. The experiment was automatically controlled using LabVIEW 2011. In the experiment, the scan aperture was 40 $\times$ 40 cm, where the center of the aperture corresponded to the center of the antenna. The recorded voltage patterns at different z values are plotted in Fig. 3.15, where the first column and second column are the results of Mode 1 and Mode 2, respectively. The data is represented using Igor Pro. From Fig. 3.15, it is observed that the antenna has a maximum radiation intensity at the center for Mode 1, while it has a minimum radiation intensity at the center for Mode 2. The radiation pattern also grows with respect to the z value, which is in agreement with the theoretical prediction.

3.6 Summary

We have demonstrated the feasibility of using an MTJ device as a microwave sensor for microwave imaging applications. An MTJ based sensor can detect microwave distributions which gives it the ability to non-destructively detect hidden objects. In addition, an MTJ device was also demonstrated to be adaptable to antenna design procedures. The work in this chapter has been published in Appl. Phys. Lett., 101, 232406 (2012) [46], Appl. Phys. A, 111, 329-337 (2013) [72] and Solid State

Communications, 198, 45-51 (2014) [47].

Chapter 4

Spintronic sensor based microwave holographic imaging

4.1 Introduction

In this chapter, by using microwave holographic reconstruction algorithms, we demonstrate the capability to identify hidden objects using a spintronic sensor. To achieve this goal, measurements of both the microwave phase and amplitude were required. In addition, a reconstruction algorithm was used to interpret the recorded microwave signal and translate it into readable images. Microwave holography is one of the most important imaging techniques in modern digital computer image reconstruction and was first proposed by Farhat in the 1970s [77]. Microwave holography has rapidly developed in the 21st century due to a reasonable data acquisition time, that is determined by a sampling space corresponding to the operation wavelength of the order of centimetre [77; 78; 79; 80; 81; 70; 82; 83]. This technique reconstructs a

target's reflectivity as a function of position. Microwave holography has been widely used for concealed weapon detection, non-destructive testing, and structural monitoring. In these applications, further improvements to the reconstruction algorithm have been made, including accounting for amplitude decay [84] and using transmitted signals [82]. The microwave holographic technique has also been applied to tissue imaging for medical purposes in recent years [85; 86; 84; 82; 83]. Both the microwave's amplitude and phase information are required in a microwave holography reconstruction algorithm. Due to the fact that microwaves have a large coherent length, the role of the microwave phase must be carefully considered in order to properly reconstruct the target.

Microwave holography is not the only imaging technique that requires phase information. Microwave radar and tomography also require information about the microwave phase. In order to make microwave sensors practical for imaging, a sensor based microwave phase detection technique is required.

In this chapter, a microwave sensor based rapid phase detection technique is developed. Combining the rapid phase detection technique and the microwave holography technique, a spintronic microwave imaging system is developed. Using the combined technique, we demonstrate the feasibility of microwave holographic imaging applications using a spintronic microwave sensor.

4.2 Spintronic sensor based microwave rapid phase detection technique

The interference method is introduced to realize the microwave rapid phase detection technique [41; 87; 45]. An MTJ based spintronic sensor was employed as a microwave detector, as shown in Fig. 4.1. Microwaves from the generator (Agilent E8257D) were split into two parts. Each part of the signal went through a different path before being finally coupled at the spintronic sensor. The signal in path A passed through several coaxial cables and were emitted to free space by the horn antenna (ATM 90-440-6). The free space signal was detected by the spintronic sensor and is denoted as $e_T cos(\omega t + \Phi)$, where e_T is the microwave amplitude, ω is the microwave frequency, t is time and Φ is the microwave phase shift when travelling in path A and free space. To verify the accuracy of the phase measurement, a mechanically adjustable phase shifter (ATM P1607) was inserted into path A. By tuning the phase shifter, Φ can be continuously adjusted to within 2°. Meanwhile, a reference signal was introduced to the sensor via path B. This included an adjustable attenuator (Mini-Circuits K2-BW3+), a bias tee (Mini-Circuits ZX85-12G+), a voltage controlled phase shifter (Hittite HMC935LP5E), a spintronic sensor and several coaxial cables. The attenuator was employed to balance the signal strength from the two paths. The bias tee was used to separate RF and low frequency signals.

The key element in this setup is the voltage controlled phase shifter, which made it possible to simultaneously read both amplitude and phase. The delay of the voltage controlled phase shifter depended linearly upon the bias voltage. When biased with

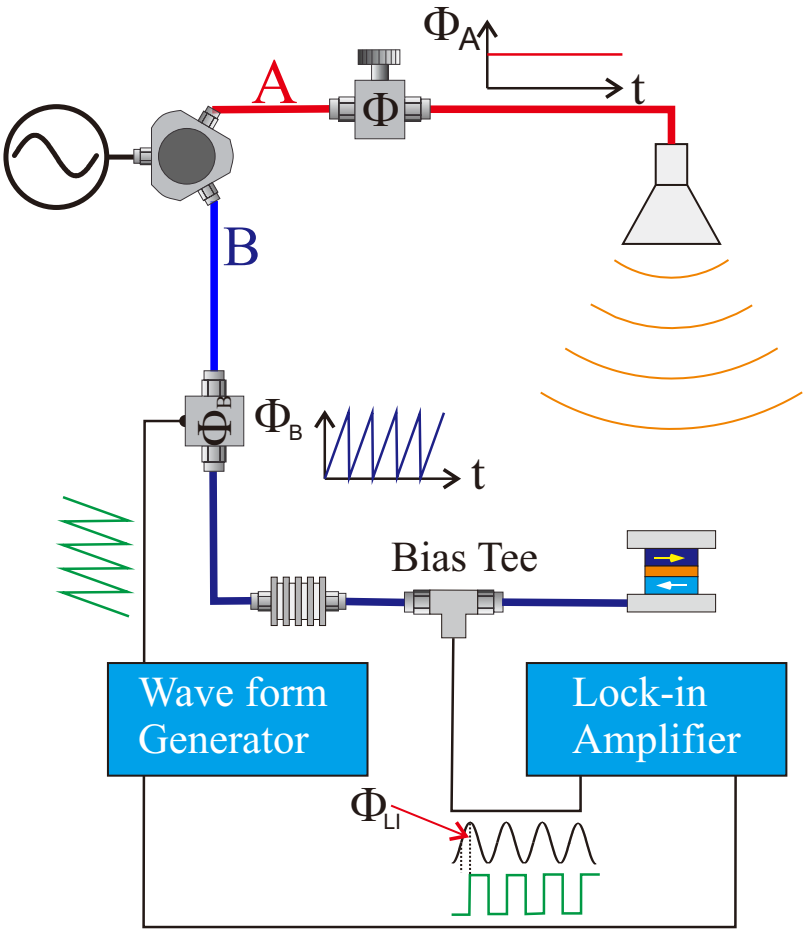

Figure 4.1: Interferometry experimental setup through which the microwave signal was coherently split into two beams and finally coupled at the sensor (MTJ). The use of a voltage controlled phase shifter inserted into path B permitted the detection of microwave magnitude and phase. After Yao et al. [45], used with permission.

a sawtooth wave, the voltage controlled phase shifter showed a sawtooth wave phase delay. The voltage range was set so that the phase delay varied from 0° to 360°. The microwave signal in path B is denoted as $e_R cos(\omega t + \Phi_t + \Phi_0)$, where e_R is the amplitude of the reference, Φ_0 is the phase difference between path A and path B. $\Phi_t = \omega_V t$ is the time dependent phase shift produced by the voltage-controlled phase shifter, where ω_V is the sawtooth wave frequency. The coupled microwave signal and

reference were recorded by the spintronic sensor and is written as

$$V(t) \propto e_T \cos(\omega t + \Phi) \cdot e_R \cos(\omega t + \omega_V t + \Phi_0)$$
$$= [e_T e_R \cos(2\omega t + \omega_V t + \Phi + \Phi_0) + e_T e_R \cos(\omega_V t + \Phi_0 - \Phi)]/2. \quad (4.1)$$

We can see that two terms are included in Eq. 4.1. One is the second harmonic microwave signal with a frequency of 2ω. The other is the low frequency term in the form of $e_T e_R cos(\omega_V t + \Phi_0 - \Phi)$. The second term is a *cos* oscillation voltage with frequency ω_V and initial phase $\Phi_0 - \Phi$. The amplitude is proportional to the microwave field intensity in free space and the phase is microwave phase shift during travel in free space. When triggered by an SR830 DSP (digital signal processing) lock-in amplifier, both the amplitude and the initial phase of this low frequency oscillation voltage were detected. This yielded the signal's amplitude and phase.

4.2.1 Frequency dependent phase delay

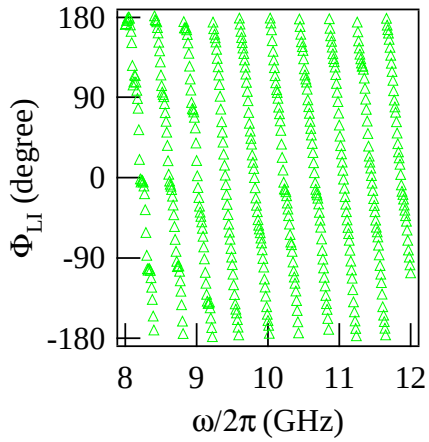

Figure 4.2: Fixing the mechanical phase shifter to zero, the measured lock-in phase Φ_{LI} plotted as a function of microwave frequency ranging from 8 to 12 GHz.

Fixing the MTJ and the antenna's position, the lock-in phase as a function of microwave frequency was measured. In the experiment, the mechanical phase shifter in path A was set to zero. The sawtooth frequency (triggered frequency) is set to 8.33 kHz. Microwaves ranging from 8 GHz to 12 GHz at an interval of 0.01 GHz were investigated. At each frequency, the lock-in phase was recorded by the lock-in amplifier using LabVIEW. The measured lock-in phase Φ_{LI} as a function of microwave frequency is plotted in Fig. 4.2, in which Φ_{LI} exhibits a periodic linear dependence with microwave frequency. This behavior is as expected, since the phase delay should be $\Delta\Phi = (d \cdot f/\nu) \times 360°$, where d is the microwave travel distance difference between path A and path B, and f and ν are the microwave frequency and velocity, respectively.

4.2.2 Phase measurement accuracy

To verify that the measured phase Φ_{LI} is exactly the microwave travelling phase delay in path A, a second experiment was performed to investigate the relationship between Φ_{LI} and the mechanical phase shifter Φ.

As in the first experiment, microwave frequencies ranging from 8 to 12 GHz were employed. In the experiment, at each frequency, Φ_{LI} was recorded when the phase value Φ of the mechanical phase shifter in path A was tuned. In a range of 180°, Φ_{LI} was recorded at more than 40 microwave frequencies to 30 individual Φ values. Φ_{LI} as a function of Φ is shown in Fig. 4.3. For simplification, all measured phase are offset to $-180°$ when $\Phi = 0$. It is found that Φ_{LI} exactly follows the relation of $\Phi_{LI} = \Phi + 180°$ for all the microwave frequencies under investigation. The result

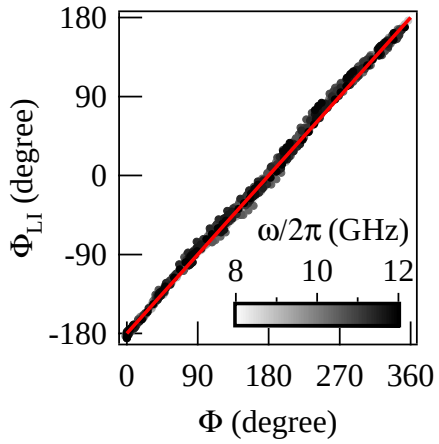

Figure 4.3: Φ_{LI} as a function of Φ for all frequencies ranging from 8 GHz to 12 GHz with a step size of 0.1 GHz. The solid line is the relation $\Phi_{LI} = \Phi - 180°$. After Yao et al. [45], used with permission.

demonstrates that the lock-in amplifier can indeed directly measure the microwave phase, confirming the predictions of Eq. 4.1.

4.2.3 Microwave power dependence measurement

In Fig. 4.2, the phase Φ_{LI} is shown to be independent of microwave power. In the third experiment, a detailed power variance study of V_{LI} and Φ_{LI} for frequencies of $\omega/2\pi$=10, 10.5 and 11 GHz was performed. At each frequency, Microwave power ranging from 0.1 mW to 100 mW were radiated to the MTJ sensor. At each microwave power, the lock-in voltage and phase were recorded by the lock-in amplifier.

The lock-in voltage V_{LI} as a function of microwave power is plotted in Fig. 4.4, where black squares, red circles and blue triangles represent $\omega/2\pi$=10, 10.5 and 11 GHz, respectively. The black solid lines are for $V_{LI} \propto P^{0.96}$ relationships. We can see that the measured lock-in voltages V_{LI} follow these lines, and this $V_{LI} \propto P^{0.96}$ result is in agreement with the expected relationship of $V_{LI} \propto e_T e_R \propto P$. It should

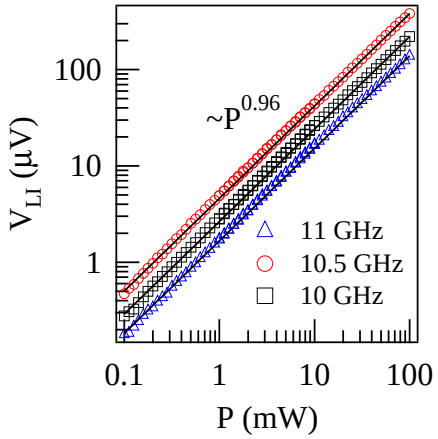

Figure 4.4: The lock-in magnitude V_{LI} (symbols) follows a $P^{0.96}$ relation (solid lines) at P=10 (circle), 15 (square), and 20 (triangle) dBm, where P is microwave power. After Yao et al. [45], used with permission.

be noticed that in this experiment, both e_T and e_R vary linearly with respect to the square root of the output microwave power. In practical uses, e_R is typically kept constant and therefore the measured voltage is proportional to the microwave electric field.

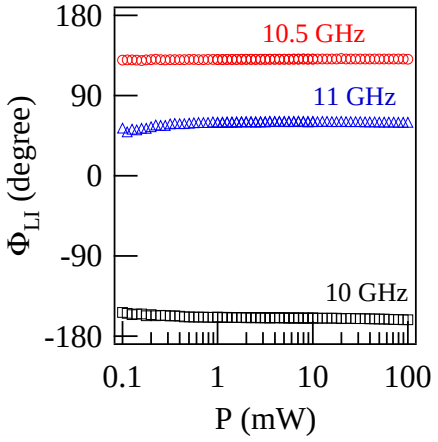

Figure 4.5: The lock-in phase Φ_{LI} as a function of microwave power. Φ_{LI} is not sensitive to the microwave power.

The lock-in phase Φ_{LI} as a function of microwave power is plotted in Fig. 4.5.

In contrast to V_{LI}, Φ_{LI} is constant with respect to the microwave power P. At each frequency, the fluctuation of Φ_{LI} is less than 1°. A more careful study of the phase fluctuation is plotted in Fig. 4.6. At a frequency of 11 GHz, the lock-in phase Φ_{LI} kept constant when V_{LI} is larger than 1 μV. The deviation of Φ_{LI} appeared when $V_{LI} < 1$ μV as indicated by Fig. 4.6. In this case, the background noise became an issue and the error can be as high as 10°.

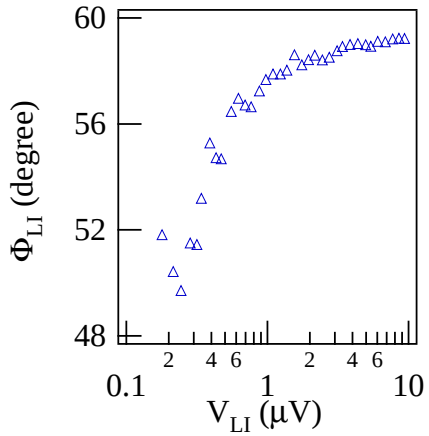

Figure 4.6: The lock-in phase Φ_{LI} as a function of rectification voltage at a frequency of 11 GHz. Deviation of Φ_{LI} appears when $V_{LI} < 1$ μV.

By employing this technique, the signal amplitude and phase may be measured simultaneously via a lock-in amplifier. Using this technique, the microwave sensor becomes a vector measurement tool. This greatly broadens the sensor's applications to areas such as imaging and non-destructive detection.

4.3 Spintronic sensor-based microwave holography system

In this section, we present a detailed discussion about the spintronic sensor based microwave holographic system, which includes the reconstruction algorithm, experimental setup and obtained images.

4.3.1 Microwave holography reconstruction algorithm

The basic microwave holographic configuration is shown in Fig. 4.7. A point transmitter and a point receiver are placed in a scanning plane. The point transmitter emits microwaves into free space and the point receiver records both the amplitude and phase reflected by the target.

In the experiment, both the transmitter and the receiver were scanned mechanically over a 2D rectangular aperture. During the scan process, the relative distance between the transmitter and receiver remained constant. We note that the transmitter and receiver are at $(x', y', 0)$ and $(x' - d, y', 0)$, respectively. Here, our coordinate system was chosen so that both the transmitter and receiver shared the same y' coordinate and z' is set to zero. In holography experiments, the target is described by its reflectivity function $f(x, y, h)$, which is the ratio between the reflected microwave intensity and the incident microwave intensity. Each point on the target can be regarded as a source emitting microwaves based on Huygens Fresnel principle [77]. These microwaves were recorded by the microwave receiver and can be written as an integration of the microwave field reflected from each point of the target multiplied

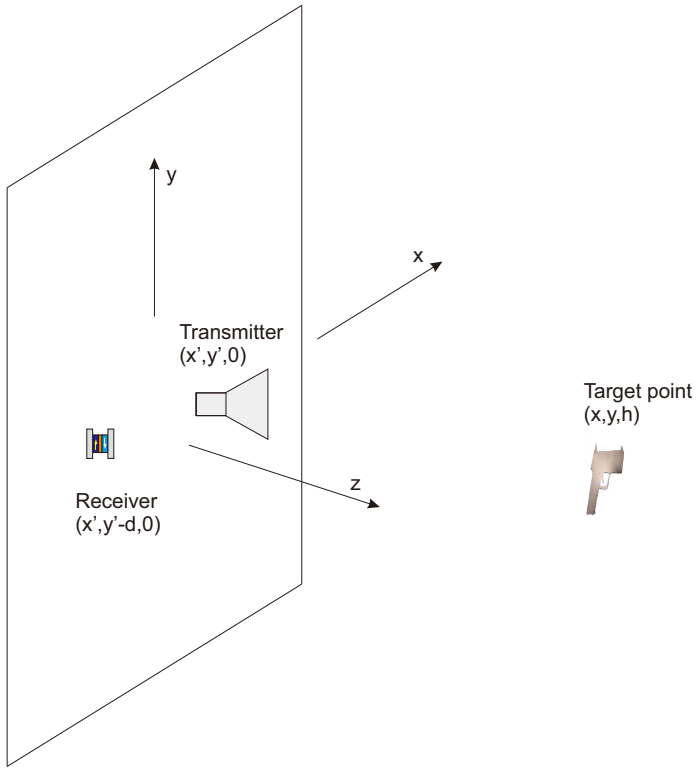

Figure 4.7: Microwave holography imaging configuration. The Transmitter $(x', y', 0)$ and the receiver $(x' - d, y', 0)$ are scanned together over a 2D rectangular aperture along x and y direction. The 2D target is located in the x-y plane with $z = h$.

by the travelling phase to the receiver. That is

$$s(x', y') = \int\int f(x, y) \frac{e^{-jk(R_1+R_2)}}{R_1 + R_2} dxdy, \tag{4.2}$$

where $s(x', y')$ is the recorded microwave signal, $k = 2\pi/\lambda$ is the wave number, λ is the microwave wavelength, $R_1 = \sqrt{(x' - x)^2 + (y' - y)^2 + h^2}$ and $R_2 = \sqrt{(x' - x + d)^2 + (y' - y)^2 + h^2}$ are the distances from the transmitter to the target and from the target to the receiver, respectively. $1/(R_1 + R_2)$ is the microwave amplitude decay when the microwave travels in free space. Here the integration is only performed along the x and y directions. This is based on the fact that the system discussed here is a two dimensional imaging

system and all targets are two dimensional with a fixed z coordinate, which is equal to h in this case.

In the following discussion, we will concentrate on retrieving $f(x, y)$ from Eq. 4.2. For simplicity, we define a function $g(x, y)$ as

$$g(x,y) = \frac{e^{-jk(\sqrt{x^2+y^2+h^2}+\sqrt{(x+d)^2+y^2+h^2})}}{\sqrt{x^2+y^2+h^2}+\sqrt{(x+d)^2+y^2+h^2}}. \tag{4.3}$$

Then Eq. 4.2 can be simplified as

$$s(x',y') = \int\int f(x,y)g(x'-x,y'-y)dxdy, \tag{4.4}$$

In Eq. 4.4, we can see that $s(x, y)$ is just the convolution of $f(x, y)$ and $g(x, y)$ in the x and y direction, which can be written as

$$s(x,y) = f(x,y) \star g(x,y), \tag{4.5}$$

where $\star$ is denoted as the two-dimensional convolution operator. Applying the Fourier transformation (FT) to both sides of Eq. 4.5, we obtain

$$S(k_x,k_y) = F(k_x,k_y)G(k_x,k_y), \tag{4.6}$$

where $S(k_x, k_y)$, $F(k_x, k_y)$ and $G(k_x, k_y)$ are the 2D FTs of $s(x, y)$, $f(x, y)$ and $g(x, y)$, respectively. k_x and k_y are the Fourier transform variables corresponding to x and y, respectively. Resolving $F(k_x, k_y)$ from Eq. 4.6 and transferring back to $f(x, y)$, we get

$$f(x,y) = FT_{2D}^{-1}\{\frac{S(k_x,k_y)}{G(k_x,k_y)}\} = FT_{2D}^{-1}\{\frac{FT_{2D}[s(x,y)]}{FT_{2D}[g(x,y)]}\} \tag{4.7}$$

In Eq. 4.7, $f(x, y)$ is resolved from the recorded microwave signal $s(x, y)$ and a defined function $g(x, y)$, in which the target's depth is known.

In this reconstruction algorithm, $s(x, y)$ is a complex function whose phase is a crucial element when performing Fourier Transform.

4.3.2 Spintronic sensor based microwave holography experimental setup

A schematic diagram of the spintronic sensor based microwave holographic imaging system is shown in Fig. 4.8. The apparatus includes an open-ended waveguide, a spintronic sensor, a microwave generator, a microwave power divider, a voltage-controlled phase shifter, an adjustable attenuator, a waveform generator, a lock-in amplifier and an x-y stepper motor. A Ku-band(12 GHz-18 GHz) open-ended rectangular waveguide was employed as the transmitting antenna. This open-end waveguide was chosen to act as a point source with high transmission efficiency. The spintronic sensor was placed at the same height as the open end of the waveguide and acted as the microwave receiver. The distance between the sensor and the waveguide is d. The microwaves emitted from the open-ended waveguide was reflected by the target and measured by the spintronic sensor. The spintronic sensor measured both the microwave's amplitude and phase and the data was recorded by the lock-in amplifier. An $x - y$ stepper motor was employed to move targets for scanning. The motor has a minimum spatial resolution of 12.5 μm and a maximum speed of 4 cm/s. This system is controlled by a computer using LabVIEW. Typically, a square scan area was performed (30 $\times$ 30 cm with a step of 2.5 mm). In the scan process, at each position,

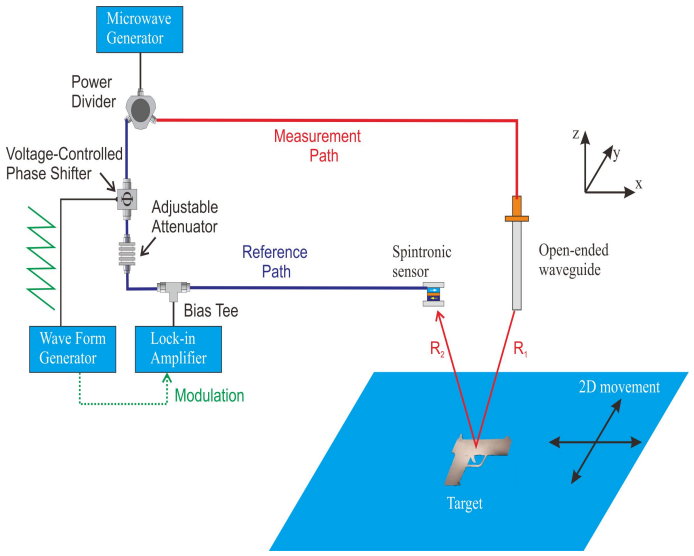

Figure 4.8: Schematic diagram of the spintronic sensor based microwave holographic imaging setup. The targets move along the x and y directions. During this process, the reflected microwave's amplitude and phase are recorded by the spintronic sensor. After Fu et al. [48], used with permission.

both the position information (x and y) and the microwave signal (amplitude and phase) were recorded by the computer. The data was analysed using Matlab-based on the algorithm described in section 4.3.1. The reconstructed images are represented using Igor Pro.

4.3.3 Penetration experiment

In our first experiment, a metallic gun-shape target cut from a 2 mm thick metallic plate with a length of 19.5 cm and a width of 12.5 cm was examined. A picture of the target is shown in Fig. 4.9. The target was placed at a depth (the vertical distance between sensor and target) of $h = 19$ cm and covered by a piece of cloth so that it is optically invisible. A picture of the experiment configuration is shown in Fig. 4.10. In the experiment, microwave frequency was set to 13.5 GHz and the microwave

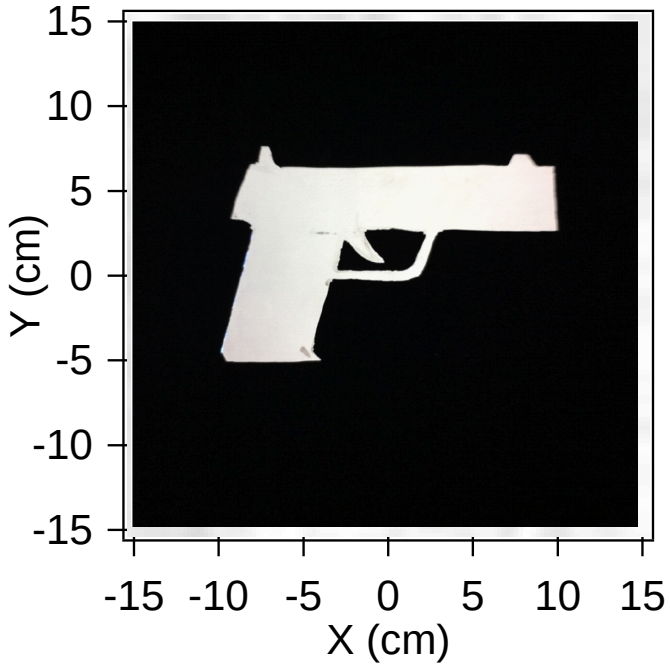

Figure 4.9: Photograph of the metallic (Al) gun-shape target with a length of 19.5 cm and a width of 12.5 cm. After Fu et al. [48], used with permission.

source power was 23 dBm. At this frequency, the sensitivity of the spintronic sensor was about 30 mV/mV. The target driven by the stepper motor moved along x and y directions with a step size of 2.5 mm in an aperture of 30 $\times$ 30 cm square. In this way, two dimensional patterns of microwave amplitude and phase were generated, plotted in Fig. 4.11(a) and (b), respectively. These patterns are significantly different from the optical image of the target as shown in Fig. 4.9.

In the optical image, one pixel only presents the information from a small area of the target. However, this is not the case for the patterns we got in Fig. 4.11. Each pixel in Fig. 4.11 collects information from all elementary points of the target. This is due to the fact that microwaves are coherently coupled together and there is no microwave lens to decouple information from each elementary point. To interpret the

Figure 4.10: The picture of the experiment setup. The gun-shaped target is placed on the x-y stage and covered by a piece of cloth.

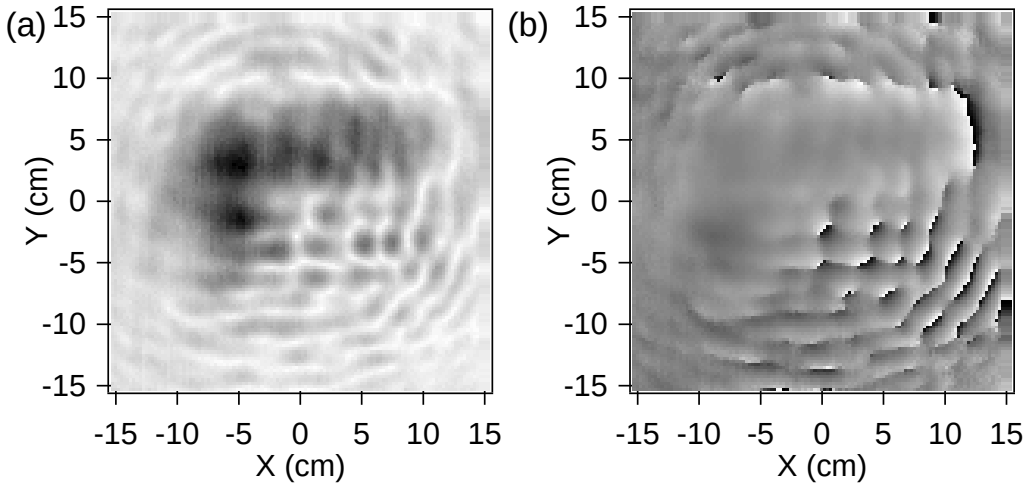

Figure 4.11: (a) Recorded holographic amplitude pattern of the gun-shaped target. (b) Recorded holographic phase pattern of the gun-shaped target. After Fu et al. [48], used with permission.

acquired data, holographic technology has been adapted, and is analogous to the lens in the optical range.

The reconstructed holographic image is obtained by applying the relation in Eq. 4.7 in section 4.3.1, as shown in Fig. 4.12. From the shape of the dark area in

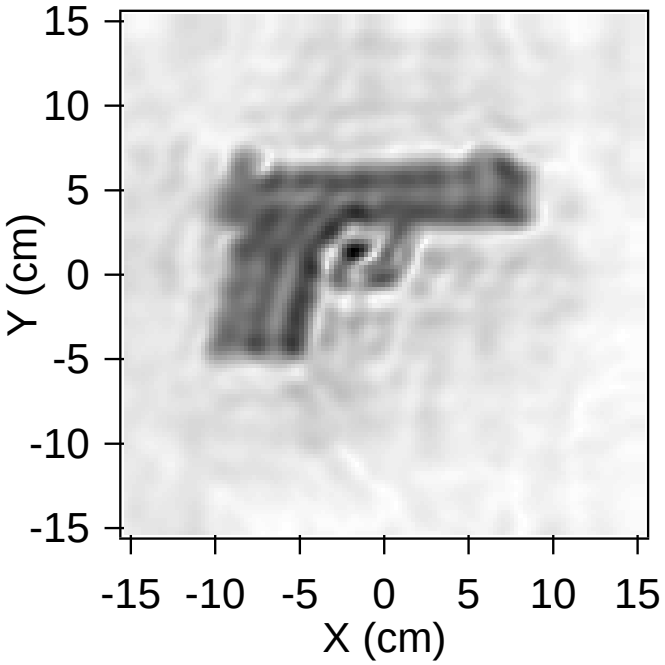

Figure 4.12: Reconstructed holographic image of the concealed target. After Fu et al. [48], used with permission.

Fig. 4.12, the hidden target is clearly observed and identified as a gun; even its trigger guard is distinguishable. Note that spintronic sensors are broadband, when the sensor works at other microwave frequencies, reconstruction images similar to Fig. 4.12 are obtained. With this experiment, we have demonstrated the potential to detect concealed weapons using the spintronic sensor based microwave holography system.

4.3.4 Resolving small objects

In this experiment, a series of Canadian coins are under investigation at the same height as the first experiment h=19 cm. A similar scan process was performed using the stepper motor. The only difference is that the scan aperture was 25 cm $\times$ 25

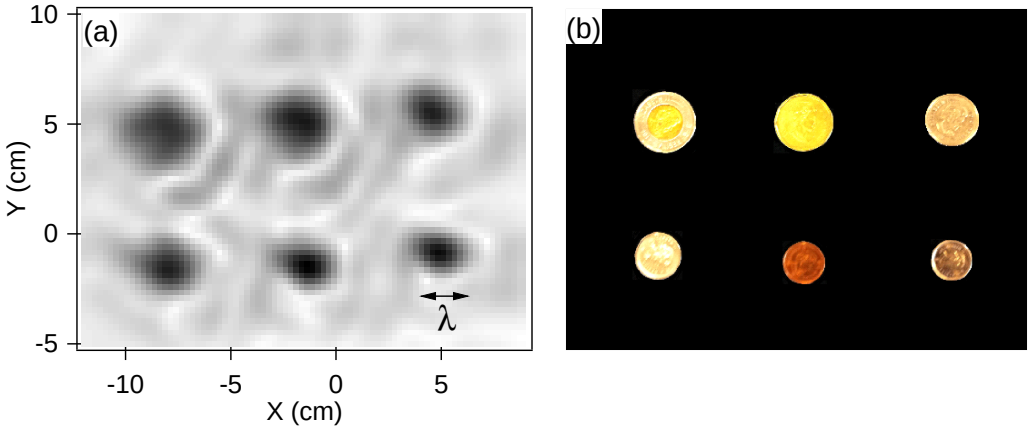

Figure 4.13: (a) Reconstructed image of different Canadian coins. The black arrow indicates the microwave wavelength used in the experiment. (b) Photograph of these Canadian coins in the same scale as that of (a). The coins are ordered by their sizes from upper left to bottom right. After Fu et al. [48], used with permission.

cm instead of 30 cm × 30 cm. Taking the recorded amplitude and phase into Eq. 4.7 in section 4.3.1, a reconstructed image of all the coins (21 cm × 15 cm shown) is obtained, as shown in Fig. 4.13(a). In Fig. 4.13(a), each dark area corresponds to a coin. Six coins are distinguished in the reconstructed image, which is in agreement with the experimental configuration shown in Fig. 4.13(b). The sizes of the coins are summarised in Tab. 4.1, where the coins are ordered by their sizes, corresponding to from upper left to bottom right in Fig. 4.13(b). In agreement with the coin sizes, the sizes of the dark areas also decrease. The smallest is the 10 cent coin with a diameter of 18 mm, which can be seen in the bottom right of Fig. 4.13(a). Note that the microwave wavelength λ=22 mm at 13.5 GHz.

We went a step further with an additional experiment to explore the system's resolving ability of small objects. A frequency of 12.1 GHz was chosen, and h ranged from 20 to 44 cm. In this experiment, the scan range was 40 cm × 40 cm and a series

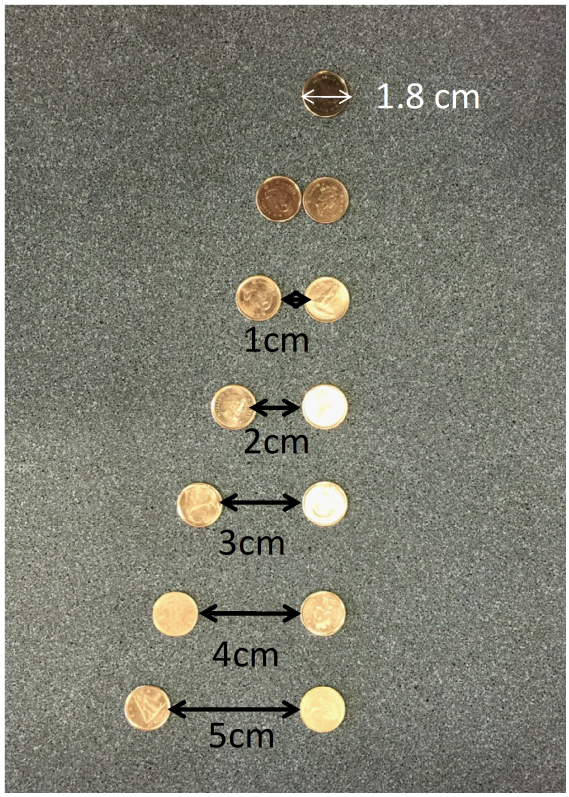

Figure 4.14: Photograph of objects: two column Canadian dimes. The lateral separation varies from 0 cm to 5 cm.

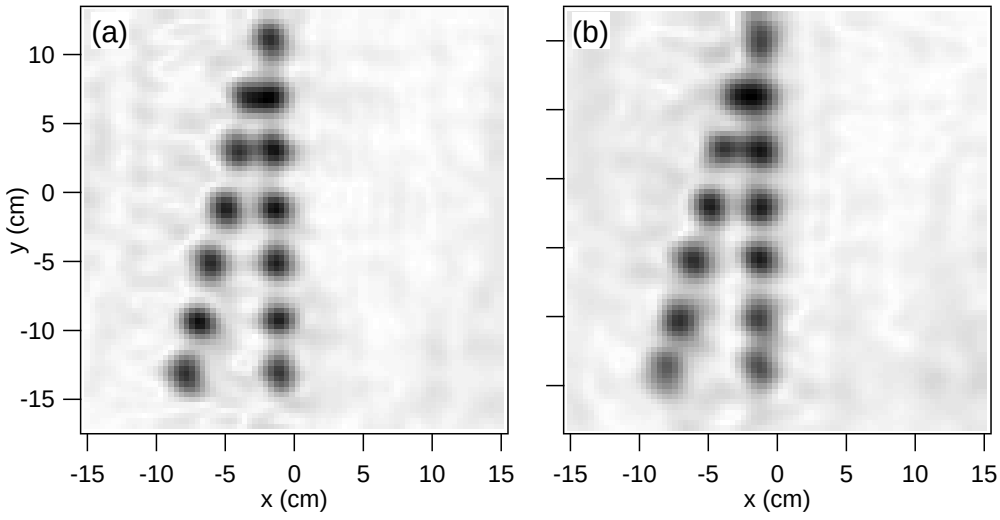

Figure 4.15: Reconstructed images of dimes when h=(a) 20 cm and (b) 32 cm

Coin (cent)	Diameter (mm)
Toonie (200)	28.00
Loonie (100)	26.50
Quarter (25)	23.88
Nickel (5)	21.20
Penny (1)	19.05
Dime (10)	18.03

Table 4.1: Diameters of Canadian coins

of dimes (10 cent coins) were examined. The diameter of these coins is 18 mm, which is smaller than the microwave wavelength of 24.8 mm. As shown in Fig. 4.14, the dimes were placed in a triangular shape. The lateral separation varied from 0 cm to 5 cm, as indicated by the black arrows in Fig. 4.14. Following the same scan process, a series of images were obtained at various h. The images when h=20 cm and 32 cm are shown in Fig. 4.15. In these images, the dimes can be clearly identified when the separation distance is large, such as the dimes in row 4 to row 7 starts from the top. In row 3, the dimes can still be distinguished in both images, indicating the system can resolving objects with a center to center distance of 28 mm (center to center distance of the dimes in row 3).

The amplitude in the reconstruction image for dimes in row 3 are plotted in Fig. 4.16, where offsets are shown for clarity. From Fig. 4.16, Two discrete peaks representing two dimes are clearly observed when h=20, 26 and 32 cm. As h increases, the two peaks begin to merge and cannot be distinguished, indicating a decrease in system resolution as h increases.

In far field experiments, the spatial resolution is limited by the diffraction limit, which is on the order of a half-wavelength multiplied by the system's optical number

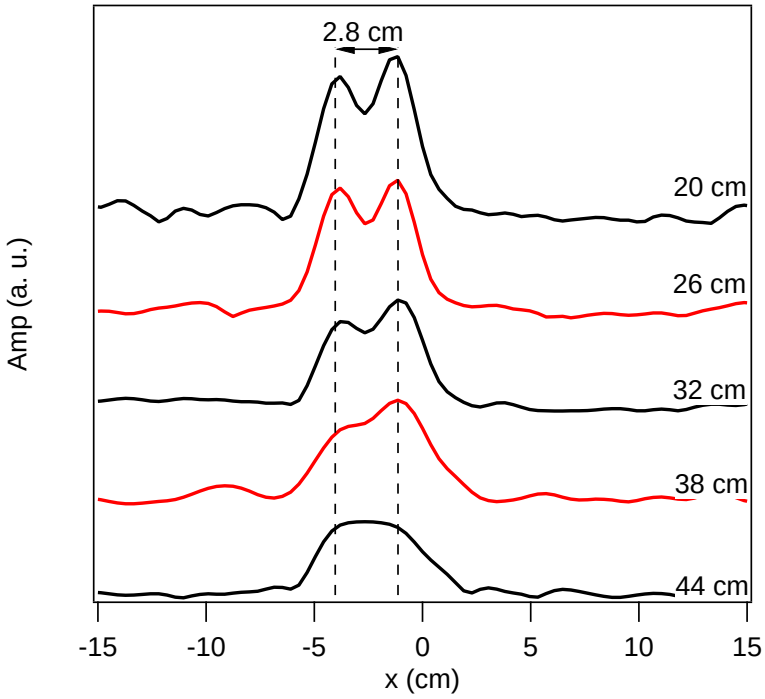

Figure 4.16: The amplitude of the deduced reflectivity for the two dimes separated by 1 cm (edge-to-edge distance) measured at different stand-off distances.

(focal length h divided by the scan aperture D)[78]. In our experiment, the system can resolve objects with dimensions about one wavelength, which can be further improved by increasing the scan aperture. However, the diffraction limit can not be overcome in the far field. In the near field, sub-wavelength resolution can be achieved and a smaller sensor is preferred for resolution issues, since the microwave field is less disturbed by smaller sensors. The size of the MTJ microwave sensor is much smaller than the wavelength of the microwave used. Even after taking into account the size of the electrode (0.2 mm), the cross section of the sensor is much smaller than the wavelength of the microwave used, allowing a precise detection of the phase.

4.3.5 Potential three-dimensional imaging

Three dimensional imaging systems can provide additional depth information due to which they are more powerful than the two dimensional ones. This system is two-dimensional, since the target depth must already be known for a single frequency measurement. However, the system could be potentially used as a 3D imaging system by tuning the value of h in the reconstruction code and comparing the sharpness of the obtained images. As a simple example, two targets placed at different depths were imaged by the holography system, as shown in Fig. 4.17. The gun-shaped target was placed at a depth of 19 cm while the F-shaped target was placed at a depth of 14 cm. The microwave frequency used was 13.5 GHz. The amplitude and phase patterns were obtained using the same measurement procedure. The sensor scanned in an area of 30 cm $\times$ 30 cm with steps of 2.5 mm. At each scan position, the amplitude and phase signal were recorded.

Using the reconstruction algorithm in section 4.3.1 and tuning h over a large scale, a series of reconstruction images are obtained, as shown in Fig. 4.18. In each figure, the h value used into Eq. 4.3 is indicated at the upper right corner of the figure. When the input h value is matched with the target's depth, the target is focused and has sharp edges in the image. Otherwise, the target is defocused and indistinct. As shown in Fig. 4.18(a) and (b), when the input h value is far from both targets' depths, neither the gun nor the "F" can be identified in the image. When the input h is matched with the gun's depth, the gun can be clearly observed and identified, while the "F" is still out of focus, as shown in Fig. 4.18(c) and (d). Similarly, when h is matched with the depth of the "F", "F" becomes clear while the gun is defocused,

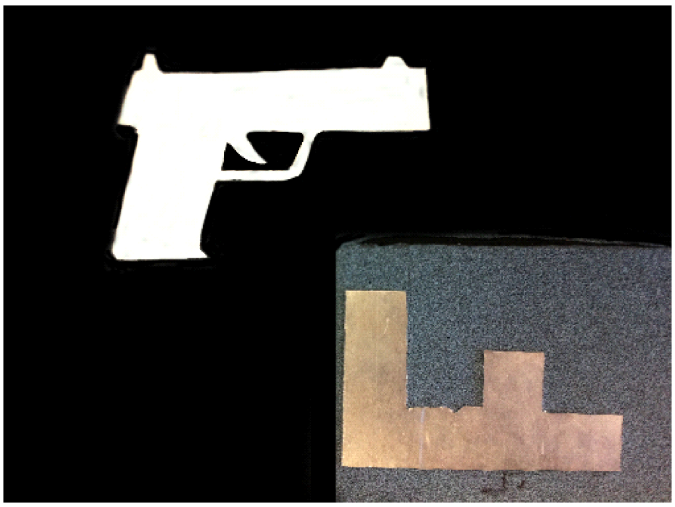

Figure 4.17: Photograph of the targets at different depths. The gun-shaped target is placed at a depth of 19 cm and the F-shape cut is placed at a depth of 14 cm. After Fu et al. [48], used with permission.

as shown in Fig. 4.18(g) and (h). By comparing the target's sharpness at different values of h, we may identify that the gun is placed at h = 18 to 19 cm and the "F" is placed at h = 13 to 14 cm. Therefore, the spintronic sensor based imaging technique has clearly demonstrated the capability of detecting not only the existence of the concealed objects but also their shapes. This capability might allow a concealed threat to be distinguished along with other hidden objects.

The point-by-point measurement shown in this section takes about 20 minutes to acquire a 2D image. However, the time is not limited by the sensor, but by the scan stage and communication between instruments. The experiment time can be reduced to 4-5 minutes by optimizing the scan process. In the optimized scan process, the x-y stage moves with a constant speed without stopping and the lock-in amplifier records the data simultaneously. It is believed that by using a faster stage or sensor array, the experiment could be finished within 1 minute.

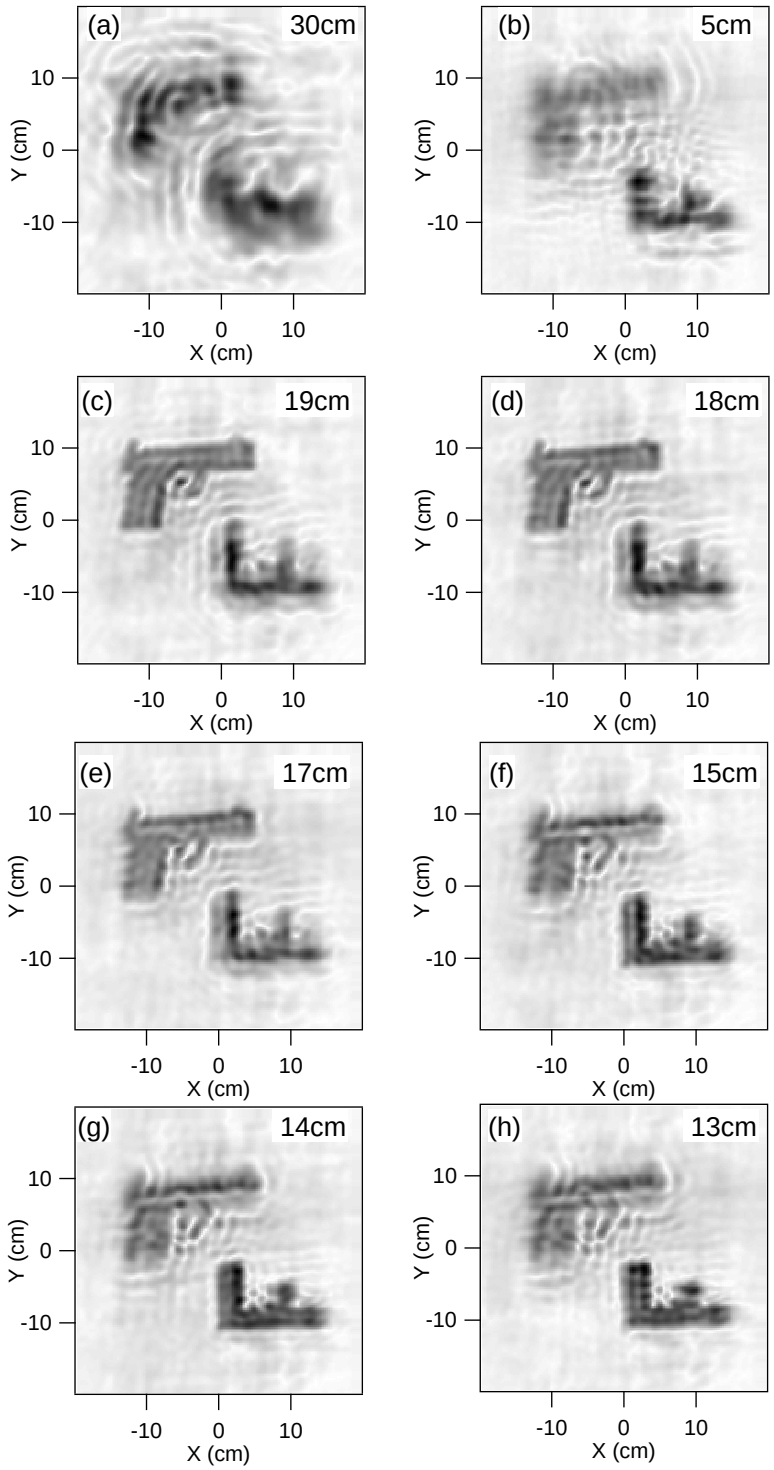

Figure 4.18: Reconstructed images focused at depths of (a) 30, (b) 5, (c) 19, (d)18, (e) 17, (f) 15, (g) 14 and (h) 13 cm.

In summary, a spintronic sensor based microwave holographic system was developed. Using this system, we explored the feasibility of microwave holographic imaging applications using a spintronic sensor. This system can detect targets embedded in microwave penetrable media and has the ability to resolve objects at dimensions of one microwave wavelength. The target's distance can be determined by a broadband measurement and this was confirmed by its sharpness in the reconstruction images. This implies that a three-dimensional imaging is achievable using a spintronic device.

4.4 Summary

In this chapter, we have developed a rapid phase detection technique which allowed a lock-in amplifier to simultaneously read both microwave amplitude and phase. Adapting the rapid phase detection technique, a sensor based microwave holographic imaging system was developed. The feasibility of microwave imaging using microwave sensors was demonstrated by detecting embedded objects. The work presented in this chapter has been published in Appl. Phys. Lett. 104, 062408 (2014) [45], J. Appl. Phys. 117, 213902 (2015) [48] and Proc. SPIE 9454, 945406 (2015) [88]. One U.S. patent describing the rapid phase detection technique is underway (United States Patent Pending, No.: WO 2015063596 A1, Date of Publication: May 7, 2015) [89].

Chapter 5

Microwave sensor based radar system

5.1 Introduction

In Chapter 4, we demonstrated the spintronic sensor's capability for identifying hidden objects by employing microwave holographic principles. Microwave holographic imaging is a single frequency measurement technique which does not make full use of the spintronic sensor's broadband property. In this chapter, we combine broadband microwave techniques and a wavefront reconstruction algorithm to explore the capabilities of the spintronic sensor in medical imaging applications, specifically in breast cancer imaging.

Breast cancer is a serious public health issue concerning women's health, and it is the most common form of cancer among Canadian women [90]. It is the second leading cause of death from cancer in Canadian women. In 2015, it is estimated that 25220

women were diagnosed with breast cancer. This represents 26 percent of cancers diagnosed in women in 2015. Unfortunately, approximately 5,000 women will die from breast cancer in 2015. This represents 14 percent of all deaths due to cancer in women in 2015. Based on 2007 estimates, about 1 in 9 Canadian women are expected to develop breast cancer in their lifetime and 1 in 29 will die from it. However, the 5-year relative survival rate can be as high as 88 percent when a tumor is found in an early stage. The current early stage detection method is X-ray mammography [91], which exposes patients to potentially harmful ionizing radiation. Other methods, such as magnetic resonance imaging (MRI) [91; 92; 93] and ultrasound [91; 94], are either too expensive or less effective. Microwave imaging could be a way to overcome these weaknesses due to the fact that microwaves are non-ionizing and microwave instruments are cost efficient, sensitive and compact [12; 85; 95; 71; 96; 97].

Microwave radar is one type of widely-used microwave imaging techniques. Microwave radar techniques have been successfully used in military, rescue and ground-penetrating applications [98; 99]. With microwave radar techniques, an object's position is determined by measuring the time delay of the reflected wave compared to the transmitted wave [98]. Microwave scattering occurs when there is a contrast in dielectric properties and microwave radar techniques can then create a map of the scattering locations[100; 101]. In microwave breast cancer imaging, strong reflections are related to tumors since tumors usually have dielectric properties that contrast strongly with the surrounding environment [102]. In this chapter, we explore the feasibility of a microwave breast cancer imaging system by using radar techniques with a sensor. Using this imaging system, an experiment was performed with a volunteer.

5.2 Microwave reconstruction algorithm in a circular scan geometry[100]

Consider a circular scan geometry in the x-y plane with a radius of R. Here q (r_q, θ_q) is a point in the target. The transmitter and the receiver are located at (R, ϕ) and (R, φ), respectively. The scan geometry can be found in Fig. 5.1. The signal received may be written as [100; 101]

$$s(t, \phi, \varphi) = \sum_{q=1}^{T} \sigma_q \cdot f\left(t - \frac{D(\phi) + D(\varphi)}{\nu}\right), \tag{5.1}$$

where T is the total number of the scattering points in the target, σ_q is the reflection coefficient of point q, ν is the microwave speed, $D(\phi) = \sqrt{R^2 + r_q^2 - 2 \cdot R \cdot r_q \cdot \cos(\phi - \theta_q)}$ and $D(\varphi) = \sqrt{R^2 + r_q^2 - 2 \cdot R \cdot r_q \cdot \cos(\varphi - \theta_q)}$ are the distances from the point q to the transmitter and the receiver, respectively. Taking the Fourier transform to transfer the signal from time domain to the frequency domain, we have

$$S(\omega, \phi, \varphi) = \sum_{q=1}^{T} \sigma_q F(\omega) \cdot \exp\left(-j(k \cdot (D_p(\phi) + D_p(\varphi)))\right) \tag{5.2}$$

where $F(\omega)$ is the spectrum of $f(t)$. Taking the Fourier transform with respect to ϕ and φ, we obtain

$$S(\omega, \alpha, \beta) = \sum_{q=1}^{T} \sigma_q \Gamma(\omega, \alpha, \beta) \cdot \exp\left(-j(\Psi_q(\alpha) + \Psi_q(\beta) + \Xi(\alpha) + \Xi(\beta))\right), \tag{5.3}$$

where

$$\Psi_q(\alpha) = \sqrt{k^2 + r_q^2 - \alpha^2} + \alpha \sin^{-1}(\alpha / k r_q) + \alpha \theta_q, \tag{5.4}$$

$$\Psi_q(\beta) = \sqrt{k^2 + r_q^2 - \beta^2} + \beta \sin^{-1}(\beta / k r_q) + \beta \theta_q, \tag{5.5}$$

$$\Xi(\alpha) = \sqrt{k^2 + R^2 - \alpha^2} + \alpha \sin^{-1}(\alpha / k R) + \alpha \pi, \tag{5.6}$$

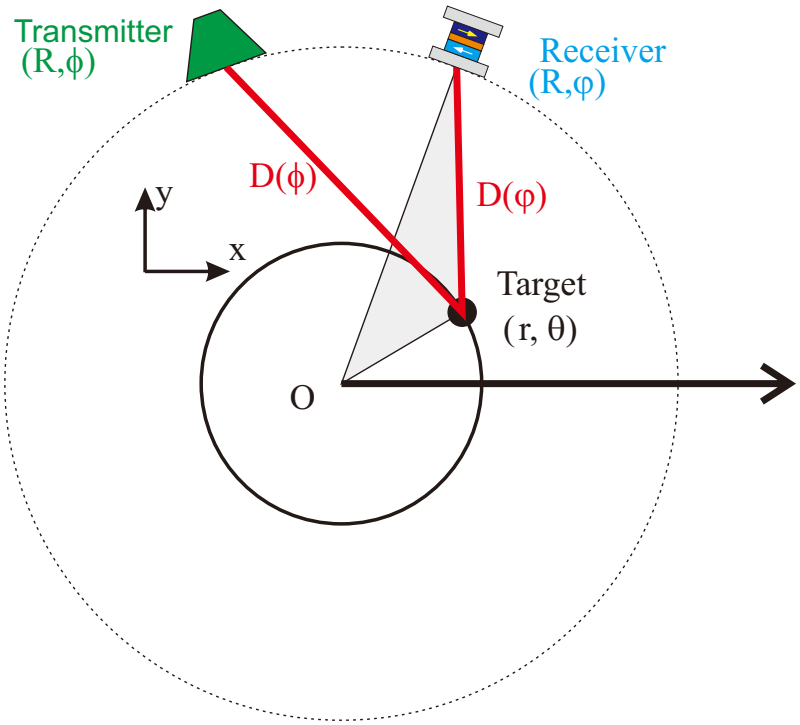

Figure 5.1: Multi-static scan geometry with transmitter at (R, ϕ), receiver at (R, φ) and target at(r, θ). After Fu et al. [49], used with permission.

$$\Xi(\beta) = \sqrt{k^2 + R^2 - \beta^2} + \beta \sin^{-1}(\beta/kR) + \beta\pi, \tag{5.7}$$

and $\Gamma(\omega, \alpha, \beta)$ represents the amplitude components of the signal in the (ω, α, β) space. α and β are the Fourier components of the angles ϕ and φ, respectively.

Note that $\Psi_q(\alpha)$ and $\Psi_q(\beta)$ are functions of r_q and θ_q which are related to the target. However $\Xi(\alpha)$ and $\Xi(\beta)$ are functions of R which are only related to the scan geometry. To eliminate the effect of scan geometry, a filter is employed

$$\Lambda(\omega, \alpha, \beta) = \exp(j(\Xi(\alpha) + \Xi(\beta))). \tag{5.8}$$

The compensated spectral response is

$$S_c(\omega, \alpha, \beta) = S(\omega, \alpha, \beta) \cdot \Lambda(\omega, \alpha, \beta) = \sum_{q=1}^{T} \sigma_q \Gamma(\omega, \alpha, \beta) \cdot \exp\left(-j(\Psi_q(\alpha) + \Psi_q(\beta))\right). \tag{5.9}$$

$S_c(\omega, \alpha, \beta)$ is only related to the target. In the following steps, we will represent S_c in $x-y$ space, which is also the reconstruction mapping we need. Taking the inverse Fourier transform with respect to α and β, we have

$$S_c(\omega, \phi, \varphi) = \sum_{q=1}^{T} \sigma_q \Theta(\omega) \exp(-2jkr_q(\cos(\theta_q - (\phi+\varphi)/2) \cdot \cos((\varphi-\phi)/2))) \quad (5.10)$$

Note that during the scan process, the relative angle between the transmitter and the receiver stays constant, so we can eliminate the $\cos((\varphi-\phi)/2)$ term and get

$$S_f(\omega, \phi, \varphi) = S_c(\omega, \phi, \varphi)\sec((\varphi-\phi)/2) = \sum_{q=1}^{T} \sigma_q \Theta(\omega) \exp(-2jkr_q(\cos(\theta_q - (\phi+\varphi)/2))). \quad (5.11)$$

Simplify S_f by introducing $\rho = (\phi+\varphi)/2$, we have

$$S_f(\omega, \rho) = \sum_{q=1}^{T} \sigma_q \Theta(\omega) \exp(-2jkr_q(\cos(\theta_q - \rho))). \quad (5.12)$$

Since $S_f(\omega, \rho)$ is in polar coordinates, a coordinate transformation is required to process the mapping. The coordinate transformation is performed in k space, where $k_x = k \cdot \sin(\rho)$ and $k_y = k \cdot \cos(\rho)$. Then we can get the final form of the mapping.

5.3 Microwave sensor-based radar experiment performed in lab-based system

A spintronic sensor based radar imaging system is shown in Fig. 5.2. The system includes a microwave generator (Agilent E8257D), a power divider (ATM P215), a voltage-controlled phase shifter (Hittite HMC935LP5E), an adjustable attenuator (Mini-Circuits K2-BW3+), a bias tee (Mini-Circuits ZX85-12G+), a lock-in amplifier (Stanford Research Systems SR830), a wave form generator (Stanford Research

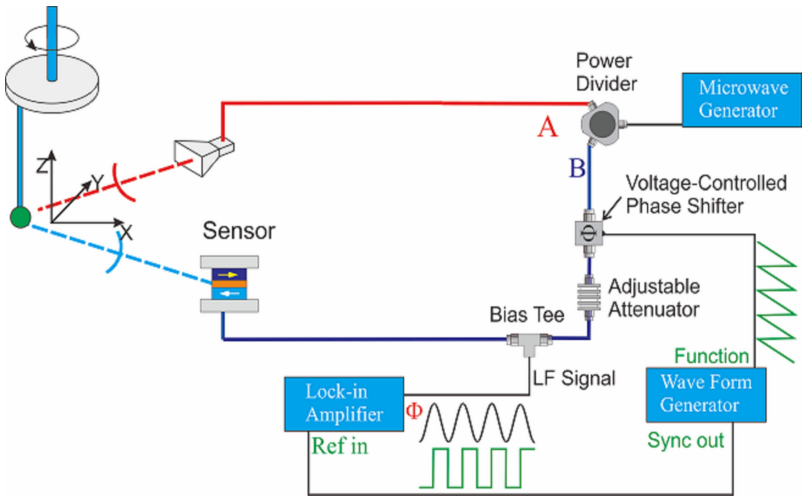

Figure 5.2: A schematic diagram of spintronic sensor based microwave radar system. The right side of the figure shows the instruments required for rapid phase detection which is discussed in detail in Chapter 4. The left side is the target attached to a rotation stage.

Systems DS345), a horn antenna (ATM 90-440-6), a spintronic sensor and a rotation stage (RMS IMC23-L01). The rotation stage was used to move the targets. All the other instruments were used for microwave amplitude and phase detection, as in Chapter 4.

In contrast to the 2D holography experiment, microwave radar employs broadband microwaves to determine the target's location. In the near field range, broadband microwave radar is widely used since high resolution can easily be achieved. Mathematically, a stepped frequency continuous wave (SFCW) can be converted into a pulsed wave in the time domain via a Fourier transform [98]. The time resolution is inversely proportional to the bandwidth of the SFCW. For example, for microwaves with 4 GHz bandwidth, the minimum time resolution is $\delta t = 0.25$ ns. With such a time resolution, the system can achieve a spatial resolution of $\delta d = c \cdot \delta t/2 = 3.75$ cm in air, where c is the propagation speed of microwaves, and the factor of $1/2$ comes

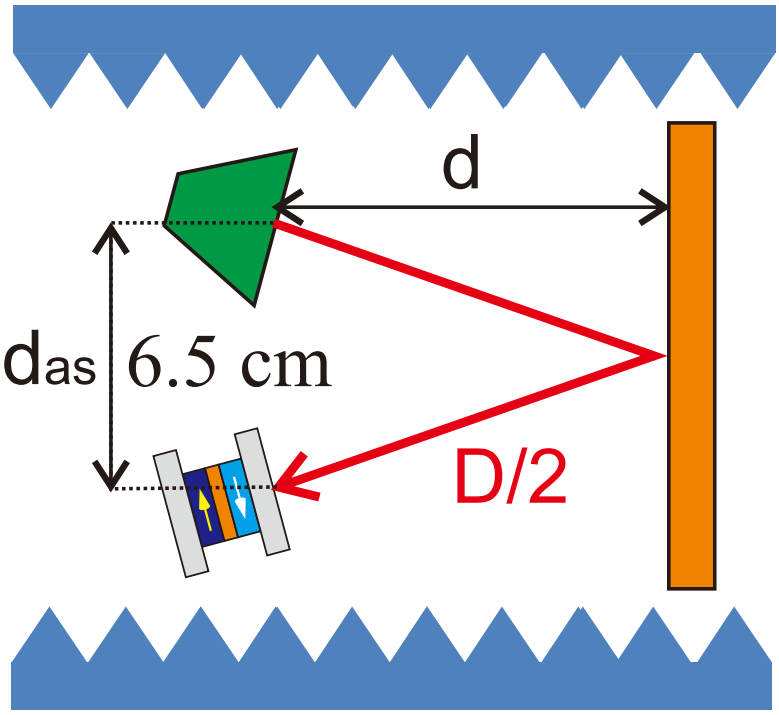

Figure 5.3: Schematic diagram of of the calibration measurement. A copper board was placed in front of the antenna and the sensor at a distance of d from both the antenna and the sensor.

from the microwave's round trip.

A calibration measurement was performed using a copper board, as shown in Fig. 5.3. The copper board was placed in front of the antenna and the sensor at a distance of d from both the antenna and the sensor. The antenna and the MTJ based sensor were separated by a distance d_{as} =6.5 cm. The microwave travelled from the antenna to the copper board and reflected back to the sensor. The total travelling distance is $D = 2\sqrt{d^2 + (d_{as}/2)^2}$. The microwave phase Φ follows the simple relation of $\Phi = D/\lambda = (D/c2\pi)\omega$ for a given system with a fixed microwave travelling distance D, where λ is the microwave wavelength. In the calibration experiment, microwaves

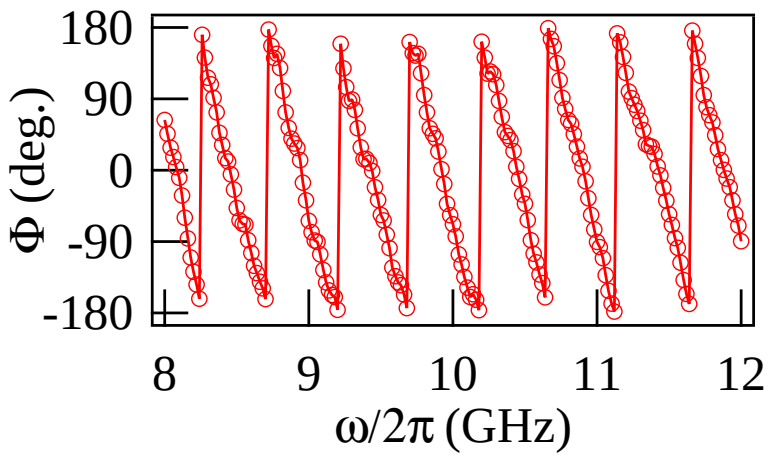

Figure 5.4: Measured microwave phase Φ as a function of microwave frequency between 8 and 12 GHz. Φ follows the simple relation of $\Phi = D/\lambda = (D/c2\pi)\omega$ and Φ is wrapped in a range between $\pm 180°$. After Fu et al. [49], used with permission.

ranging from 8 to 12 GHz with an interval of 0.02 GHz were employed. For a given distance d, the microwave amplitude and phase were recorded by the lock-in amplifier at each frequency. The measured phase is plotted as a function of frequency in Fig. 5.4, which is in good agreement with the expected relationship.

The inverse fast Fourier transform (iFFT) was used to transform the frequency domain to the time domain so that the time delay due to the reflection could be determined. Moving the target distance d from 4 cm to 14 cm in steps of 2 cm, a series of FFT spectra are obtained, as shown in Fig. 5.5. From Fig. 5.5, we can clearly see that the peaks of the FFT spectra shift with respect to d, as expected.

Picking the peak position of each FFT spectrum and plotting these as a function of D, a linear dependence is obtained, as shown in Fig. 5.6. Fitting a linear relation, a slope of $c = 3 \times 10^8$ m/s and $\Delta t_0 = 1.05 \pm 0.05$ ns at $D = 0$ is found. The error bar of $0.05ns$ comes from the linear fitting with a 90% confidence. The drift in Δt_0

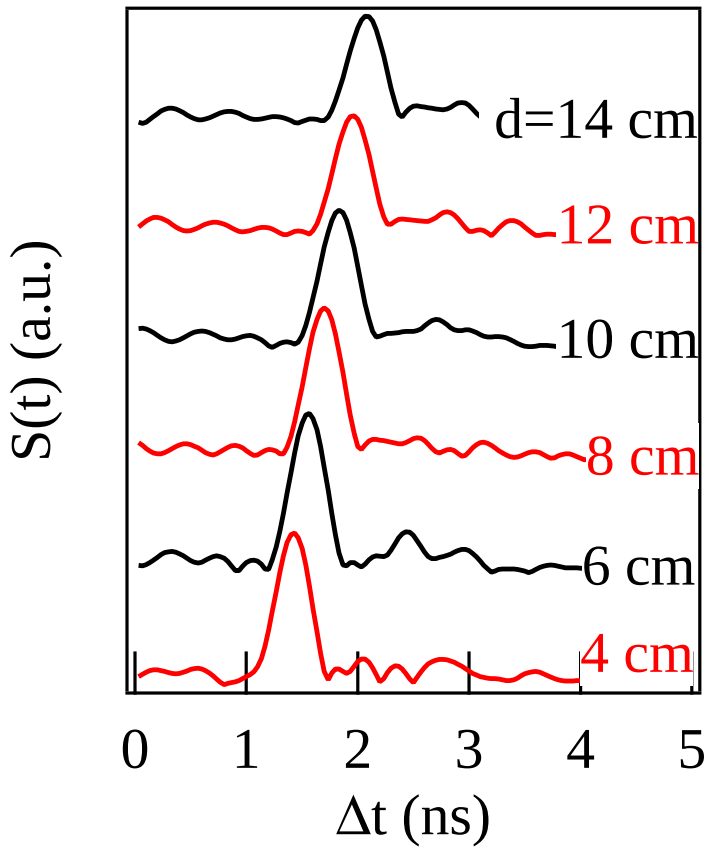

Figure 5.5: The iFFT spectrum when the target is moved from 4 cm to 14 cm. The shift of the peak clearly indicates the movement of the target. After Fu et al. [49], used with permission.

is of the order of 0.05 ns over days and is ignored as it is within the measurement uncertainty.

With our ability to detect the amplitude and phase of microwaves, the spintronic microwave sensor was used in microwave image experiments by using the traditional radar technique. The experimental configuration is shown in Fig. 5.1, where a circular scan geometry with a radius R is defined in the x-y plane. The origin of the coordinate system is at the center of the aperture $O(0, 0)$, the antenna is at (R, ϕ), the spintronic

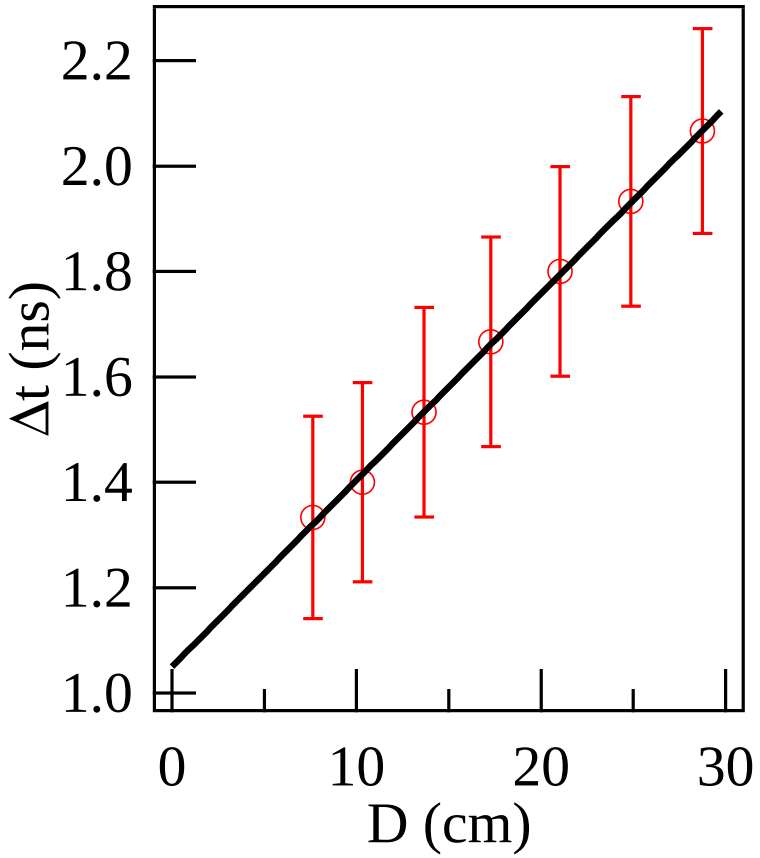

Figure 5.6: Δt as a function of distance $D = 2\sqrt{d^2 + (d_{as}/2)^2}$ obtained from iFFT spectra shown in Fig. 5.5. The line shows a linear dependence of $D = (\Delta t - \Delta t_0)c/2$ with $\Delta t_0 = 1.05 \pm 0.05$ ns. After Fu et al. [49], used with permission.

sensor is at (R, φ) and the target is at (r, θ). $D(\phi)$ and $D(\varphi)$ are the distances from the target to the antenna and the sensor. These can be expressed as $D(\phi) = \sqrt{R^2 + r^2 - 2R \cdot r\cos(\phi - \theta)}$ and $D(\varphi) = \sqrt{R^2 + r^2 - 2R \cdot r\cos(\varphi - \theta)}$. The radius of the transmitter and receiver as defined in Fig. 5.1 is R=18 cm. The angle between the horn antenna and the MTJ sensor is fixed at $\phi - \varphi = 20°$ and the initial position is at $\phi + \varphi = 0°$. The phase delay of $\omega[D(\phi) + D(\varphi)]/c$ enables the target position to be obtained from the phase measurement. For broadband measurements, the phase

differences between the frequencies lead to the formation of a phase modulated signal with the form

$$S(\omega, \phi, \varphi) = \sigma F(\omega) \exp\{-j\frac{\omega[D(\phi) + D(\varphi)]}{\nu}\}, \tag{5.13}$$

where σ is the reflectivity of the target, and $F(\omega)$ is the magnitude response from the target at frequency ω. The amplitude decay with distance is not considered since it has little impact on the image. The signal in Eq. 5.13 resembles the Fourier transform of a time delayed signal. By calculating the inverse Fourier transform of Eq. 5.13, the following signal is obtained: [100; 101]

$$S(t, \phi, \varphi) = \sigma f\left(t - \frac{D(\phi) + D(\varphi)}{\nu}\right) \tag{5.14}$$

where $f(t)$ is the time domain representation of $F(\omega)$. This time domain signal has a delay which is directly related to the signal travel time between the radiating antenna, the target and the receiving sensor.

Now we describe the first radar imaging experiment in the cylindrical scan geometry. The target was a polymer-distilled-water-mixture sphere with a 3 cm diameter, which had a dielectric constant of 33 and a conductivity of 1.6 S/m to simulate fibro glandular tissue [102]. As shown in Fig. 5.1, the target was located at (r, θ). The transmitter was an X-band (8-12 GHz) horn antenna, and the receiver was an MTJ sensor. The radiated microwave power was measured by a power meter (Agilent U2000)to be about 10 mW .

The data were recorded at different positions of (ϕ, φ). To simplify the implementation, we rotated the target counter-clockwise instead of rotating the transmitter

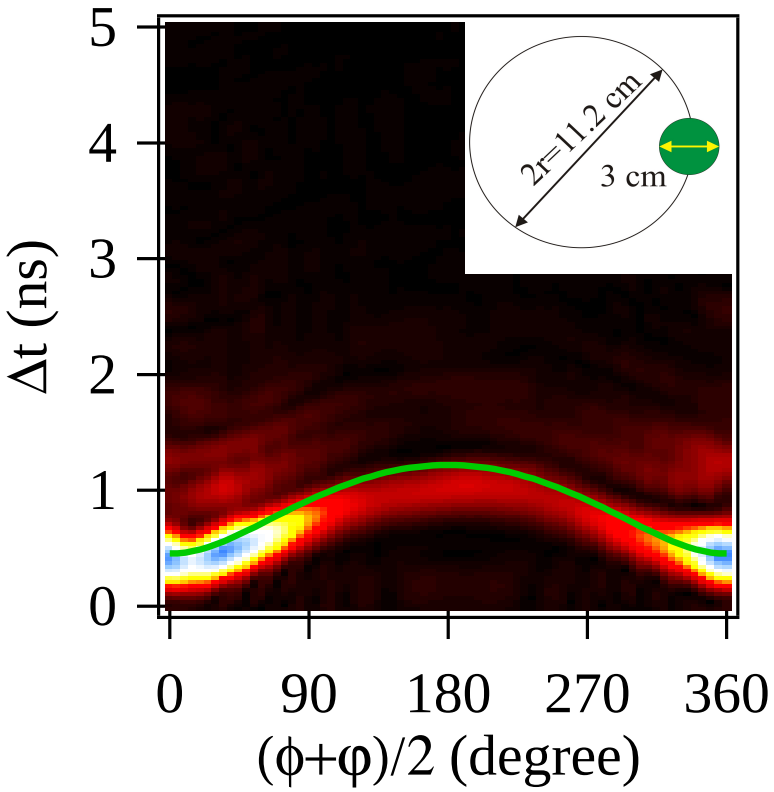

Figure 5.7: 2D mapping of iFFT amplitude as a function of response time and θ position. Green line indicates the calculated trajectory of the target without any fitting parameters. After Fu et al. [49], used with permission.

and receiver, which is mathematically equivalent to rotating the transmitter and the MTJ sensor clockwise. The data were collected along a circular scan geometry with 72 scan locations at intervals of 5°. At each location, the microwave frequency was scanned from 8 to 12 GHz at intervals of 0.02 GHz.

The iFFT spectra for each θ is mapped in Fig. 5.7, where the colors represent the amplitude of the spectra. In the figure, one can clearly see that the peak positions of the spectra shift with respect to the rotation angle $(\phi + \varphi)/2$, which indicates the time delay to the target. At $(\phi + \varphi)/2 = 5 \pm 5°$ where the target is close to the horn

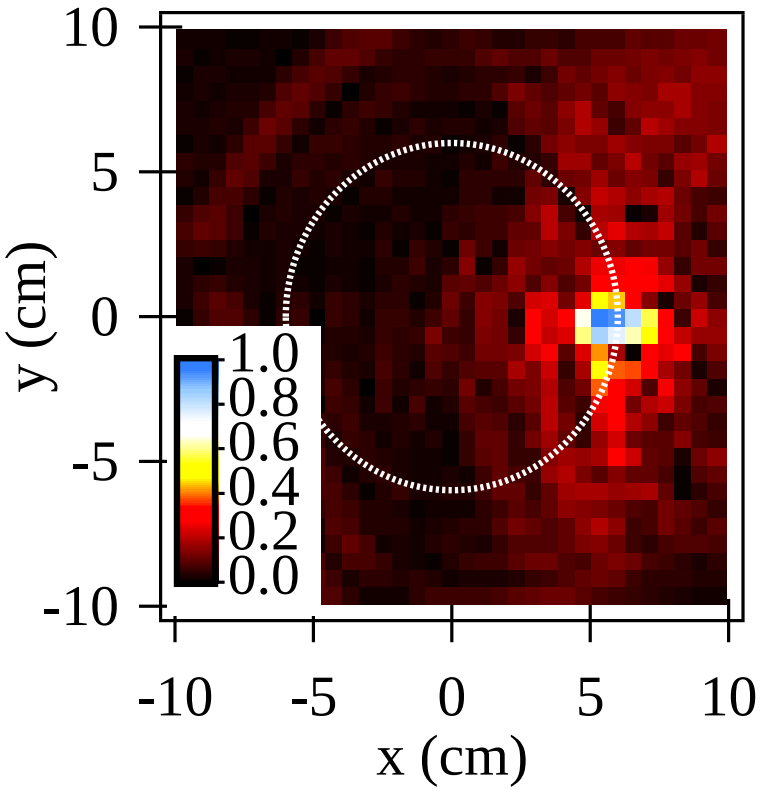

Figure 5.8: The distribution of the reflectivity in x-y plane forms a 2D image, where the bright spot indicates the initial position of the target and the dotted line indicates a radius of 5.6 cm. After Fu et al. [49], used with permission.

antenna and sensor, the signal is strongest and the time delay is about 0.35 ± 0.05 ns corresponding to a distance of $D(\phi) + D(\varphi) = 10.5 \pm 1.5$ cm. In the opposite position at $(\phi+\varphi)/2 = 185 \pm 5°$, the signal is weakest and time delay is about 1.01 ns corresponding to a distance of $D(\phi) + D(\varphi) = 30.3 \pm 1.5$ cm. These features indicate the initiation position of the target is at $r = 5.4 \pm 1.5$ cm and $\theta = 5 \pm 5°$, consistent with the experimental setup with $r = 5.6$ cm and θ=0. We can further calculate the trajectory of the target and the resultant time delay is plotted as a green line in Fig. 5.7.

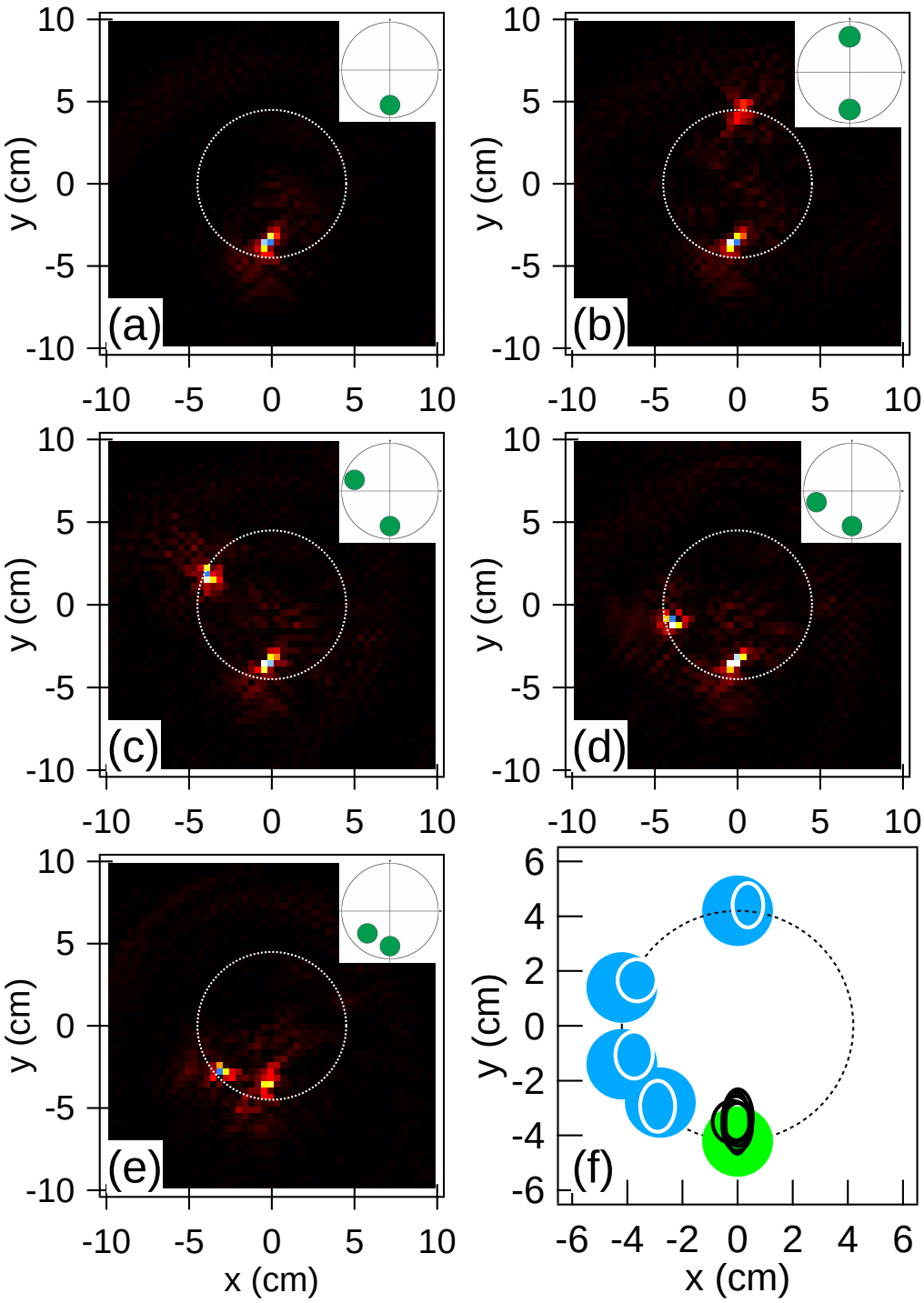

Figure 5.9: (a) A single target located at (0.0 cm, -4.2 cm) was used for calibrating the effective propagation speed ν_{eff}. Adding a second target at (b)(0.0 cm, 4.2 cm); (c) (-4.2 cm, 1.4 cm); (d) (-4.2 cm, -1.4 cm); and (e) (-2.8 cm, -2.8 cm). (f) Summary of the result of Fig. 5.9(a)-(e). The green solid ellipses (white empty ellipses) are positions of the experimental setup (reconstructed image) for the first and second target, respectively. After Fu et al. [49], used with permission.

For a single target, one can also deduce a reasonable location of the target by fitting the trajectory in the 2D iFFT spectra. The image reconstruction has advantages in identifying multiple targets of complex circumstances as we discuss below. The purpose of the image reconstruction is to plot the spatial distribution of the microwave scatter, and identify the position of the targets. Wavefront reconstruction can be applied to solve such a problem. Using a reconstruction of data acquired along circular trajectories, the reflection spectra measured in the spatial-temporal domain were transformed to the spatial domain to obtain the position of the target. The image reconstruction was used to convert the 2D iFFT spectra to a more readable image as shown in Fig. 5.8 by the spatial distribution of reflectivity. A strongly reflective target (5.4 cm,0.0 cm) is clearly seen in the x-y plane. The results without any fitting parameter are in agreement with expectation. The dotted line indicates a circle with a radius of 5.6 cm.

A second imaging experiment was performed under more complex conditions, where a 2.5 cm diameter sphere of a polymer-distilled-water-mixture was immersed in Canola-oil (with a dielectric constant of 2.5 and a conductivity of 0.035 S/m) in a cylindrical container with a radius of 6.5 cm, thus simulating the tissue in a human breast. As in the first experiment, 72 scan locations at intervals of 5° in a circular geometry were investigated. Microwave frequencies ranging from 7-13 GHz at intervals of 0.02 GHz were employed. This gave a time resolution of 0.08 ns. An effective propagation speed ν_{eff} was used to simplify the reconstruction process. In order to determine ν_{eff}, a single target experiment was performed for calibration. A $\nu_{eff} = 2.7 \times 10^8$ m/s was determined and the reconstructed image is shown in Fig.

5.9(a), where the target is located at (-0.4 cm, -3.9 cm), which is in agreement with the experimental setup (0.0 cm, -4.2 cm) with an error of 0.5 cm.

To verify the feasibility of the proposed approach in a more complex environment, a second target almost identical to the first one was added in the Canola-oil. As shown in the inset of Fig. 5.9(b), the second target was placed at (0.0 cm, 4.2 cm), while the first target was left at its original position (0.0 cm, -4.2 cm). The reconstructed image is shown in Fig. 5.9(b), indicating the second target is at (0.4 cm, 4.4 cm), which is in agreement with its location in the experimental setup. The first target was reconstructed at (-0.4 cm, -3.9 cm). This is similar to the experimental position, as shown in Fig. 5.9(a).

In the following experiments, the second target was moved to other positions (-4.2 cm, 1.4 cm), (-4.2 cm, -1.4 cm), and (-2.8 cm, -2.8 cm), as shown in the insets of Fig. 5.9(c), (d) and (e), respectively. From their corresponding reconstructed images in Fig. 5.9(c), (d) and (e), we summarized the results in Fig. 5.9(f), where the green solid ellipses and blue solid ellipses are positions of the experimental set-up for the first and second target, respectively. The centers of the white empty ellipses and black empty ellipses are determined by the largest magnitude in the reconstructed images, and their radii are chosen such that each ellipse covers the whole bright area. It is clearly seen that the experimental configurations and the reconstruction positions are within experimental uncertainties.

In summary, by combining the rapid phase detection technique and wavefront reconstruction algorithm, we demonstrate that microwave radar imaging applications using spintronic microwave sensors are feasible. This technique can locate targets'

positions in a liquid environment, which could potentially be used for breast cancer detection.

5.4 Microwave sensor based clinical trial system

In the previous section, we demonstrated the feasibility of microwave imaging using a sensor based microwave radar system. In this section, we adapted this technique as the first step of a clinical trial system for breast cancer imaging. Note that the MTJ is a sensitive spintronic device and its ultra-thin (several nm) MgO layer can breakdown under several hundred mV [103]. This causes an electrostatic discharge issue when a volunteer is involved. In our lab-based system, a transient voltage suppressor is employed to protect the spintronic sensor. This greatly reduces the electrostatic discharge issue but does not eliminate it. In addition, our MTJ whose bonding wires are exposed to air, was designed for lab testing purpose. In the clinical based system, there is a risk that the volunteers may touch the bonding wires or the MTJ. This would damage it and bring additional risks to the volunteers. Both safety issue and limited testing time for the volunteer experiment have led us to adapt the rapid phase detection technique using a packaged semiconductor microwave sensor. While the performance of the two types of microwave sensor is comparable, the package and the higher breakdown voltage for the Schottky diode (several Volts) [52] allows the experiment to be carried out safely. Based on the clinical trial system, several phantom experiments were performed to explore and demonstrate the system's imaging capabilities. Then, using this clinical trial system, an experiment was performed, in which a volunteers' breasts were imaged.

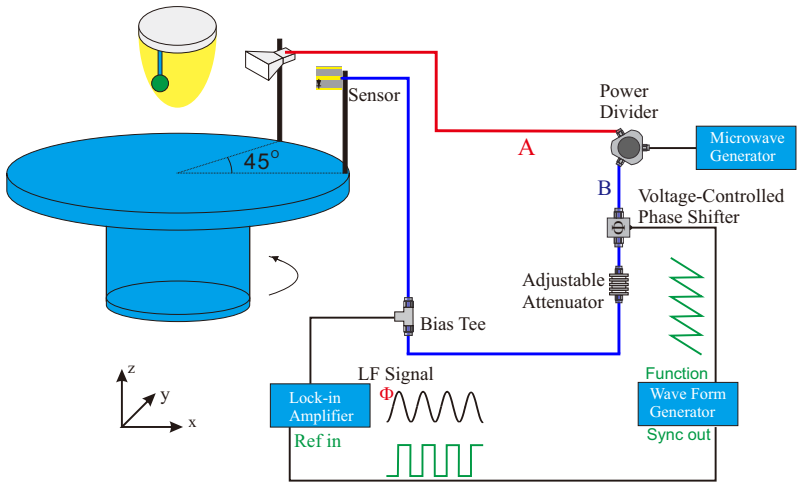

Figure 5.10: Schematic diagram of clinical trial system. The right side of the figure are the instruments required for rapid phase detection which is discussed in detail in Chapter 4. The antenna and the sensor are connected with a rotation stage. The breast phantom is held by a holder in the system.

As shown in Fig. 5.10, the clinical trial system is very similar to the previous system. They share the data collection part, which includes a microwave generator, power divider, voltage-controlled phase shifter, adjustable attenuator, a waveform generator, a lock-in amplifier and a horn antenna. A semiconductor sensor was employed for safety reasons. The difference between the two systems is the rotation stage. In the previous system, the stage was connected with the phantom or target so that the phantom or target is rotated during the experiment. However, in the clinical system, rotating the target would mean rotating the volunteer, which is difficult. Therefore, in the clinical system, the antenna and the sensor are rotated together.

During the scan process, the microwave cables move together with the antenna and the sensor. This may cause signal fluctuations and influence the system's imaging ability. Several phantom based experiments were performed to check the system's feasibility in practical applications. In the phantom based experiments, a breast-

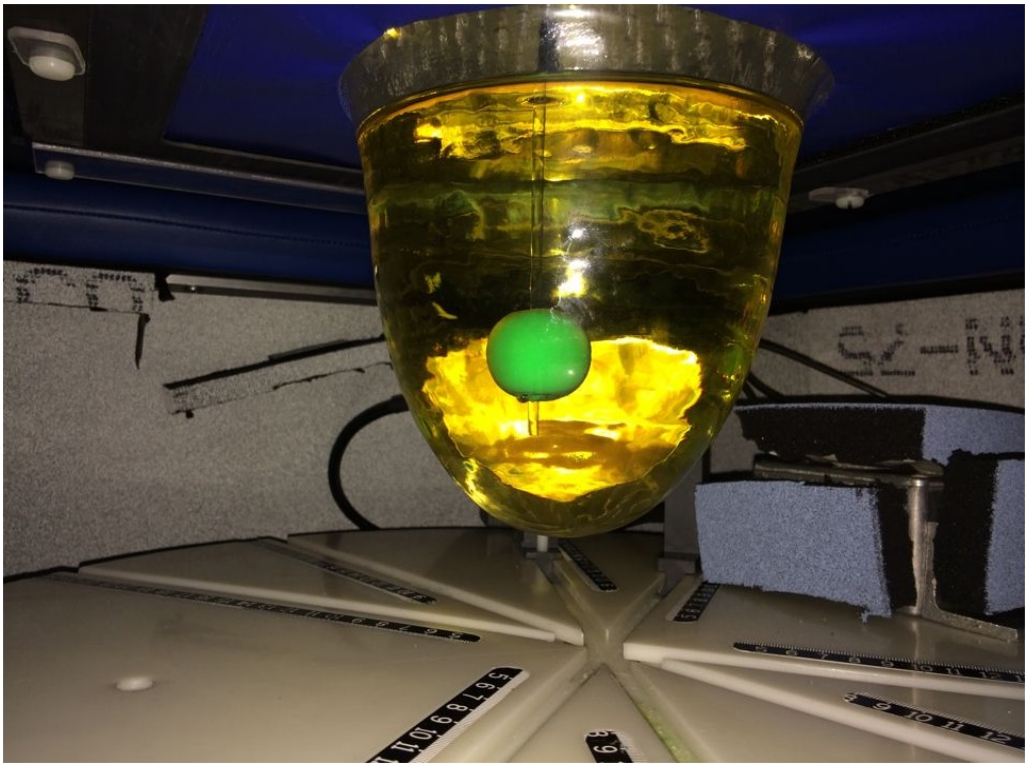

Figure 5.11: Picture of the breast phantom. An elliptical mould to simulates the human breast. Canola-oil and the green sphere simulate the fat and the tissue in the breast, respectively.

Table 5.1: The positions in the experiment and in the reconstructed images and the errors in x and y direction

Experiment Number	Configuration (cm)		Error (cm)	
	Experiment	Reconstruction	x	y
a	(0.7,-5.1)	(1.1, -4.6)	0.4	0.5
b	(-0.7, -2.2)	(-0.8, -2.6)	-0.1	-0.4
c	(-0.7, 0.7)	(-1.2, 0.7)	-0.5	0
d	(-3.7, -3.7)	(-3.9, -3.8)	-0.2	-0.1

shaped mould filled with Canola-oil was placed in the center of the plate. This simulated a human breast, with mainly fat tissues. In the mould, there was a 2.5 cm sphere made of a polymer-distilled-water-mixture to simulate tissues in the breast, as shown in Fig. 5.11.

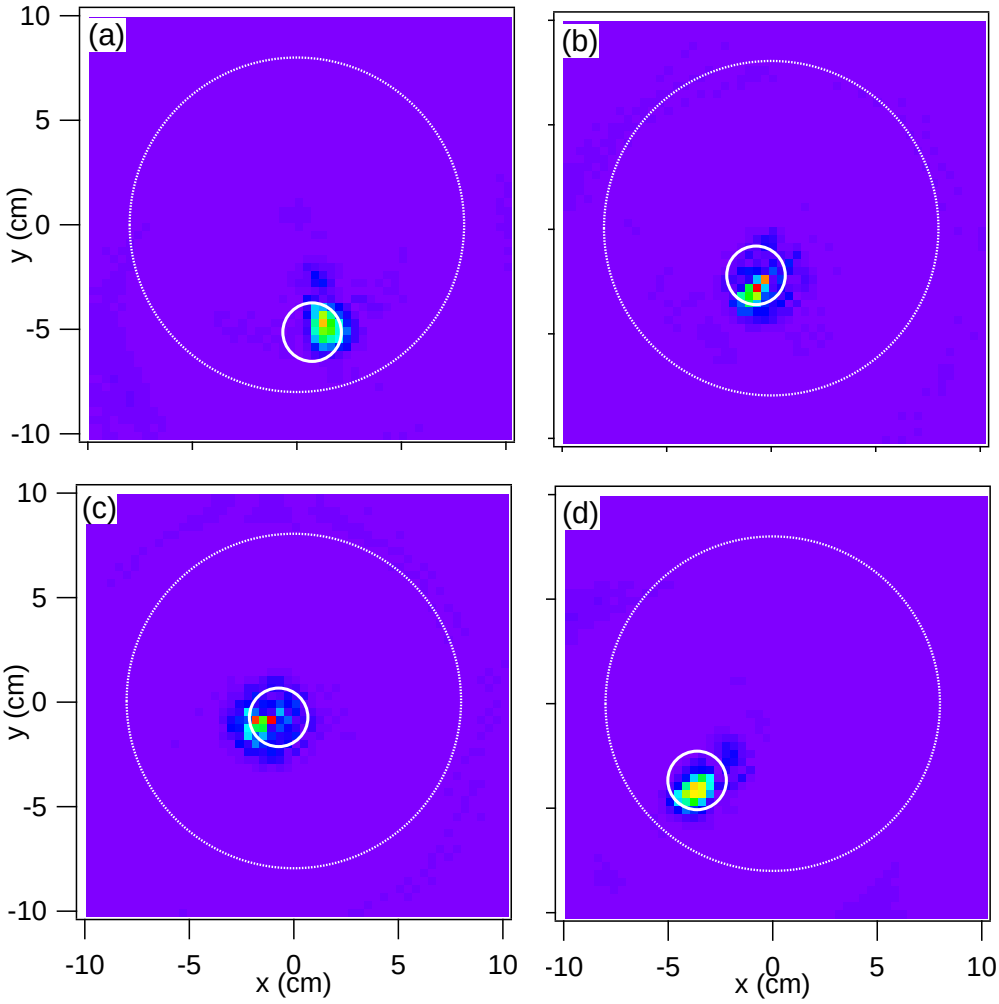

Figure 5.12: Reconstructed images for a sphere in different positions. The dashed big circle in each figure indicates the boundary of the phantom and the solid small circle in each figure indicates the position of the sphere.

In the experiment, the antenna and the sensor were placed 18 cm away from the rotation center with a separation of 45 degrees. The antenna and the sensor rotated around the breast phantom in steps of five degrees. At each position, a microwave signal, swept from 7 GHz to 13 GHz with frequency intervals of 0.1 GHz, was recorded. The sphere was placed at positions of (0.7, 5.1), (-0.7, 2.2), (-0.7, 0.7)

and (-3.7, -3.7) cm. Based on the measured microwave amplitude and phase, images were reconstructed by using the reconstruction algorithm discussed in Section 5.2. The reconstruction images are color mappings where different colors correspond to different microwave reflectivities, as shown in Fig. 5.12 (a), (b), (c) and (d). In Fig. 5.12, the hot spots are identified as the target's position locating at (1.1, -4.6), (-0.8, -2.6), (-1.2, 0.7) and (-3.9, -3.8) cm. The experimental configuration in each case is indicated by a solid white circle. The dashed white circle indicates the boundary of the mould. Table 5.1 summarizes all four experimental configurations and reconstructed results. The errors in the x direction are 0.4, -0.1, -0.5 and -0.2 cm, and the errors in the y direction are 0.5, -0.4, 0.0 and -0.1 cm. From the table, we can see that the system can identify the target positions within an error of 1 cm.

For practical applications, the system should have the ability to identify multiple targets. An extreme case is when the targets are attached together. In a second experiment, a 1.5 cm diameter water-filled glass sphere was added to demonstrate the system's ability in imaging multiple targets. In this experiment, the tissue sphere was placed at (-3.8, 2.7) cm with the water sphere attached. Four cases were investigated where the water sphere placed in the $+x$, $-y$, $-x$, $+y$ directions relative to the tissue sphere. The reconstructed images for all cases are plotted in Fig. 5.13. The dashed white circle indicates the boundary of the mould. In all four figures, hot spots identified as the tissue are at the position of (-3.8, 2.7) cm, in agreement with the experiment configuration, as shown by the solid white circle. The position change of the water is clearly revealed by the hot spots in the figures. Their positions are identified at (-1.9, 2.7), (-4.6, 0.8), (-4.2, 4.6) and (-5.8, 3.1) cm in Fig. 5.13(a), (b),

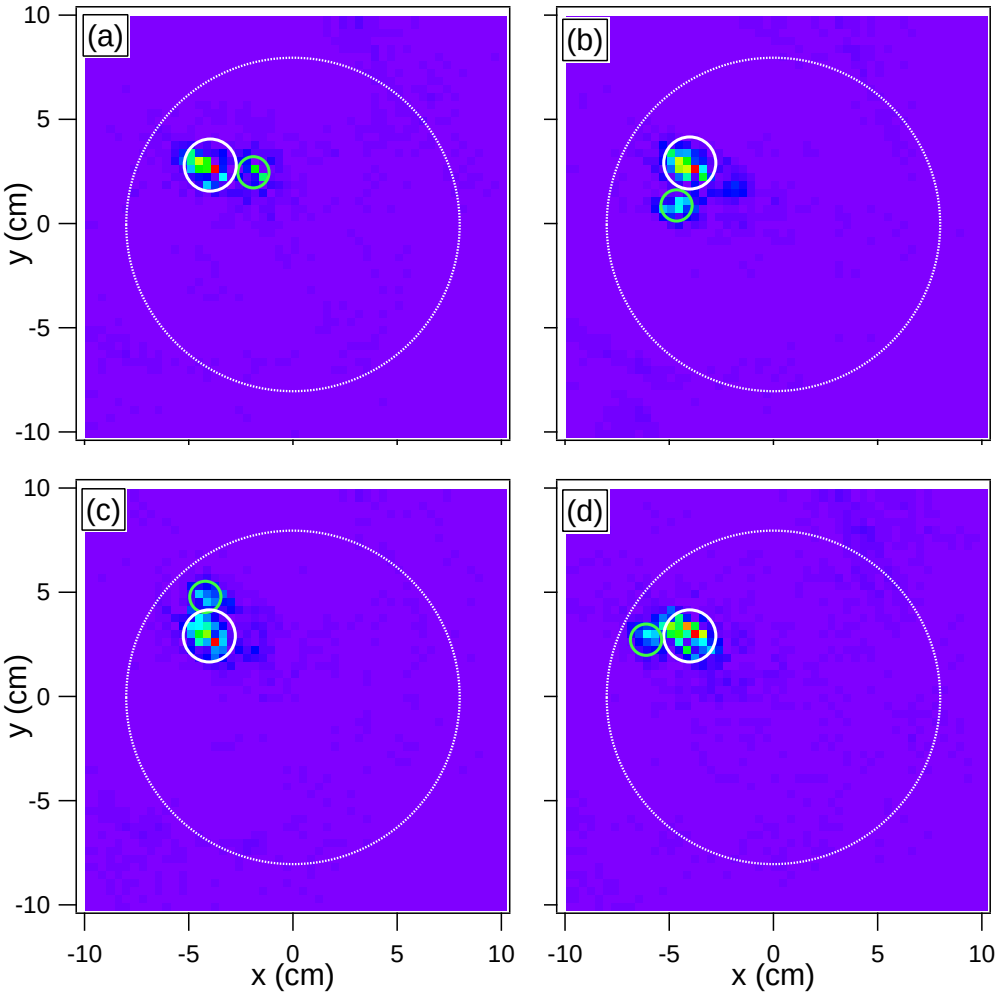

Figure 5.13: Reconstructed images for a tumor at different position with respect to the sphere. The dashed circle in each figure indicates the boundary of the phantom. The white and green solid circles indicate the positions of the sphere and the tumor, respectively.

(c) and (d), respectively. The expected positions of the water sphere are (-1.9, 2.7), (-3.8, 0.7), (-3.8, 4.7) and (-5.8, 2.7). These positions are indicated by green circles in the reconstruction images. As with the first experiment, the position error in each direction is within 1 cm.

5.4.1 Performance with low output power

In biomedical applications, microwaves will be strongly absorbed by the human body due to high water concentration in the body. Therefore, only a small ratio of microwaves can reach the region of interest in the patient. In addition, there is an upper limit for radiated microwave power that can be used, due to safety concerns. In order to be adapted to biomedical applications, the system must retain its imaging ability with low radiated microwave power. To verify the system's ability, a 2.5 cm diameter object was investigated under different microwave power levels, ranging from 23 dBm to -15 dBm. The same scan procedure as in the previous imaging experiment was performed. The reconstructed images using microwave output powers of 23 dBm, 15 dBm, 0 dBm, -10 dBm and -15 dBm are shown in Fig. 5.14 (a), (b), (c), (d) and (e), respectively. In all five figures, the hot spots appear at a position of (-3.5, 2.7), which is consistent with the experimental configuration and is indicated by the solid white circles. When output power ranges from 23 dBm to -10 dBm, the target is clearly observed. However, when the output power is -15 dBm, the noise becomes comparable to the signal so that the target's location is no longer reliable.

Fig. 5.15 is the response of amplitude as a function of output microwave power. A linear response is revealed since the response amplitude corresponds to the microwave power. From this experiment, even when output microwave power as low as -10 dBm, this system can still retain its imaging capability

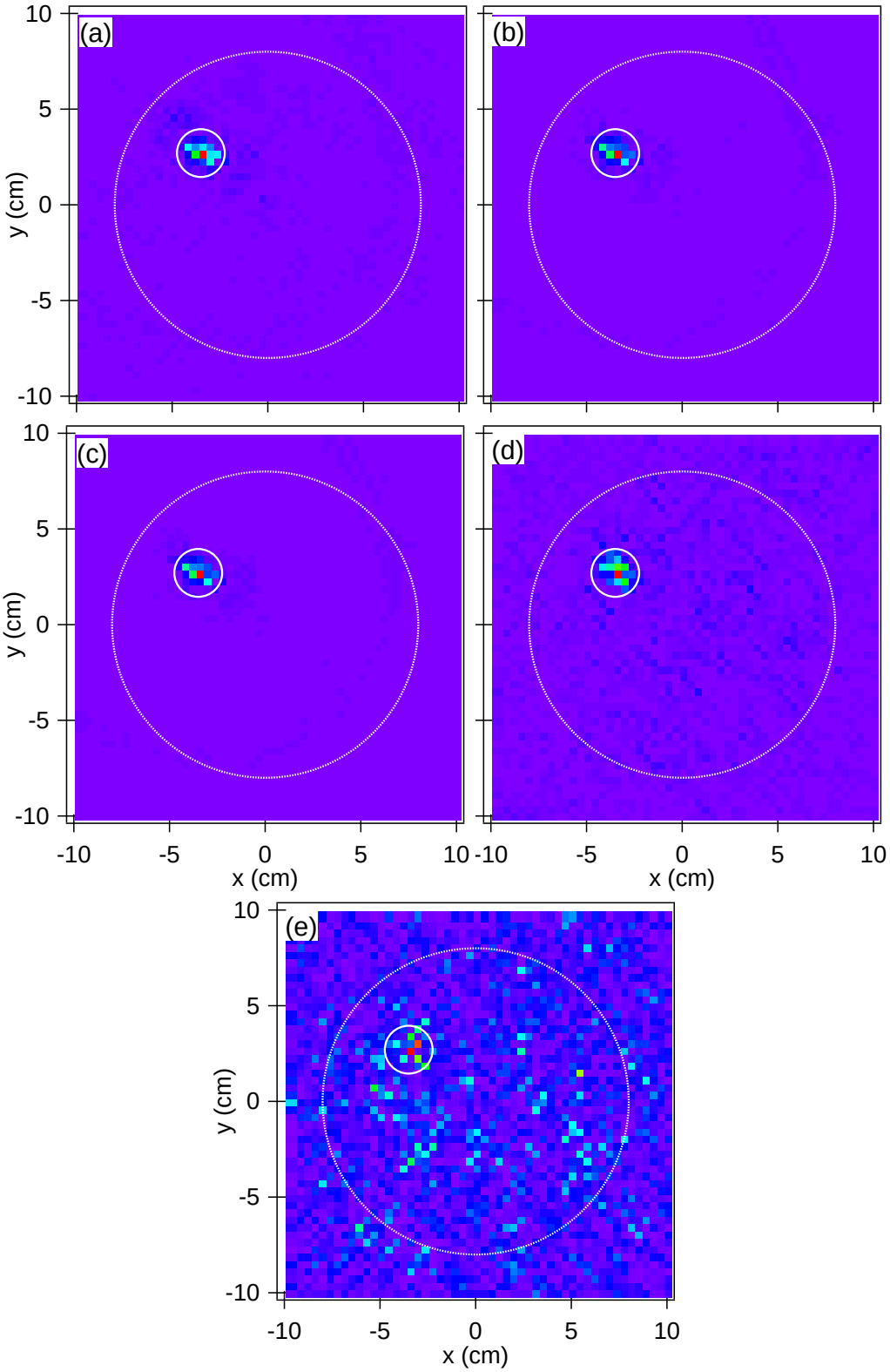

Figure 5.14: Reconstructed images when microwave output power is (a) 23 dbm, (b) 15 dBm, (c) 0 dBm, (d) -10 dBm and (e) -15 dBm. The dashed big circle in each figure indicates the boundary of the phantom and the solid small circle indicates the position of the sphere.

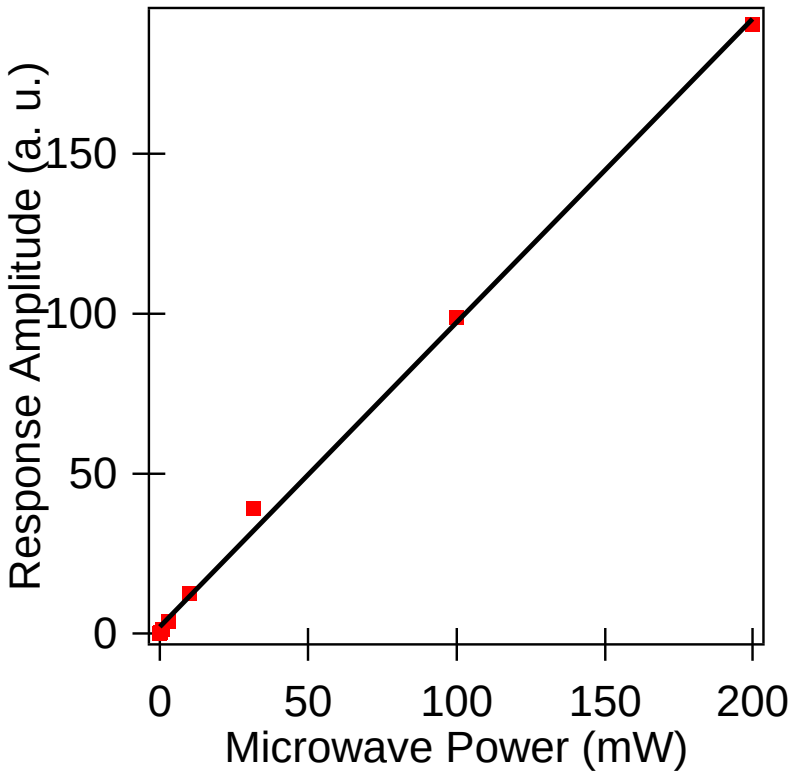

Figure 5.15: Signal amplitude in the reconstruction images as a function of output power. A linear response is revealed as expected.

5.4.2 Potential three-dimensional measurement

Though a 2D image reconstruction algorithm is employed, the system still has the potential to locate objects in 3D space when an additional scan in the z direction is performed. To demonstrate the feasibility of 3D application, three 2.5 cm diameter spheres held at different heights were investigated. Taking the highest target as the reference in z, the three targets are placed at (3.9 cm, 3.9 cm, 0 cm), (-3.9 cm, -3.9 cm, 3 cm) and (-3.9 cm, 3.9 cm, 8 cm).

In this experiment, the antenna and the sensor were lowered together with the plate using a lift stage. Scans at 12 heights were performed, ranging from 0 cm to

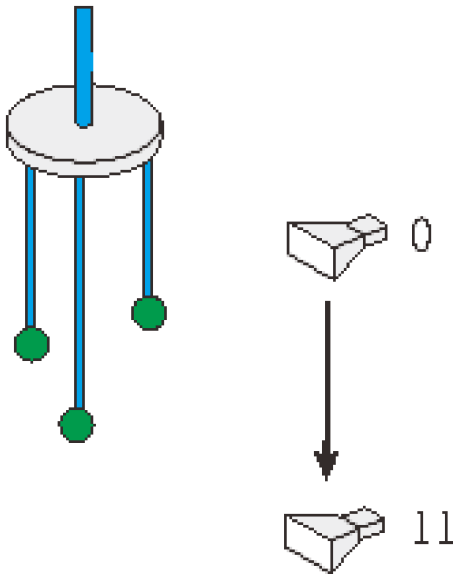

Figure 5.16: Schematic diagram showing how the height changes in the experiment. The antenna and the sensor moved from the top with a step of 1 cm in a range of 11 cm.

11 cm with a step of 1 cm. At each height, the antenna and sensor rotated around the object in steps of 5 degrees, as in the previous experiment procedure. After 360 degrees' rotation, the antenna and the sensor were lowered. Then the scanning process was repeated at each height, as shown in Fig. 5.16.

When the antenna and the sensor were at the same level as the target, less radiation was incident on the target due to the lower microwave power density. Thus, the reflection by the target was weaker and a weaker signal in the reconstructed image is expected. Using the 2D reconstructed algorithm to process the data obtained at each height separately, all three targets are revealed in the reconstruction images. Images when h= 0 cm, 3 cm, and 8 cm are selected and plotted in Fig. 5.17(a), (b), (c), where all figures use the same color scale so that we can direct compare the amplitudes.

From the Fig. 5.17(a), (b), (c), we can identify the three objects located at (3.5

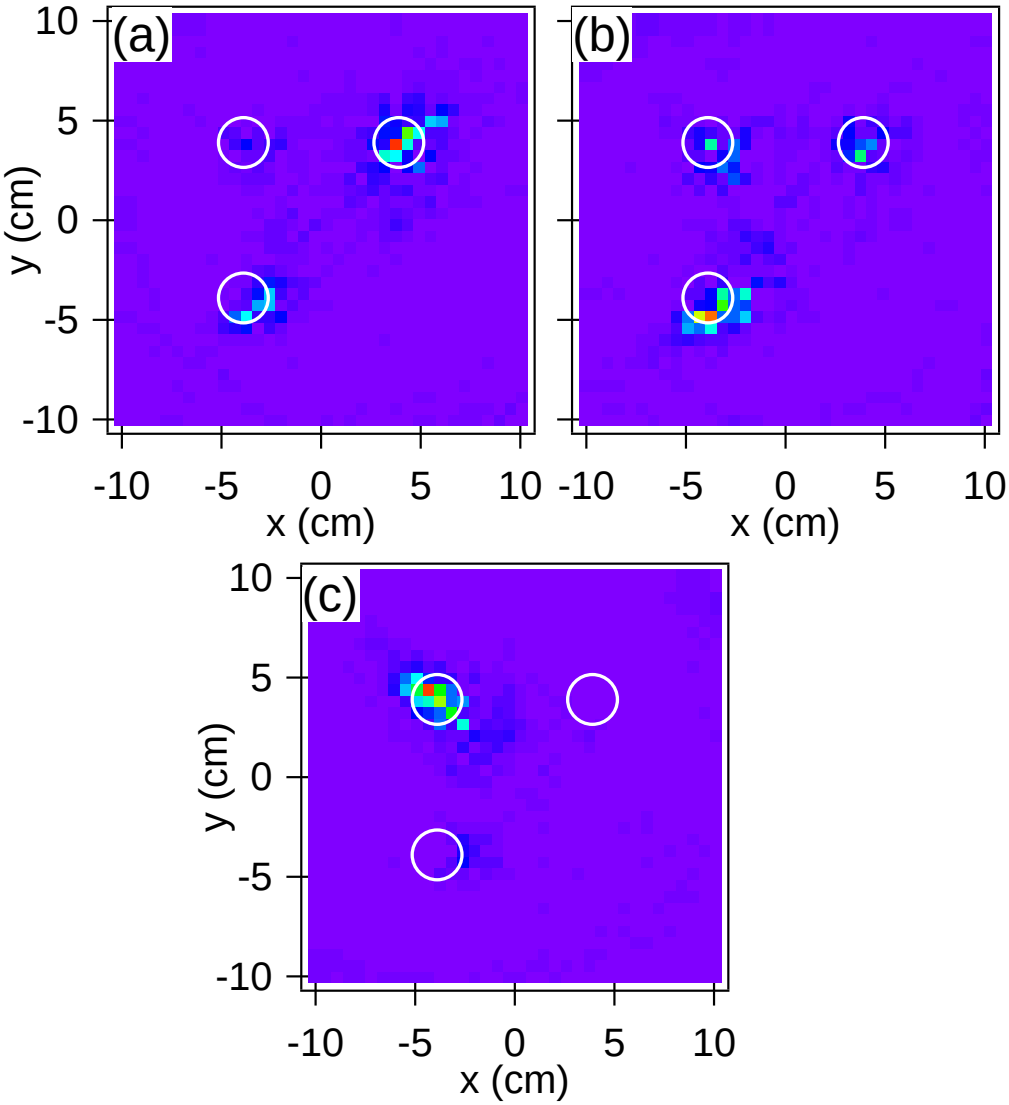

Figure 5.17: Reconstruction images when the height were (a) 0 cm, (b) 3 cm and (c) 8 cm.

cm, 4.1 cm), (-4.0 cm, -4.5 cm) and (-4.6 cm, 4.6 cm), respectively. In order to determine the targets' heights, we need to compare the targets' response amplitudes at different heights. The response amplitude is plotted as a function of height for each object in Fig. 5.18. From the response curves, the three target have the strongest response when height=0 cm, 3 cm, and 8 cm, respectively. This indicates the objects'

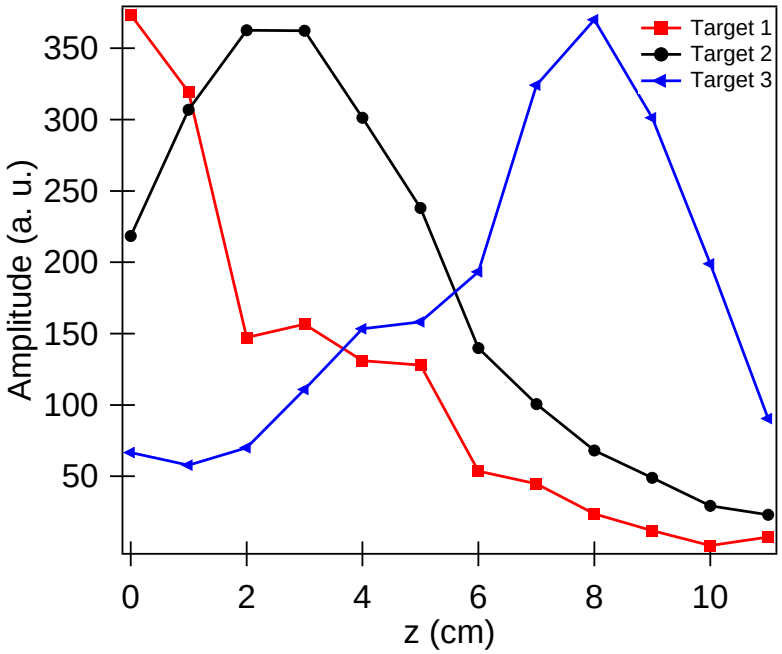

Figure 5.18: Reconstructed amplitude of each target as a function of height. The maximum amplitude for each target appeared at height 0 cm, 3 cm and 8 cm.

Table 5.2: The target positions in experiment and in the reconstructed images

Experimental Configuration	**Reconstruction position**
(3.9, 3.9, 0) cm	(3.5, 4.1, 0) cm
(-3.9, -3.9, 3) cm	(-4.0, 4.5, 3) cm
(-3.9, 3.9, 8) cm	(-4.6, 4.6, 8) cm

locations at these heights. Table 5.2 summarizes the expected objects' positions and the reconstructed positions. We can see that the error is within 1 cm. This verifies the system's potential in determining an object's position in 3D space.

5.4.3 Volunteer experiments

An experiment was performed to obtain microwave images of volunteers' breasts. Similar to the phantom based experiment, the sensor and the antenna were placed

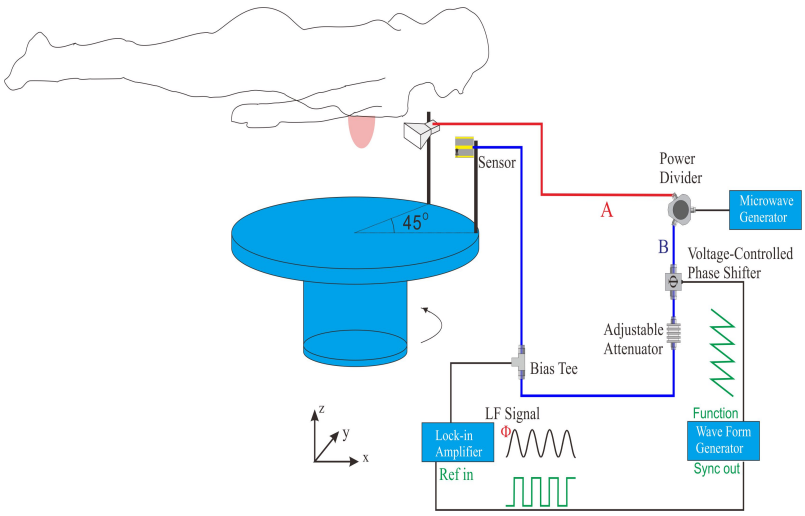

Figure 5.19: Schematic diagram of the clinical trial system. The right side of the figure are the instruments required for rapid phase detection which is discussed in detail in Chapter 4. The antenna and the sensor are connected with a rotation stage. The breast phantom is held by a holder in the system.

18 cm away from the rotation center with a 45° relative angle. The experiment setup is identical to the previous sections. As shown in Fig. 5.19, in the experiment, the volunteer laid on the bed and put one of her breasts in a hole in the bed. As in the phantom based experiment, the antenna and sensor rotated around the volunteer's breast in steps of five degrees. At each position, microwave signals ranging from 7 GHz to 13 GHz were recorded. During the scan process, the volunteer was required to keep motionless. The scan process was limited to 13 minutes for the benefit of the volunteer. A background collection was required for each volunteer since the bed deformation may be different for different volunteers. In the background collection step, the volunteer was required to lay on the bed without putting her breast into the hole. This process lasted the same time period as the breast scan. There were four volunteers involved in the experiment and ethics approval were obtained.

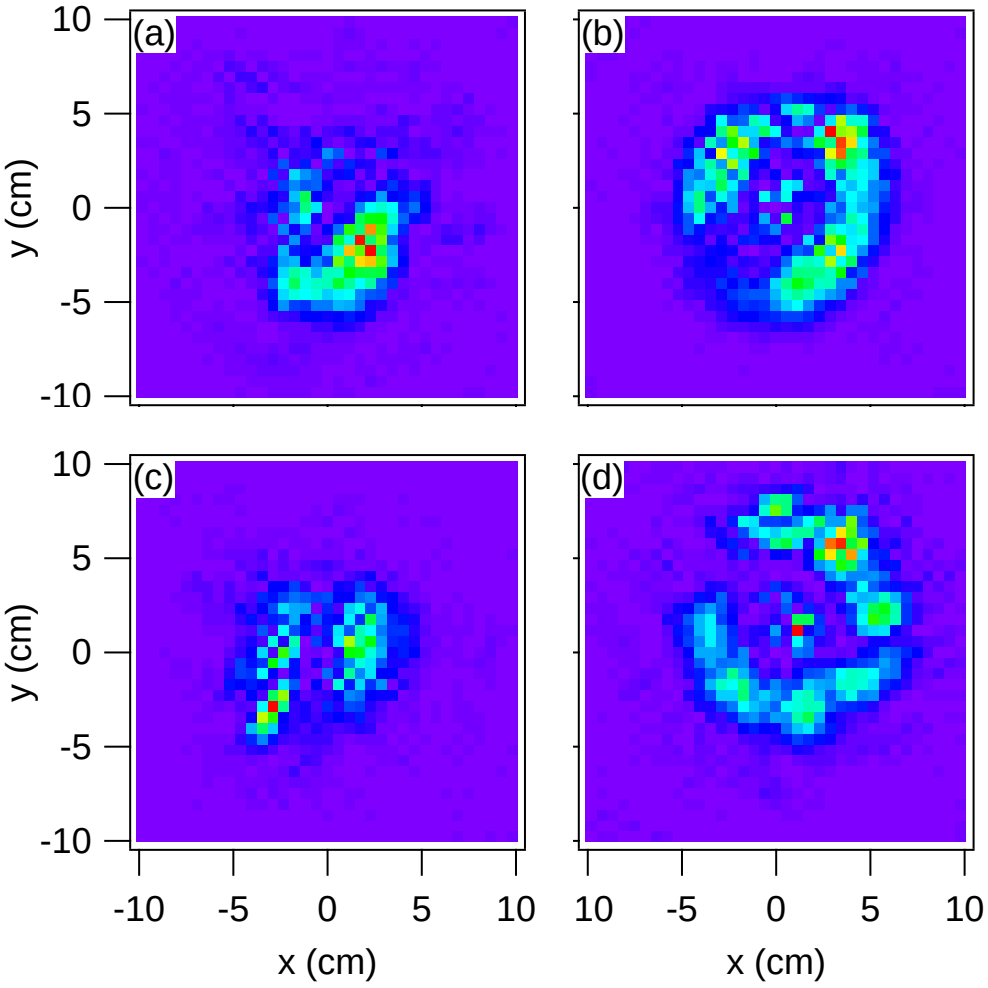

Figure 5.20: Reconstructed images from four different volunteers.

The subtraction of the breast data and the background data were used to create the reconstructed images. The reconstruction algorithm was identical to previous sections. The reconstructed images shown in Fig. 5.20. Figures 5.20(a), (b), (c), (d) are reconstruction images obtained from four different volunteers. In Fig. 5.20(b) and (d), circle shaped targets were observed. However, such circle shaped responses were not observed in Fig. 5.20(a) and (c). For each volunteer, the maximum response

amplitude appeared at (2.3, -2.3) cm, (3.4, 5.8) cm, (-2.9, -2.8) cm, and (1.1, 1.1), which corresponded to the strongest reflection point in each breast. Different images were obtained from different volunteers, indicating that the microwave could identify the differences in the volunteers' breasts. The differences may come from a lot of factors such as the sizes and shapes of the volunteers' breasts, and the different reflection coefficients of the skin. At this stage, there is too little information to understand the images. More information is required, which may come from either the microwave imaging technique or other imaging techniques.

For the microwave imaging technique, 3D images could provide more information than 2D images, whose potential feasibility was demonstrated in Section 5.4.2. In addition, a systematic study is required to characterize the microwave penetration velocity and loss in each breast tissue. Furthermore, a numerical model that takes these into account is desirable. Based on these items, the obtained 3D microwave image could be directly compared with other imaging techniques such as MRI.

In summary, we have developed a sensor based microwave imaging system. This imaging system can locate targets within an error of 1 cm. The system is capable of acquiring images even with an output power as low as -10 dBm. By performing a scan along the z axis, it is shown that the system has the potential to do 3D imaging. By adapting this imaging system for the volunteer experiment, the volunteers' breasts were imaged using microwave sensors.

5.5 Summary

In this chapter, by using the rapid phase detection technique, we have developed a sensor based microwave radar system. This radar system can locate a target's position in complex environments by employing a wavefront reconstruction algorithm. A clinical trial microwave imaging system was developed with the sensor based radar technique. By adapting this imaging system for volunteer experiments, images of volunteers' breast were obtained using a microwave sensor. Work in this chapter was published in Appl. Phys. Lett., 105, 122406 (2014) [49].

Chapter 6

Conclusion

6.1 Summary

Microwave technology is used extensively for a wide range of modern applications such as telecommunications, navigation and radar. This widespread use is the result of several advantages provided by the several centimetres wavelength of microwave radiation. First, the corresponding high frequency permits both broad bandwidth and high data transmission rates. Second, this wavelength permits smaller antenna sizes than lower frequency radiation. Microwave antennas can be easily used in integrated circuits – a key factor in the use of microwave technology for device applications such as smartphones.

The signal processing and analysis of microwaves requires highly sensitive microwave devices that are operational at room temperatures; in particular, the rectifying behaviors of semiconductor diodes play an important role. Within the next decade, the most commonly used device in rectifiers, the Schottky diode, will un-

doubtedly play a leading role, however, after more than 70 years of development, the performance of Schottky diodes has reached its limits [18].

The focus of this thesis is to demonstrate the potential of spintronic-based microwave detectors which utilize MTJs. In Section 3.3 and Section 4.2, the microwave amplitude and phase detection capabilities of a spin-rectification sensor are shown. The potential of this sensor for microwave imaging was demonstrated by detecting hidden objects as well as performing microwave antenna design and holographic and radar imaging in Section 3.4, Section 3.5, Section 4.3 and Chapter 5. Except for the clinical trial of microwave imaging for breast cancer detection discussed in Section 5.4, which was performed in the lab of Dr. Stephen Pistorius at the University of Manitoba, all experiments were carried out in the Dynamic Spintronics Group at the University of Manitoba.

For the next generation of microwave detectors utilizing MTJ devices, previous research and development has already led to an enhancement in MTJ sensitivity near the condition of ferromagnetic resonance, where the spin dynamics have a maximum impact on d.c. transport. As a consequence, recent breakthroughs in MTJ design have enabled order of magnitude enhancements in power sensitivity [29; 30; 32; 33; 34; 35; 36]. The spin rectification effect gets weaker when the microwave frequency is away from the resonant frequency. In the lab, this problem can be circumvented by an external magnetic field bias to alter the resonant frequency of an MTJ. But for device applications it would requires elements for providing an external field for the sensor operation and increases the complexity to design the system. To simplify the design of the first prototype imaging system using a spintronic sensor, in this thesis,

we have explored the Seebeck rectification effect [44], as detailed in Section 2.4, which allows the detection of broadband microwaves with a bandwidth greater than 10 GHz in the absence of any external magnetic bias. The discovery of non-resonant spin rectification paved a new way for developing spintronic microwave detectors, which allows them to be easily integrated into existing circuits without needing any extra components for magnetic bias.

While previous works have calibrated the MTJ sensitivity by direct microwave injection via coaxial cable [30; 32; 34], in Chapter 3 of this thesis we demonstrated the capability of MTJ devices to detect scattered microwave through the imaging of hidden objects [46]. Since the radiated power is larger than the scattering amplitude, we have explored the application of antenna characterization using MTJ in Section 3.5. In this case, the benefit of using a small microwave sensor is that there will be less perturbation of the microwave field that is being sensed, i.e. less destructive sensing [47].

In addition to the enhancement of power sensitivity, precise phase detection could provide information crucial for imaging reconstruction. In this thesis, we have developed a rapid phase detection method by using the lock-in technique [45], so that both microwave amplitude and phase can be precisely measured. The precision of this method has permitted through-the-wall-detection of human vital signs because the phase of scattered microwaves is periodically modulated by the chest wall movement during breathing and heartbeats [104].

The first steps towards implementing spin rectification devices for microwave imaging applications are presented in Chapter 4 and 5, using both holographic [48; 88]

and radar imaging [49]. The high sensitivity of spintronic microwave detectors allows coherent image reconstruction even in noisy environments. A holographic imaging system was built and the capability of identification of hidden objects was demonstrated [48; 88]. It was also shown that embedded defects immersed in a liquid could be located using the radar imaging technique. Using the microwave radar technique, a clinical trial microwave imaging system was developed. Based on this system, four volunteer experiments were performed, showing the system's capability of detecting strong reflection areas in human breasts.

In summary, during my thesis, using MTJ devices, microwave amplitude distributions were detected. A microwave holographic imaging system was developed which was able to image concealed targets. Furthermore, a microwave radar imaging system was developed which showed its potential in medical imaging. These results have demonstrated the feasibility of a spintronic sensor for microwave imaging applications and encourage us to continue the research and development of the spintronic based imaging system.

6.2 Future work

Based on the progress of spintronic sensor based imaging system, the future research could include two research tasks. One is to enhance the performances of spintronic sensors and the other is to optimize the imaging systems. For the first task, the following research and development seem timely:

(1) **Resonant detection at FMR condition**

In this thesis, I used non-resonant Seebeck rectification for microwave detection,

which has several advantages such as broadband detection and simple implementation. However, currently the highest sensitivity based on this working principle is only about a few hundred mV/mW[54], two order of magnitude smaller than that for resonant detection (up to 74,500 mV/mW)[35; 36]. If a magnetic field is used to bias the spintronic sensor working at the FMR condition, the detection capability may be significantly enhanced. Different from magnetic resonance imaging, where the whole unit under test should be biased by a magnetic field in order to excite the nuclear magnetic resonance, for the microwave imaging system based on the resonant detection, the magnetic field is only required to bias the spintronic sensor. This effect allows us to appropriately integrate a permanent magnet and/or an electromagnetic coil with the spintronic sensor. Notice that the neodymium magnet could provide a magnetic field higher than 1 Tesla, corresponding to a microwave frequency of up to 30 GHz. Changing the dc bias current for the electromagnetic coil would allow the resonant detection for a range of microwave frequency and achieve a broadband microwave measurement.

(2) **Microwave magnetic field detection**

While different methods have been developed for microwave detection, most of them measure microwave e-fields. In contrast, current state-of-the-art, microwave h-field sensors are still based on Faradays law by detecting the change of magnetic flux through a loop. Its sensitivity scales down with the square of the diameter of the loop. This factor makes it difficult for applications in the near field, where the microstructured h-field sensor is desirable in order to achieve sub-wavelength resolution.

One of the unique features of spintronic devices is the capability to detect microwave h-field besides the microwave e-field. It is well known that the impact of microwave h-field on the produced rectification voltage can be significantly enhanced near the frequency of FMR through the susceptibility tensor defined in Section 2.3. This feature may allow the high sensitive detection of microwave h-field. The ability to detect microwave e-field in the non-resonant condition has been demonstrated in this thesis. In the future, a near field imaging system will be developed using spintronic sensors, which may achieve both h-field and e-field imaging by turning the FMR condition on or off. To verify this capability as well as compare the spatial resolution with the traditional loop antenna, the coplanar waveguide could be the first test sample as the distribution of microwave h-field and e-field can be well calculated. The capability for measuring the spatial distribution of both microwave h-field and e-field using the spintronic sensor may allow the generation of better microwave imaging, making it more useful for fields such as biomedicine, security services, material characterization, etc.

During my thesis, two prototype imaging systems based on the spintronic sensor have been built and the preliminary results have demonstrated the capability of spintronic devices for microwave imaging applications. To improve the performances of the systems, the following research should be carried out in the future.

(3) **Noise analysis**

For any practical applications, noise analysis is essential to improve the performance of the system. During my thesis, my research focused on building the prototype and demonstrating the feasibility of spintronic sensor based system for microwave

imaging application. The next step should be to study the noise properties of the system, which mainly includes the characterization of the sensor's thermal noise and the shot noise, the crosstalk and interference between sensor elements, and the noise from equipment. This research will guide the optimization of imaging systems using the spintronic sensor.

(4) **Full characterization of the imaging system**

In order to characterize the full functionality of these systems, more systematic experiments should be carried out in the future, which may include the determination of spatial resolution, stand-off distance, and penetration depth. Some preliminary results related to the spatial resolution have been presented in Section 4.3.4, which depends on the stand-off distance, scan aperture, and output microwave power. A detailed data sheet of the specification of the imaging system should be made so that the sensor based imaging system can be compared with the currently existing approaches based on microwave antennas.

Generally speaking, by using lower frequency microwaves, a larger penetration depth can be achieved. But the resolution may be not high enough for target identification. As the spintronic sensor is a broadband microwave detector (preliminary results shows a range up to 40 GHz), our proposed method is to develop sensor-based ultra-wideband microwave technology, where low frequency microwaves meet the requirement of penetration and high frequency microwaves meet the requirement of resolution. By combining them, this approach could solve the contradiction between penetration and resolution using conventional single frequency or narrowband microwave approach. In addition, broadband microwave measurements also carry the

information of range resolution. It is worthwhile to study the 3D imaging technique based on spintronic sensors by combining broadband microwave measurements with the existing 2D holographic imaging, as it could provide additional information such as the depths and the relative positions of objects.

(5) **Data acquisition time**

The data acquisition time plays a critical role in the performance of the imaging system, especially for developing 3D imaging. Both the current holographic imaging system and the radar imaging system developed during my thesis use a single spintronic sensor system, which is attached to a mechanical stage. Currently, the x-y stage moved with a velocity of 2 cm/s and it took about 20 minutes to acquire a 2D holographic image. Obviously, the time consumption is not limited by the sensor to catch the signal, but by the scan stage and communication between instruments. In the future, more efforts can be made to reduce the data acquisition time by solving/reducing these factors. With a faster scanner, less data acquisition time is expected. The data acquisition time can be further reduced by optimizing the scan process. The experiment shown in the thesis was a point-by-point scan, which required the sensor to stop at each sampling position for tens of milliseconds. In the optimized scan process, the x-y stage would move with a constant speed without stopping and the lock-in amplifier would record the data simultaneously. This movement could be compensated by modifying the code in the data analysis process.

It should be noted that the mechanical motion is much slower than an electrical switch. Therefore a sensor array could be designed and fabricated in the future, which should significantly decrease the data acquisition time. This microwave sensor array

is like the electro-optical devices used in digital cameras, where millions of optical sensors are integrated into an array. Therefore, the development of spintronic sensor array for microwave imaging is essential for future practical applications. While large spintronic sensor array such as MRAM indeed exists, it is not designed for the purpose of microwave detection. Furthermore, different from optical sensors, the microwave sensors need to measure the phase besides its amplitude, which requires feeding additional reference signal into sensors. The key technical challenge here is to optimize the reference path so that the reference signal sent to each sensor has identical amplitude and phase or its amplitude and phase can be well calibrated.

Appendix A

Publication list

A.1 U.S. Patent Application

C.-M. Hu, Y. S. Gui, **L. Fu**. Rapid microwave phase detection with a solid state device. *United States Patent Pending*, No.: WO 2015063596 A1, May 7, 2015.

A.2 First Author Papers

L. Fu, Y. S. Gui, and C.-M. Hu. Through-wall bio-radio location and characterization of human activities. *Meas. Sci. Technol.*, accepted.

L. Fu, Y. S. Gui, L. H. Bai, H. Guo, H. Abou-Rachid, and C.-M. Hu. Microwave holography using a magnetic tunnel junction based spintronic microwave sensor. *J. Appl. Phys.*, 117:213902, 2015.

L. Fu, Y. S. Gui, Y. Xiao, M. Jaidann, H. Guo, H. Abou-Rachid, and C.-M. Hu. Detection of concealed targets using spintronic microwave sensor. *Proc. SPIE*,

9454:945406, 2015.

L. Fu, W. Lu, D.R. Herrera, D.F. Tapia, Y.S. Gui, S. Pistorius, C.-M. Hu. Microwave radar imaging using a solid state spintronic microwave sensor. *Appl. Phys. Lett.*, 105:122406, 2014.

L. Fu, Z. X. Cao, S. Hemour, K. Wu, D. Houssameddine, W. Lu, S. Pistorius, Y. S. Gui and C.-M. Hu. Microwave reflection imaging using a magnetic tunnel junction based spintronic microwave sensor. *Appl. Phys. Lett.*, 101:232406, 2012.

A.3 Invited Papers

Y.S. Gui, Ali M. Mehrabani, Daniel Flores-Tapia, **L. Fu**, L.H. Bai, S. Pistorius, Lot Shafai, and C.-M. Hu. New horizons for microwave applications using spin caloritronics. *Solid State Communications*, 198:45, 2014.

Z.X. Cao, W. Lu, **L. Fu**, Y.S. Gui, C.-M. Hu. Spintronic microwave imaging. *Appl. Phys. A*, 111:329, 2013.

A.4 Co-author Papers

D. Flores-Tapia, D. Rodriguez, M. Solis, N. Kopotun, S. Latif, O. Maizlish, **L. Fu**, Y. S. Gui, C.-M. Hu, S. Pistorius. Experimental feasibility of multistatic holography for breast microwave radar image reconstruction. *Medical Physics*, accepted.

H. J. Tang, S. Kaur, **L. Fu**, B. M. Yao, X. Li, H. M. Gong, Y. S. Gui, and C.-M. Hu. Life signal detection using an on-chip split-ring based solid state microwave sensor. *Appl. Phys. Lett.*, 105:133703, 2014.

B. M. Yao, **L. Fu** , X. S. Chen, W. Lu, L. H. Bai, Y. S. Gui and C.-M. Hu. Rapid microwave phase detection based on a solid state spintronic device. *Appl. Phys. Lett.*, 104:062408, 2014.

B. M. Yao, **L. Fu**, X. S. Chen, W. Lu, H. Guo, Y. S. Gui and C.-M. Hu. Ground penetrating detection using miniaturized radar system based on solid state microwave sensor. *Rev. Sci. Instrum.*, 84:124702, 2013.

Fuchun Xi, Lijian Zhang, Jie Xu, **L. Fu**, Yongsheng Gui, Can-Ming Hu, Lei Zhou, Shan Qiao, and Zhenghua An. Electromagnetic Field Enhancement and Its Application in Spin Rectification. *Applied Physics Express*, 6: 103002, 2013.

Z. H. Zhang, Y. S. Gui, **L. Fu**, X. L. Fan, J. W. Cao, D. S. Xue, P. P. Freitas, D. Houssameddine, S. Hemour, K. Wu, and C.-M. Hu. Seebeck Rectification Enabled by Intrinsic Thermoelectrical Coupling in Magnetic Tunneling Junctions. *Phys. Rev. Lett.*, 109:037206, 2012.

Z. X. Cao, M. Harder, **L. Fu**, B. Zhang, W. Lu, G. E. Bridges, Y. S. Gui, and C.-M. Hu. Nondestructive two-dimensional phase imaging of embedded defects via on-chip spintronic sensor. *Appl. Phys. Lett.*, 100:252406 (2012).

Bibliography

[1] D. Pozar. *Microwave Engineering*. John Wiley and Sons, fourth edition, 2012.

[2] L. Diener. Microwave near-field imaging with open-ended waveguide—Comparison with other techniques of nondestructive testing. *Research in Nondestructive Evaluation*, 7:137, 1995.

[3] M. Golosovsky, A. Lann, and D. Davidov. A millimeter-wave near-field scanning probe with an optical distance control. *Ultramicroscopy*, 71:133, 1998.

[4] H. Sezer, L. Li, Z. Wu, B. Anderson, and P. Williams. Non-destructive microwave evaluation of TBC delamination induced by acute angle laser drilling. *Measurement Science and Technology*, 18:167, 2006.

[5] M. Sayar, D. Seo, and K. Ogawa. Non-destructive microwave detection of layer thickness in degraded thermal barrier coatings using K- and W-band frequency range. *NDT and E International*, 42:398, 2009.

[6] D. J. Cavalieri, B. A. Burns, and R. G. Onstott. Investigation of the effects of summer melt on the calculation of sea ice concentration using active and passive microwave data. *Journal of Geophysical Research*, 95:5359, 1990.

[7] W. J. Plant. A model for microwave Doppler sea return at high incidence angles: Bragg scattering from bound, tilted waves. *Journal of Geophysical Research*, 102:21131, 1997.

[8] D. V. Mühll, C. Hauck, and H. Gubler. Mapping of mountain permafrost using geophysical methods. *Progress in Physical Geography*, 26:643, 2002.

[9] A. Kaab. Remote sensing of permafrost-related problems and hazards. *Permafrost and Periglacial Processes*, 136:107, 2008.

[10] S. C. Hagness, A. Taflove, and J. E. Bridges. Two-dimensional FDTD analysis of a pulsed microwave confocal system for breast cancer detection: Fixed-focus and antenna-array sensors. *IEEE Transactions on Biomedical Engineering*, 45:1470, 1998.

[11] E .C. Fear and M. A. Stuchly. Microwave detection of breast cancer. *IEEE Transactions on Microwave Theory and Techniques*, 48:1854, 2000.

[12] E. C. Fear, X. Li, S. C. Hagness, and M. A. Stuchly. Confocal microwave imaging for breast cancer detection: Localization of tumors in three dimensions. *IEEE Transactions on Biomedical Engineering*, 49:812, 2002.

[13] E. C. Fear, P. M. Meaney, and M. A. Stuchly. Microwaves for breast cancer detection? *IEEE Potentials*, 22:12, 2003.

[14] B. E. Henty and D. D. Stancil. Multipath-enabled super-resolution for rf and microwave communication using phase-conjugate arrays. *Physical Review Letters*, 93:243904, 2004.

[15] I. S. Lin, J. D. McKinney, and A. M. Weiner. Photonic synthesis of broadband microwave arbitrary waveforms applicable to ultra-wideband communication. *IEEE Microwave and Wireless Components Letters*, 15:226, 2005.

[16] M. Yamashita and Makimoto S. *Microwave resonators and filters for wireless communication: theory, design and application.* Springer, 2000.

[17] R. E. Collin. *Foundations for microwave engineering.* John Wiley and Sons, 2001.

[18] S. Hemour and K. Wu. Radio-Frequency Rectifier for Electromagnetic Energy Harvesting: Development Path and Future Outlook. *Proceedings of the IEEE*, 102:1667, 2014.

[19] P. S. Carter and H. H. Beverage. Early History of the Antennas and Propagation Field until the End of World War I, Part I - Antennas. *Proceedings of the IRE*, 50:679, 1962.

[20] J-M Dilhac. Edouard Branley, the coherer, and the Branley effect. *IEEE Communications Magazine*, 47:20, 2009.

[21] J. E. Brittain. Electrical Engineering Hall of Fame : Jonathan Zenneck. *Proceedings of the IEEE*, 93:198, 2005.

[22] P. Russer. Ferdinand Braun - A pioneer in wireless technology and electronics. *Proceedings of the 39th European Microwave Conference*, 229:547, 2009.

[23] L. Hoddeson. The Discovery of the Point-Contact Transistor. *Historical Studies in the Physical Sciences*, 12:41, 1981.

[24] J. J. Sakurai and J. J. Napolitano. *Modern Quantum Mechanics*. Addison-Wesley, second edition, 2010.

[25] M. Goldhaber. Samuel A. Goudsmit. *Physics Today*, 32:71, 1979.

[26] W. Thomson. On the Electro-Dynamic Qualities of Metals:–Effects of Magnetization on the Electric Conductivity of Nickel and of Iron. *Proceedings of the Royal Society of London*, 8:546, 1856.

[27] J. Nickel. Magnetoresistance Overview. *HP Labs Technical Reports*, pages HPL–95–60, 1995.

[28] S. M Thompson. The discovery, development and future of GMR: The Nobel Prize 2007. *Journal of Physics D: Applied Physics*, 41:93001, 2008.

[29] S. Kaka, M. R. Pufall, W. H. Rippard, T. J. Silva, S. E. Russek, and J. A. Katine. Mutual phase-locking of microwave spin torque nano-oscillators. *Nature*, 437:389, 2005.

[30] A. A. Tulapurkar, Y. Suzuki, A. Fukushima, H. Kubota, H. Maehara, K. Tsunekawa, D. D. Djayaprawira, N. Watanabe, and S. Yuasa. Spin-torque diode effect in magnetic tunnel junctions. *Nature*, 438:339, 2005.

[31] Skyworks. SM76XX Datasheet. *Surface Mount Mixer and Detector Schottky Diodes*, page 1, 2015.

[32] C. Wang, Y. T. Cui, J. Z. Sun, J. A. Katine, R. A. Buhrman, and D. C. Ralph. Sensitivity of spin-torque diodes for frequency-tunable resonant microwave detection. *Journal of Applied Physics*, 106:053905, 2009.

[33] J. Zhu, J.A. Katine, G. E Rowlands, Y.-J. Chen, Z. Duan, J. G. Alzate, P. Upadhyaya, J. Langer, P. K. Amiri, K. L. Wang, and I. N. Krivorotov. Voltage-induced ferromagnetic resonance in magnetic tunnel junctions. *Physical Review Letters*, 108:197203, 2012.

[34] S. Ishibashi, K. Ando, T. Seki, T. Nozaki, H. Kubota, S. Yakata, H. Maehara, A. Fukushima, S. Yuasa, and Y. Suzuki. High spin-torque diode sensitivity in CoFeB/MgO/CoFeB magnetic tunnel junctions under DC bias currents. *IEEE Transactions on Magnetics*, 47:3373, 2011.

[35] S. Miwa, S. Ishibashi, H. Tomita, T. Nozaki, E. Tamura, K. Ando, N. Mizuochi, T. Saruya, H. Kubota, K. Yakushiji, T. Taniguchi, H. Imamura, A. Fukushima, S. Yuasa, and Y. Suzuki. Highly sensitive nanoscale spin-torque diode. *Nature materials*, 13:50, 2014.

[36] B. Fang, M. Carpentieri, X. Hao, H. Jiang, J. A. Katine, I. N. Krivorotov, B. Ocker, J. Langer, K. L. Wang, B. Zhang, B. Azzerboni, P. K. Amiri, G. Finocchio, and Z. Zeng. Giant spin-torque diode sensitivity at low input power in the absence of bias magnetic field. *Nature Communications*, 7:11259, 2016.

[37] International Commission on Non-Ionizing Radiation Protection (ICNIRP). Guidelines for limiting exposure to time-varying electric, magnetic, and electromagnetic fields (up to 300 GHz). *Health Physics*, 74:494, 1998.

[38] Y. S. Gui, S. Holland, N. Mecking, and C.-M. Hu. Resonances in ferromagnetic gratings detected by microwave photoconductivity. *Physical Review Letters*, 95:056807, 2005.

[39] Y. S. Gui, N. Mecking, X. Zhou, G. Williams, and C.-M. Hu. Realization of a room-temperature spin dynamo: The spin rectification effect. *Physical Review Letters*, 98:107602, 2007.

[40] L. H. Bai, Y. S. Gui, A. Wirthmann, E. Recksiedler, N. Mecking, C.-M. Hu, Z. H. Chen, and S. C. Shen. The rf magnetic-field vector detector based on the spin rectification effect. *Applied Physics Letters*, 92(3):032504, 2008.

[41] A. Wirthmann, Xiaolong Fan, Y. S. Gui, K. Martens, G. Williams, J. Dietrich, G. E. Bridges, and C.-M. Hu. Direct phase probing and mapping via spintronic michelson interferometry. *Physical Review Letters*, 105:017202, 2010.

[42] X. F. Zhu, M. Harder, J. Tayler, A. Wirthmann, B. Zhang, W. Lu, Y. S. Gui, and C.-M. Hu. Nonresonant spin rectification in the absence of an external applied magnetic field. *Physical Review B*, 83:140402(R), 2011.

[43] X. F. Zhu, M. Harder, A. Wirthmann, B. Zhang, W. Lu, Y. S. Gui, and C.-M. Hu. Dielectric measurements via a phase-resolved spintronic technique. *Physical Review B*, 83:104407, 2011.

[44] Z. H. Zhang, Y. S. Gui, L. Fu, X. L. Fan, J. W. Cao, D. S. Xue, P. P. Freitas, D. Houssameddine, S. Hemour, K. Wu, and C.-M. Hu. Seebeck rectification enabled by intrinsic thermoelectrical coupling in magnetic tunneling junctions. *Physical Review Letters*, 109:037206, 2012.

[45] B. M. Yao, L. Fu, X. S. Chen, W. Lu, L. H. Bai, Y. S. Gui, and C.-M. Hu. Rapid

microwave phase detection based on a solid state spintronic device. *Applied Physics Letters*, 104:062408, 2014.

[46] L. Fu, Z. X. Cao, S. Hemour, K. Wu, D. Houssameddine, W. Lu, S. Pistorius, Y. S. Gui, and C.-M. Hu. Microwave reflection imaging using a magnetic tunnel junction based spintronic microwave sensor. *Applied Physics Letters*, 101:232406, 2012.

[47] Y.S. Gui, Ali M. Mehrabani, Daniel Flores-Tapia, L. Fu, L.H. Bai, S. Pistorius, Lot Shafai, and C.-M. Hu. New horizons for microwave applications using spin caloritronics. *Solid State Communications*, 198:45, 2014.

[48] L Fu, Y S Gui, L H Bai, H Guo, and C.-M. Hu. Microwave holography using a magnetic tunnel junction based spintronic microwave sensor. *Journal of Applied Physics*, 117:213902, 2015.

[49] L. Fu, W. Lu, D. Rodriguez Herrera, D. Flores Tapia, Y. S. Gui, S. Pistorius, and C.-M. Hu. Microwave radar imaging using a solid state spintronic microwave sensor. *Applied Physics Letters*, 105:122406, 2014.

[50] M. Bass, P. A. Franken, F. Ward, and G. Weinreich. Optic Rectification. *Physical Review Letters*, 9:446, 1962.

[51] Ingrid Wilke and Suranjana Sengupta. Nonlinear Optical Techniques for Terahertz Pulse Generation and Detection-Optical Rectification and Electrooptic Sampling. *Terahertz Spectroscopy: Principles and Applications*, page 41, 2008.

[52] B. L. Sharma. *Metal-semiconductor Schottky barrier junctions and their applications*. Plenum Press, 1984.

[53] J. L. Hesler, T. W. Crowe, and V. Diodes. Responsivity and noise measurements of zero-bias Schottky diode detectors. *18th International Symposium on Space Terahertz Technology*, page 89, 2007.

[54] Y. S. Gui, Y. Xiao, L. H. Bai, S. Hemour, Y. P. Zhao, D. Houssameddine, K. Wu, H. Guo, and C.-M. Hu. High sensitivity microwave detection using a magnetic tunnel junction in the absence of an external applied magnetic field. *Applied Physics Letters*, 106:152403, 2015.

[55] I. Žutić, J. Fabian, and S. D. Sarma. Spintronics: Fundamentals and applications. *Reviews of Modern Physics*, 76:323, 2004.

[56] Y. S. Gui, L. H. Bai, and C.-M. Hu. The physics of spin rectification and its application. *Science China: Physics, Mechanics and Astronomy*, 56:124, 2013.

[57] U.A. Bakshi and A.V. Bakshi. *Antenna And Wave Propagation*. Technical Publications, 2009.

[58] J. D. Jackson. *Classical Electrodynamics*. John Wiley and Sons, 1999.

[59] D. R. Smith, J. B. Pendry, and M. C. K. Wiltshire. Metamaterials and Negative Refractive Index. *Science*, 305:788, 2004.

[60] M. Julliere. Tunneling between ferromagnetic films. *Physics Letters A*, 54:225, 1975.

[61] T. Miyazaki and N. Tezuka. Giant magnetic tunneling effect in Fe/Al2O3/Fe junction. *Journal of Magnetism and Magnetic Materials*, 139:L231, 1995.

[62] S. Ikeda, J. Hayakawa, Y. Ashizawa, Y. M. Lee, K. Miura, H. Hasegawa, M. Tsunoda, F. Matsukura, and H. Ohno. Tunnel magnetoresistance of 604% at 300 K by suppression of Ta diffusion in CoFeBMgOCoFeB pseudo-spin-valves annealed at high temperature. *Applied Physics Letters*, 93:082508, 2008.

[63] M. Walter, J. Walowski, V. Zbarsky, M. Münzenberg, M. Schäfers, D. Ebke, G. Reiss, A. Thomas, P. Peretzki, M. Seibt, J. S. Moodera, M. Czerner, M. Bachmann, and C. Heiliger. Seebeck Effect in Magnetic Tunnel Junctions. *Nature Materials*, 10:742, 2011.

[64] N. Liebing, S. Serrano-Guisan, K. Rott, G. Reiss, J. Langer, B. Ocker, and H. W. Schumacher. Tunneling magnetothermopower in magnetic tunnel junction nanopillars. *Physical Review Letters*, 107:177201, 2011.

[65] W. Lin, M. Hehn, L. Chaput, B. Negulescu, S. Andrieu, F. Montaigne, and S. Mangin. Giant thermoelectric effect in Al2O3 magnetic tunnel junctions. *Nature communications*, 3:744, 2012.

[66] Y. Lu, T. Wei, F. Duewer, Y. Lu, N. Ming, P. G. Schultz, and X.-D. Xiang. Nondestructive Imaging of Dielectric-Constant Profiles and Ferroelectric Domains with a Scanning-Tip Microwave Near-Field Microscope. *Science*, 276:2004–2006, 1997.

[67] Y. J. Kim, L. Jofre, F. De Flaviis, and M. Q. Feng. Microwave Reflection To-

mographic Array for Damage Detection of Civil Structures. *IEEE Transactions on Antennas and Propagation*, 51:3022, 2003.

[68] M. T. Ghasr, M. A. Abou-Khousa, S. Kharkovsky, R. Zoughi, and D. Pommerenke. Portable real-time microwave camera at 24 GHz. *IEEE Transactions on Antennas and Propagation*, 60:1114, 2012.

[69] E. C. Fear, S. C. Hagness, P. M. Meaney, M. Okoniewski, and M. A. Stuchly. Enhancing breast tumor detection with near-field imaging. *IEEE Microwave Magazine*, 3:48, 2002.

[70] R. K. Amineh, M. Ravan, A. Trehan, and N. K. Nikolova. Near-field microwave imaging based on aperture raster scanning with TEM horn antennas. *IEEE Transactions on Antennas and Propagation*, 59:928, 2011.

[71] N. K. Nikolova. Microwave imaging for breast cancer. *IEEE Microwave Magazine*, 12:78, 2011.

[72] Z. X. Cao, W. Lu, L. Fu, Y. S. Gui, and C.-M. Hu. Spintronic microwave imaging. *Applied Physics A*, 111:329, 2013.

[73] S. Sugawara, Y. Maita, K. Adachi, K. Mori, and K. Mizuno. A mm-Wave Tapered Slot Antenna with Improved Radiation Pattern. *IEEE MTT-S International Microwave Symposium Digest*, page 959, 1997.

[74] G. H. Huff, J. Feng, S. Zhang, and J. T. Bernhard. A novel radiation pattern and frequency reconfigurable single turn square spiral microstrip antenna. *IEEE Microwave and Wireless Components Letters*, 13:57, 2003.

[75] A. Lai, K. M. K. H. Leong, and T. Itoh. Infinite Wavelength Resonant Antennas With Monopolar Radiation Pattern Based on Periodic Structures. *IEEE Transactions on Antennas and Propagation*, 55:868, 2007.

[76] U. R. Krafta. Polarization Properties of Sprial Antennas: A Tutorial. *Electromagnetics*, 14:259, 1994.

[77] H. M. Smith. *Principles of holography.* Wiley-Interscience, 1969.

[78] D. M. Sheen, D. L. McMakin, and T. E. Hall. Three-dimensional millimeter-wave imaging for concealed weapon detection. *IEEE Transactions on Microwave Theory and Techniques*, 49:1581, 2001.

[79] D. M. Sheen, D. L. McMakin, and T. E. Hall. Near field imaging at microwave and millimeter wave frequencies. *IEEE MTT-S International Microwave Symposium Digest*, page 1693, 2007.

[80] R. Appleby and H. B. Wallace. Standoff detection of weapons and contraband in the 100 GHz to 1 THz region. *IEEE Transactions on Antennas and Propagation*, 55:2944, 2007.

[81] C. F. Cull, D. A. Wikner, J. N. Mait, M. Mattheiss, and D. J. Brady. Millimeter-wave compressive holography. *Applied optics*, 49:E67, 2010.

[82] R. K. Amineh, M. Ravan, A. Khalatpour, and N. K. Nikolova. Three-dimensional near-field microwave holography using reflected and transmitted signals. *IEEE Transactions on Antennas and Propagation*, 59:4777, 2011.

[83] R. K. Amineh, A. Khalatpour, H. Xu, Y. Baskharoun, and N. K. Nikolova. Three-dimensional near-field microwave holography for tissue imaging. *International Journal of Biomedical Imaging*, 2012:291494, 2012.

[84] M. Ravan, R. K. Amineh, and N. K. Nikolova. Two-dimensional near-field microwave holography. *Inverse Problems*, 26:055011, 2010.

[85] M. Elsdon, D. Smith, M. Leach, and S. J. Foti. Experimental investigation of breast tumor imaging using indirect microwave holography, 2006.

[86] M. Elsdon, M. Leach, S. Skobelev, and D. Smith. Microwave Holographic Imaging of Breast Cancer. *IEEE 2007 International Symposium on Microwave, Antenna, Propagation, and EMC Technologies For Wireless Communications*, page 966, 2007.

[87] X. Fan, S. Kim, X. Kou, J. Kolodzey, H. Zhang, and J. Q. Xiao. Microwave phase detection with a magnetic tunnel junction. *Applied Physics Letters*, 97:212501, 2010.

[88] L. Fu, Y. S. Gui, Y. Xiao, M. Jaidann, H. Guo, H. Abou-Rachid, and C.-M. Hu. Detection of concealed targets using spintronic microwave sensor. *Proceedings of SPIE*, 9454:945406, 2015.

[89] C M Hu, Y Gui, and L Fu. Rapid microwave phase detection with a solid state device. *U. S. Patent pending*, WO 2015063596 A1, 2015.

[90] Canadian Cancer Society. Canadian Cancer Statistics Special topic : Predic-

tions of the future burden of cancer in Canada. *Public Health Agency of Canada*, page 1, 2015.

[91] S. Manfred and H. Aichinger. Recent developments in breast imaging. *Phys. Med. Biol.*, 41:315, 1996.

[92] S. Venkataraman, N. Hines, and P. J. Slanetz. Challenges in mammography: Part 2, multimodality review of breast augmentation - Imaging findings and complications. *American Journal of Roentgenology*, 197:1031, 2011.

[93] A. Karellas and S. Vedantham. Breast cancer imaging: a perspective for the next decade. *Medical physics*, 35:4878, 2008.

[94] J.-W. Tian, L.-T. Sun, Y.-H. Guo, H. D. Cheng, and Y.-T. Zhang. Computerized-aid diagnosis of breast mass using ultrasound image. *Medical physics*, 34:3158, 2007.

[95] A. Abbosh and S. Crozier. Strain Imaging of the Breast by Compression Microwave Imaging. *IEEE Antennas Wireless Propagat. Lett.*, 9:1229, 2011.

[96] Z. Ji, C. Lou, S. Yang, and D. Xing. Three-dimensional thermoacoustic imaging for early breast cancer detection. *Medical Physics*, 39:6738, 2012.

[97] R. Scapaticci, G. Bellizzi, I. Catapano, L. Crocco, and O. M. Bucci. An effective procedure for MNP-enhanced breast cancer microwave imaging. *IEEE Transactions on Biomedical Engineering*, 61:1071, 2014.

[98] M. Soumekh. *Synthetic aperture radar signal processing.* John Wiley and Sons, 1999.

[99] A. P. Annan. Chapter 1 - Electromagnetic Principles of Ground Penetrating Radar. In Harry M Jol, editor, *Ground Penetrating Radar Theory and Applications*, pages 1–40. Elsevier, Amsterdam, 2009.

[100] D. Flores-Tapia, G. Thomas, and S. Pistorius. A wavefront reconstruction method for 3-D cylindrical subsurface radar imaging. *IEEE transactions on image processing*, 17:1908, 2008.

[101] D. Flores-Tapia, G. Thomas, N. Venugopal, B. McCurdy, and S. Pistorius. Semi automatic MRI prostate segmentation based on wavelet multiscale products., 2008.

[102] D. Flores-Tapia and S. Pistorius. Real time breast microwave radar image reconstruction using circular holography: A study of experimental feasibility. *Medical Physics*, 38:5420, 2011.

[103] M. Schäfers, V. Drewello, G. Reiss, A. Thomas, K. Thiel, G. Eilers, M. Münzenberg, H. Schuhmann, and M. Seibt. Electric breakdown in ultrathin MgO tunnel barrier junctions for spin-transfer torque switching. *Applied Physics Letters*, 95:232119, 2009.

[104] H. J. Tang, S. Kaur, L. Fu, B. M. Yao, X. Li, H. M. Gong, Y. S. Gui, and C.-M. Hu. Life signal detection using an on-chip split-ring based solid state microwave sensor. *Applied Physics Letters*, 105:133703, 2014.